

RL-TR-97-147
In-House Report
October 1997



A DIFFRACTIVE OPTIC IMAGE SPECTROMETER (DOIS)

Denise M. Lyons

APPROVED FOR PUBLIC RELEASE; DISTRIBUTION UNLIMITED.

DTIC QUALITY INSPECTED

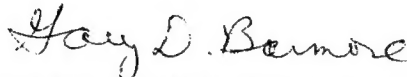
19980209 077

**Rome Laboratory
Air Force Materiel Command
Rome, New York**

This report has been reviewed by the Rome Laboratory Public Affairs Office (PA) and is releasable to the National Technical Information Service (NTIS). At NTIS it will be releasable to the general public, including foreign nations.

RL-TR-97-147 has been reviewed and is approved for publication.

APPROVED:



GARY D. BARMORE, Maj., USAF
Chief, Photonics Division
Surveillance & Photonics Directorate

FOR THE DIRECTOR:



DONALD W. HANSON, Director
Surveillance & Photonics Directorate

If your address has changed or if you wish to be removed from the Rome Laboratory mailing list, or if the addressee is no longer employed by your organization, please notify Rome Laboratory/OCPC, Rome, NY 13441. This will assist us in maintaining a current mailing list.

Do not return copies of this report unless contractual obligations or notices on a specific document require that it be returned.

REPORT DOCUMENTATION PAGE			Form Approved OMB No. 0704-0188	
Public reporting burden for this collection of information is estimated to average 1 hour per response, including the time for reviewing instructions, searching existing data sources, gathering and maintaining the data needed, and completing and reviewing the collection of information. Send comments regarding this burden estimate or any other aspect of this collection of information, including suggestions for reducing this burden, to Washington Headquarters Services, Directorate for Information Operations and Reports, 1215 Jefferson Davis Highway, Suite 1204, Arlington, VA 22202-4302, and to the Office of Management and Budget, Paperwork Reduction Project (0704-0188), Washington, DC 20503.				
1. AGENCY USE ONLY (Leave blank)		2. REPORT DATE October 1997	3. REPORT TYPE AND DATES COVERED FINAL, Oct 94 - Sep 96 In-House	
4. TITLE AND SUBTITLE A DIFFRACTIVE OPTIC IMAGE SPECTROMETER (DOIS)			5. FUNDING NUMBERS C - NA PE - 62702F PR - 4600 TA - P1 WU - 15	
6. AUTHOR(S) Denise M. Lyons				
7. PERFORMING ORGANIZATION NAME(S) AND ADDRESS(ES) Rome Laboratory/OCPC 25 Electronic Pky Rome NY 13441-4515			8. PERFORMING ORGANIZATION REPORT NUMBER RL-TR-97-147	
9. SPONSORING / MONITORING AGENCY NAME(S) AND ADDRESS(ES) Rome Laboratory/OCPC 25 Electronic Pky Rome NY 13441-4515			10. SPONSORING / MONITORING AGENCY REPORT NUMBER RL-TR-97-147	
11. SUPPLEMENTARY NOTES Rome Laboratory Project Engineer: Denise M. Lyons, OCPC, (315) 330-3145				
12a. DISTRIBUTION AVAILABILITY STATEMENT APPROVED FOR PUBLIC RELEASE; DISTRIBUTION UNLIMITED			12b. DISTRIBUTION CODE	
13. ABSTRACT (Maximum 200 words) The diffractive optic imaging spectrometer, DOIS, is a high resolution, compact, economical, rugged, programmable, multi-spectral imager that can be built for ultraviolet, visible or infrared applications in surveillance, remote sensing, medical imaging, law enforcement, environmental monitoring, and laser counter intelligence. The design implements a conventional CCD camera and emerging diffractive optical element (DOE) technology in an elegant configuration, adding spectroscopy capabilities to current imaging systems. In DOIS a DOE performs the imaging and provides the dispersion necessary to separate a multi-spectral target into separate spectral images. The CCD is scanned along the optical axis recording a series of spectral images in a process referred to as diffractive spectral sectioning. Under this project 3D spectral/spatial DOE imaging theory was developed and implemented in software to predict the system's performance. A visible spectrum DOIS prototype was designed, fabricated, characterized and demonstrated with a variety of known targets. To reconstruct the 3D object cubes, various deconvolution algorithms; nearest neighbor, inverse filtering and constrained iterative deconvolution, were developed. The best results were obtained using an SVD inverse Fourier deconvolution algorithm with regularization for noise suppression. Additional DOIS designs are presented for future work, including a configuration with constant magnification and with no moving parts.				
14. SUBJECT TERMS diffractive optic, imaging spectrometer, multi-spectral, hyper-spectral, spectral imaging			15. NUMBER OF PAGES 166	
			16. PRICE CODE	
17. SECURITY CLASSIFICATION OF REPORT UNCLASSIFIED	18. SECURITY CLASSIFICATION OF THIS PAGE UNCLASSIFIED	19. SECURITY CLASSIFICATION OF ABSTRACT UNCLASSIFIED	20. LIMITATION OF ABSTRACT UNLIMITED	

TABLE OF CONTENTS

LIST OF FIGURES	5
ABSTRACT.....	13
1. INTRODUCTION	15
1.1 <i>Image Spectrometry</i>	15
1.2 <i>Figures of Merit</i>	16
1.3 <i>Common Image Spectrometers</i>	17
1.4 <i>Spectrotomography Techniques</i>	19
1.5 <i>DOIS</i>	20
1.6 <i>Dissertation's Objectives</i>	22
2. DOIS - DIFFRACTIVE OPTIC IMAGE SPECTROMETER.....	26
2.1 <i>Basic Scenario</i>	26
2.2 <i>Experimental Demonstration with a RGB monitor</i>	29
2.2.1 <i>Blue Background Demonstration</i>	33
2.3 <i>Continuous Magnification</i>	34
2.3.1 <i>Post-detection image resampling</i>	34
2.3.2 <i>Optical designs for constant magnification</i>	35
3. DIFFRACTIVE OPTICAL ELEMENTS	38
3.1 <i>Fresnel Zone Plate</i>	38
3.2 <i>DOE design and characteristic equations</i>	40
3.3 <i>Fabrication of Multilevel Profiles</i>	43
3.4 <i>The Incoherent Point Spread Function</i>	46
3.4.1 <i>Diffraction limited incoherent psf</i>	46
3.4.2 <i>Experimentally measured incoherent psf</i>	49
3.4.2.1 <i>Coherent vs. Incoherent Imaging</i>	49
3.4.2.2 <i>Experimentally measured results</i>	55

TABLE OF CONTENTS-Continued

4. THREE DIMENSIONAL IMAGE FORMATION WITH A DIFFRACTIVE OPTICAL ELEMENT (DOE)	59
4.1 <i>Imaging with a Diffractive Optic</i>	60
4.1.1 Spectral Gaussian Coordinate Transform.....	61
4.1.2 Three-dimensional Transfer Theory.....	63
4.2 <i>Isotomic Imaging in a narrow waveband</i>	64
4.2.1 Reconstruction.....	65
4.2.2 Define isotome bandwidth.....	66
4.3 <i>Full Spectrum Imaging.....</i>	67
4.3.1 Isotome Coordinate Transform	68
4.3.2 Reconstruction.....	70
4.3.3 Inverse Spectral Coordinate Transform.....	70
5. PROTOTYPE CHARACTERIZATION.....	71
5.1 <i>DOIS Prototype</i>	71
5.2 <i>The Diffractive Optic Element.....</i>	72
5.3 <i>The CCD camera</i>	78
5.4 <i>DOIS prototype characteristics.....</i>	80
5.5 <i>Spatial and Spectral point spread function (psf)</i>	82
6. IMAGE FORMATION	85
6.1 <i>Mercury 577/579 nm doublet with an X aperture.....</i>	85
6.2 <i>Spectral/spatial analysis.....</i>	89
6.2.1 Monochromatic target, increasing aperture.....	92
6.2.2 Doublet target, increasing aperture.....	92
7. PROTOTYPE DEMONSTRATION WITH FOUR TARGETS	96
7.1 <i>Testbed Specifications.....</i>	96
7.2 <i>Results.....</i>	101

TABLE OF CONTENTS-Continued

8. OBJECT RECONSTRUCTION ALGORITHMS	107
8.1 <i>Digital Representation</i>	109
8.2 <i>Nearest Neighbor Reconstruction.....</i>	109
8.3 <i>Inverse Filtering</i>	115
8.3.1 <i>Apodization Inverse Filter.....</i>	116
8.3.2 <i>Regularized Inverse Filter.....</i>	119
8.3.3 <i>Singular Value Decomposition Inverse Filter.....</i>	124
8.3.3.1 <i>SVD results.....</i>	134
8.4 <i>Constrained Iterative Deconvolution</i>	143
9. CONCLUSION.....	150
9.1 <i>DOIS Advantages</i>	150
9.2 <i>Suggestions for future work</i>	152
9.2.1 <i>Dual Waveband design using multiple orders</i>	152
9.2.2 <i>Programmable DOE with an SLM, variable focus device.....</i>	153
9.2.3 <i>Array of DOEs.....</i>	153
REFERENCES.....	155

LIST OF FIGURES

Figure 1.1: Typical spectral line used to define spectral resolution.....	17
Figure 1.2: Three-dimensional image cube for a color filter wheel image spectrometer.	17
Figure 1.3: Grating image spectrometer three-dimensional image cube.	18
Figure 1.4: Three-dimensional data cubes for a Fourier Transform image spectrometer. ...	19
Figure 1.5: Three-dimensional Spectral imaging with a diffractive optical element.	21
Figure 1.6: The spectral image distances and magnifications for an object at $2f_o$	21
Figure 1.7: The six Cartesian Coordinate systems used in DOIS.	23
Figure 2.1: DOIS - Diffractive Optic Image Spectrometer basic scenario.	27
Figure 2.2: Algorithm for calculating wavelength from image distance, s_i	28
Figure 2.3: Example of the color picker window in Adobe Photoshop™ for the blue AFMC target.	30
Figure 2.4: Phosphor emission curves for red (P22R), green (P22G), and blue (P22B) phosphor, the measured blue and green agree with wideband textbook curves however the measured red differs dramatically.	31
Figure 2.5: Spectral images recorded with DOIS. The target is text displayed on an AppleColor™ high resolution RGB monitor.....	32
Figure 2.6: Images from green ROME and red LAB on a blue background (a) blue focus (b) green (c) red.	33
Figure 2.7: Define a pixel footprint Ω_{pixel}	34
Figure 2.8: Relay DOIS design with minimal magnification change.....	35
Figure 2.9: Magnification change vs. wavelength for original, relay and zoom designs. ...	37

LIST OF FIGURES-Continued

Figure 2.10: Zoom DOIS design with constant magnification.....	37
Figure 3.1: Fresnel zone plate phase profiles.	39
Figure 3.2: Diffraction efficiency vs. number of masks and phase levels.....	39
Figure 3.3: Ray trace that determines zone radii.....	40
Figure 3.4: Diffraction Efficiency vs. Wavelength for $N=2$ and $N=16$	42
Figure 3.5: Photolithography multilevel fabrication algorithm.....	44
Figure 3.6: SEM photos of DOE rings. (a) Top view, feature size is $\approx 10\mu\text{m}$. (b) Side view of the outermost rings, feature size is $\approx 2.5\mu\text{m}$	45
Figure 3.7: A density plot of the diffraction limited intensity psf, $h(v,u)$, it is rotationally symmetric around the u axis.	47
Figure 3.8: A theoretical plot of $h(v,0)$ in the focal plane.	48
Figure 3.9: A theoretical plot of $h(0,u)$ along the optical axis.....	48
Figure 3.10: A theoretical plot of $h(v,v)$ where $u=v$	49
Figure 3.11: (a) The theoretical intensity distribution in the coherent and incoherent images of a slit. (b) the recorded image of a coherent slit. (reprinted from Reynolds 1989, page 115).....	52
Figure 3.12: The diffraction limited impulse response for (a) coherent and (b) incoherent illumination.....	53
Figure 3.13: Cross-sections of various magnified pinholes, $MT=-.1$, (left column), alongside the resulting diffraction limited intensity distributions from coherent (bold line) and incoherent (thin line) illumination plotted together (right column).....	54
Figure 3.14: Series of images (32×32 pixels) of a $5\mu\text{m}$ pinhole illuminated by a HeNe laser recorded with DOIS through focus.	55

LIST OF FIGURES-Continued

Figure 3.15: The experimentally measured intensity point spread function, $h(r,z)$, (a) a density plot (b) a 3D plot.	56
Figure 3.16: The theoretical and measured on-axis/spectral intensity psf, $h(z(\lambda))=h(0,u)$.	57
Figure 3.17: The experimentally measured OTF(r,z), (a) a density plot (b) a 3D plot.....	58
Figure 4.1: A flow chart depicting the manipulation of the three-dimensional object cube as it is imaged, and reconstructed.....	59
Figure 4.2: A diffractive optical element imaging various spectral point sources.....	61
Figure 4.3: The variance on (a) R_v , and (b) Z_u , at $z_0=10f_0$	67
Figure 4.4: Visual representation of the isotome coordinate transform forming an image space with unit magnification	69
Figure 5.1: Photo of the DOIS prototype.....	71
Figure 5.2: DOE figures of Merit.....	73
Figure 5.3: A partial image of the DOE rings.	73
Figure 5.4: Diffraction efficiency experimental setup (a) determine the total power. (b) first order power at $r/2$. (c) first order power at full aperture.....	75
Figure 5.5: Theoretical and measured diffraction efficiency vs. wavelength.....	75
Figure 5.6: DOE MTF, measured at RPC Diffractive Optic Testing Facility.....	77
Figure 5.7: DOIS camera specifications.	78
Figure 5.8: The experimentally determined spectral response curve of the SONY CCD. The dashed line is the raw data, and the solid line has the spectral curve of the lamp and monochromator grating divided out.	79

LIST OF FIGURES-Continued

Figure 5.9: The experimentally determined spectral response curve of the SONY CCD after the removal of a factory placed filter. The dashed line is the raw data, and the solid line has the spectral curve of the lamp and monochrometer grating divided out.	80
Figure 5.10: A pictorial representation of the system's MTF, a DOIS image of an Air Force Resolution Target.....	81
Figure 5.11: Schematic of DOIS.	81
Figure 5.12: Excel spreadsheet calibrating the DOE and detector carrier locations z , to a corresponding wavelength, λ	82
Figure 5.13: Series of images (32 x 32 pixels) of a 5 μm pinhole illuminated by a HeNe laser recorded with DOIS through focus.	83
Figure 5.14: Spatial Impulse response $h(r)$ at 632.8 nm, plotted as greylevel vs. pixel number for locations (a) approaching focus. (b) leaving focus.....	83
Figure 5.15: Spectral Impulse response $h(\lambda)$, plotted as intensity of one pixel through focus (a) for 632.8 nm. (b) for 542 nm.	84
Figure 5.16: The experimentally determined spectral resolution.....	84
Figure 6.1: Mathematica code that implements the linear system algorithm.....	85
Figure 6.2: Simulated spectral object & image channels of a Mercury doublet X, using experimentally measured $\text{psf}(x,y,z(\lambda))$	87
Figure 6.3: Spectral radiance plots of a Mercury doublet 577/579nm (a) the assumed input source object. (b) the computer generated results. (c) the experimental result.	88
Figure 6.4: 3D object cube and zy view of a rectangular aperture emitting (a) monochromatically (b) a doublet source.....	90

LIST OF FIGURES-*Continued*

Figure 6.5: Cross-sections of the three-dimensional point spread functions used in CG image formation and object reconstruction.	91
Figure 6.6: Computer generated monochromatic target of increasing size.	92
Figure 6.7: Computer generated (CG) and experimentally recorded doublets of increasing size.	93
Figure 6.8: A point spread function askew from off-axis aberrations.	94
Figure 6.9: The psf of a pixel at the edge of the detection area.	95
Figure 7.1: The Four targets: a Tungsten Halogen Lamp, a Mercury Lamp, a HeNe and a GreNe.....	96
Figure 7.2: Spectral Distribution of the Newport Tungsten Halogen Lamp (a) reprinted from the Newport operations manual, (b) measured with DOIS.	97
Figure 7.3: Spectral radiance curve of the Mercury Lamp (a) reprinted from Applied Optics, (b) measured with DOIS.....	98
Figure 7.4: Schematic of the four targets testbed.....	99
Figure 7.5: Sample of the key spectral DOIS images in this demonstration.....	100
Figure 7.6: Peak spectral lines of the target, calculated from the locations of best focus.	101
Figure 7.7: Tungsten Halogen Data (a) spectral images of the 50 μ m pinhole. (b) the measured spectral radiance curve.....	103
Figure 7.8: Sketch of image drifting between pixels.....	103
Figure 7.9: HeNe Data (a) spectral images of the 5 μ m pinhole. (b) the measured spectral radiance curve ($dz=0.005''=0.0125\text{cm}$, $d\lambda\approx 0.3\text{-}0.4\text{nm}$).....	104

LIST OF FIGURES-Continued

Figure 7.10: GreNe Data (a) spectral images of the 10 μ m pinhole. (b) the measured spectral radiance curve ($dz=0.005''=0.0125\text{cm}$, $d\lambda\approx 0.2\text{-}0.3\text{nm}$).	105
Figure 7.11: The measured spectral radiance curves of each Mercury line with the in-focus 32x32 pixel spectral image(s) of the center of the cross, (a) 365nm line. (b) 404nm line. (c) 435nm line. (d) 546nm line. (e) 577/579nm doublet.	106
Figure 8.1: Mathematica implementation of the Nearest Neighbor algorithm for 20 images.	112
Figure 8.2: Recorded Mercury images and corresponding restored objects with Nearest Neighbor technique.	113
Figure 8.3: Restoration of Mercury spectral radiance curve with Nearest Neighbor technique. (a) the recorded spectra, and the reconstructed spectra with (b) $n=0.45$.	114
Figure 8.4: The Mathematica code for inverse reconstruction with apodization.	117
Figure 8.5: List Plot of the flattened (a) psf. (b) OTF.	117
Figure 8.6: Object results from apodization reconstruction with CG images (left column) and recorded iris images (right column).	118
Figure 8.7: Mathematica code for the Regularized Inverse Filter.	120
Figure 8.8: Resulting object sets after Regularized Inverse reconstruction with various α .	121
Figure 8.9: Spectral Radiance of pixel 16,16 before and after (bold) the Regularized Inverse reconstruction with $\alpha = 0.005$	121
Figure 8.10: CG doublet objects, images and reconstructed objects.	122
Figure 8.11: Measured Mercury doublet images and Regularized Inverse reconstructed.	123
Figure 8.12: Results of Regularized Inverse filter on measured 400 μ m and iris images.	123

LIST OF FIGURES-Continued

Figure 8.13 (c): Cross-section of the 3D combination psf used in SVD object reconstruction (contrast enhanced to show detail).....	128
Figure 8.14: Mathematica code to calculate the "basis" OTF, $P[[\Delta z, x, z]]$	128
Figure 8.15: Mathematica code to form the OTF Matrix.....	129
Figure 8.16: Mathematica code to create inim which converts the NxN Complex matrix into an 2NxN of all Real values.	130
Figure 8.17: Mathematica code to create the Fourier space matrix IMAGE	131
Figure 8.18: Mathematica code finds the SVD matrices, inverts the OTF and finds the reconstructed OBJ matrix.....	131
Figure 8.19: Mathematica code takes the inverse Fourier transform of the OBJ matrix..	132
Figure 8.20: Singular Values $w_{ji}(x,z)$ Matrix plots.....	133
Figure 8.21: Cross-section shows missing cone.	133
Figure 8.22: Table of the z values for the following output series.	134
Figure 8.23: $z(\lambda)$ vs. y cross-section and spectral plots from SVD applied to CG Doublet.	136
Figure 8.24: SVD reconstructed object series from the CG 8 x 8 pixel doublet aperture, previously depicted as cross-sections in 8.23.....	137
Figure 8.25: SVD reconstructed object series from the CG 16 x16 pixel doublet aperture, previously depicted as cross-sections in 8.23.....	138
Figure 8.26: SVD reconstructed object series from the experimentally measured Hg 577/579 nm X.	139
Figure 8.27: SVD reconstructed object series from the experimentally measured 542 nm GreNe point-source with a trapezoidal 546 nm Mercury target.....	140

LIST OF FIGURES-Continued

Figure 8.28: SVD reconstructed object series from the experimentally measured Mercury Rectangle.....	141
Figure 8.29: SVD reconstructed object series from the experimentally measured Iris illuminated by a Mercury bulb (notice the hot spot).....	142
Figure 8.30: Mathematica code for the Jansson-vanCittert algorithm.....	144
Figure 8.31: Resulting images after Jansson-vanCittert reconstruction with various iterations. (a) original recorded data. (b) $n=10$. (c) $n=20$	144
Figure 8.32: Spectral Radiance of pixel 16,16 Jansson-vanCittert reconstruction at various iterations.....	145
Figure 8.33: Mathematica code for Regularized Inverse Filtered vanCittert iterative reconstruction.....	146
Figure 8.34: CG doublet; rms error after each iteration for (a) the CG doublet and (b) the iris.....	146
Figure 8.35: CG doublet; results of Regularized Inverse Filtered vanCittert iterative reconstruction with $\mu=0.001$	148
Figure 8.36: Results of iris reconstruction after (a) 3D Regularized Inverse filter and (b-e) with Regularized Inverse Filtered vanCittert iterative reconstruction $\alpha=.01$	149
Figure 8.37: Reconstructed iris objects after 10 & 20 iterations.....	149
Figure 9.1: Two waveband design, mid IR and far IR, with $\lambda_0=7.3\mu\text{m}$ (a) spectral η for each order, (b) the two wavelengths at each focal position.....	152
Figure 9.2: Design for a static DOIS with a controllable, variable focus lens.....	153
Figure 9.3: Design for a static DOIS with a DOE lens array.	154

ABSTRACT

The diffractive optic imaging spectrometer, DOIS, is a high resolution, compact, economical, rugged, programmable, multi-spectral imager. The design implements a conventional CCD camera and emerging diffractive optical element (DOE) technology in an elegant configuration, adding spectroscopy capabilities to current imaging systems [Lyons 1995].

One limitation of DOEs, also known as zone plate lenses, is abundant chromatic aberration. DOIS exploits this typically unwanted effect, utilizing a DOE to perform the imaging and provide the dispersion necessary to separate a multi-spectral target into separate spectral images. The CCD is stepped or scanned along the optical axis recording a series of these spectral images. This process is referred to as diffractive spectral sectioning.

Under this dissertation, three-dimensional spectral/spatial DOE imaging theory was developed to describe and predict the system's performance. The theory was implemented in a software model to simulate DOIS image cubes. A visible spectrum DOIS prototype was designed, fabricated and characterized. The system's incoherent point spread function was theoretically modeled and experimentally determined. To verify the simulations, the prototype's performance was demonstrated with a variety of known targets and compared to simulated image cubes. To reconstruct the three-dimensional object cubes, various deconvolution algorithms; nearest neighbor, inverse filtering and constrained iterative deconvolution, were developed and applied to both computer generated and experimentally measured image cubes. The best results were obtained using an SVD inverse Fourier deconvolution algorithm with regularization for noise suppression. The results demonstrate a resolving power greater than 288 ($\lambda/\Delta\lambda=577\text{nm}/2\text{nm}$). Finally, three additional DOIS

designs are presented as suggestions for future work, including a configuration with no moving parts which records the entire 3D image cube in one "snapshot".

DOIS is a practical image spectrometer that can be built to operate at ultraviolet, visible or infrared wavelengths for applications in surveillance, remote sensing, medical imaging, law enforcement, environmental monitoring, and laser counter intelligence.

1. INTRODUCTION

The field of multi- and hyper-spectral imaging, also known as Imaging Spectrometry, has a long history [Goetz 1995] and has been receiving increased attention for several years. As discussed elsewhere [Descour 1995], Imaging Spectrometry adds the ability to examine the spectral distribution of two-dimensional scenes to the fundamental power of imaging systems. The availability of known spectral radiance, reflectance and absorption curves coupled with an imaging spectrometer allows identification and classification of targets with an accuracy and resolution previously unknown.

An entire chapter of the *IR Handbook* [Wolfe 1989] is dedicated to the spectral properties of natural sources. Recorded spectra can be compared to these and other known spectra to identify the material composition of a target. A spectrometer is an instrument for resolving and recording these spectra. The combination of an imager and a spectrometer, an imaging spectrometer, provides a conventional spatial image as well as the spectral content of each pixel, forming a three-dimensional spatial/spectral image cube. The result is a complete system capable of target detection, classification and identification.

Image spectrometers can be built to operate in the ultra-violet (UV), visible or infrared (IR) spectrum and measure spectral reflectance, emission and/or absorption. Spectra can be used as a "fingerprint" to determine exactly what material or mix of materials is present. Whether the data is from the paint of a military tank, the plume of a missile, the ground in the desert or the air we breathe, spectral information can lead to recognition of a detected target or even detect the presence of unwanted materials.

1.1 Image Spectrometry

The goal of an image spectrometer is to obtain a set of spectral images of a target to form an image cube. Each image represents a spectral band or channel, defined by a central

wavelength, λ_c , and its spectral bandwidth, $\Delta\lambda$. The total number of channels is equal to the entire wavelength range divided by the channel bandwidth.

$$\# \text{ of channels} = (\lambda_{\max} - \lambda_{\min})/\Delta\lambda \quad (1.1)$$

Common image spectrometers include three components: a dispersion element, an imager and a detection device [Wolfe 1989]. Examples include a lens and color filter wheel in front of a two-dimensional detector array, or a single pixel aperture illuminating a diffraction grating, dispersing the light onto a linear detector array. The detector records one pixel at all wavelengths which is then scanned in the x and y directions to form an image.

1.2 Figures of Merit

When designing or comparing imaging spectrometers it is customary to discuss the spectral resolution of the system [Wolfe 1994]. Spectral lines usually have some predetermined shape, such as a Gaussian or Lorentzian. The line width, sometimes defined as the spectral slit width, is usually specified as the full width at half maximum (FWHM), as shown in Figure 1.1, noted as $\Delta\lambda$.

$$\text{spectral resolution} = \Delta\lambda \quad (1.2)$$

The relative resolution is the spectral resolution divided by the center wavelength.

$$\text{relative resolution} = \Delta\lambda/\lambda_c \quad (1.3)$$

Since bigger is always better, the resolving power is defined as the reciprocal of the relative resolution.

$$\text{resolving power} = \lambda_c/\Delta\lambda \quad (1.4)$$

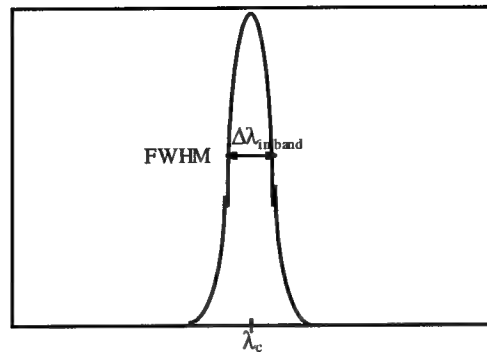


Figure 1.1: Typical spectral line used to define spectral resolution.

1.3 Common Image Spectrometers

The most simplistic image spectrometer is a standard camera (lens and detector) with various line-pass color filters. Typically the filters are placed on a wheel that is rotated so that they are in the optical path one at a time. Figure 1.2 shows that the data recorded is a series of two-dimensional (x,y) images stepped in wavelength. The number of filters determines how completely the spectra is sampled and the spectral resolution of each filter is the spectral resolution of the spectrometer. However, the system's size, complexity and cost are directly related to the number and quality of the filters, and the materials needed for some filters have limited availability. Additionally, once designed and built it is inflexible; interest in additional wavelengths will require an upgrade.

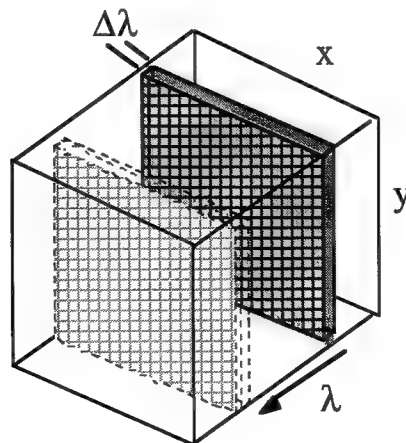


Figure 1.2: Three-dimensional image cube for a color filter wheel image spectrometer.

Another popular design is the grating spectrometer. A narrow, rectangular entrance slit is imaged onto a linear diffraction grating and then on to a two-dimensional detector. The grating's dispersion is perpendicular to the long axis of the slit. The detector records a spatial image in one direction and the spectra along the other. The data is a set of spatial/spectral images, (x,λ) or (y,λ) , that are recorded as the aperture is scanned along the scene in a pushbroom manner to form an image shown in the image cube of Figure 1.3. Its advantage is that there is a continuous spectra from the diffraction grating, so the resolution is determined by the optical magnification and detector size (parameters that a designer should have full control over). However, in order to view a conventional (x,y) image for target acquisition and tracking, it requires a scanning mechanism which can be sensitive to vibration and motion of the target.

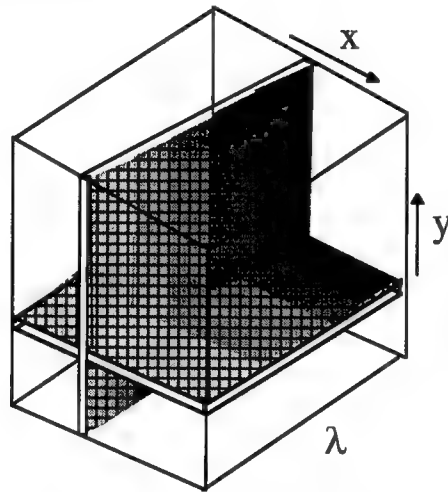


Figure 1.3: Grating image spectrometer three-dimensional image cube.

A third design is a Michelson interferometer setup with an oscillating mirror in one path. As the mirror moves, the interference term varies as the cosine of the oscillation with a frequency of $2\pi/\lambda$ for a monochromatic source. A source of a different wavelength or frequency will provide an interference pattern with a different frequency, $2\pi/\lambda_2$. If the two are used at the same time then the pattern will be the sum of two cosines, each modified by its amplitude. With a multi-spectral source, the interferogram obtained as the mirror moves is the sum of a collection of monochromatic interference patterns, each with its own amplitude. The interference pattern is recorded over time, correlated to the optical path difference caused by the mirror, and Fourier transformed to yield the spectrum. A CCD focal plane array can be placed at the detection plane to simultaneously record the frequency spectrum of multiple pixels, forming an image once the transform is performed, as shown in Figure 1.4. This technique provides very high resolution data however it is sensitive to vibrations and target motion during recording.

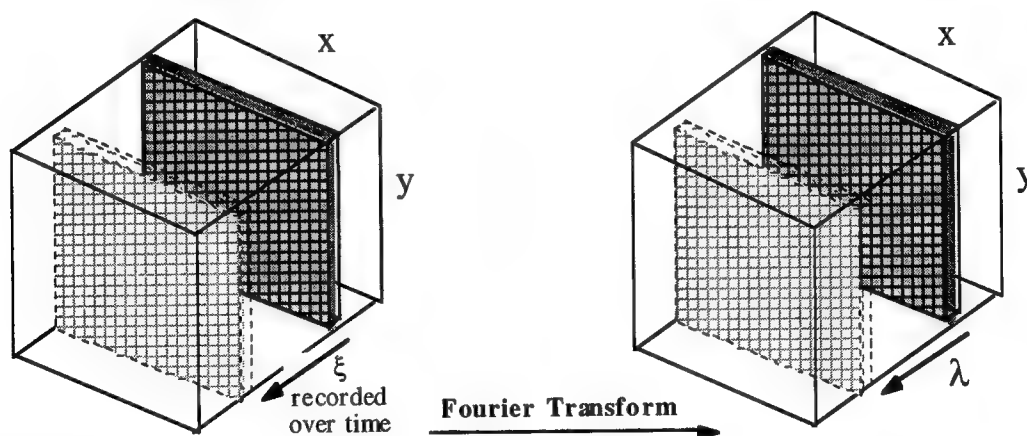


Figure 1.4: Three-dimensional data cubes for a Fourier Transform image spectrometer.

1.4 Spectrotomography Techniques

Spectrotomography is a new branch of optical tomography where the three-dimensional data cube is integrated along various axes forming two-dimensional

projections of the 3D data. These projections, containing integral data on the spectral and spatial properties of the object of interest, are recorded then processed with computer tomography algorithms to reconstruct the 3D data cube. Researchers use several techniques with various dispersion, scanning, and reconstruction methods for applying computer tomography to imaging spectrometry. A major advantage of these systems is high throughput efficiency. The projections integrate all possible photons and therefore no light is discarded, which is useful in low light scenarios. Although, the recorded data requires much processing to form a recognizable image cube. Also, much emphasis has been placed on the future ability to build a system with no moving parts and with a single snap-shot approach for moving targets [Descour 1995].

1.5 DOIS

The diffractive optic image spectrometer design is a spectro-tomographic technique which integrates over a narrowband of the image cube. Shown in Figure 1.5, the DOE provides both the spatial imaging and the spectral dispersion in this image spectrometer [Hinnrichs 1995, Lyons 1995].

A panchromatic CCD camera is used for detection. This camera, mounted parallel to the DOE, is stepped along the optical axis, \bar{z} . Each detector location z corresponds to a specific spectral channel of the target's image. As an example, Figure 1.6 lists the calculated image distance z_i and magnifications for particular spectral slices of an object located $2f_d$ from the DOE, where f_d is the focal length at the DOE design wavelength λ_d . The camera is interfaced to a frame grabber board within a computer for image capture, analysis, display and post detection processing. At each step along the optical axis, both an image frame and the corresponding detector location is recorded.

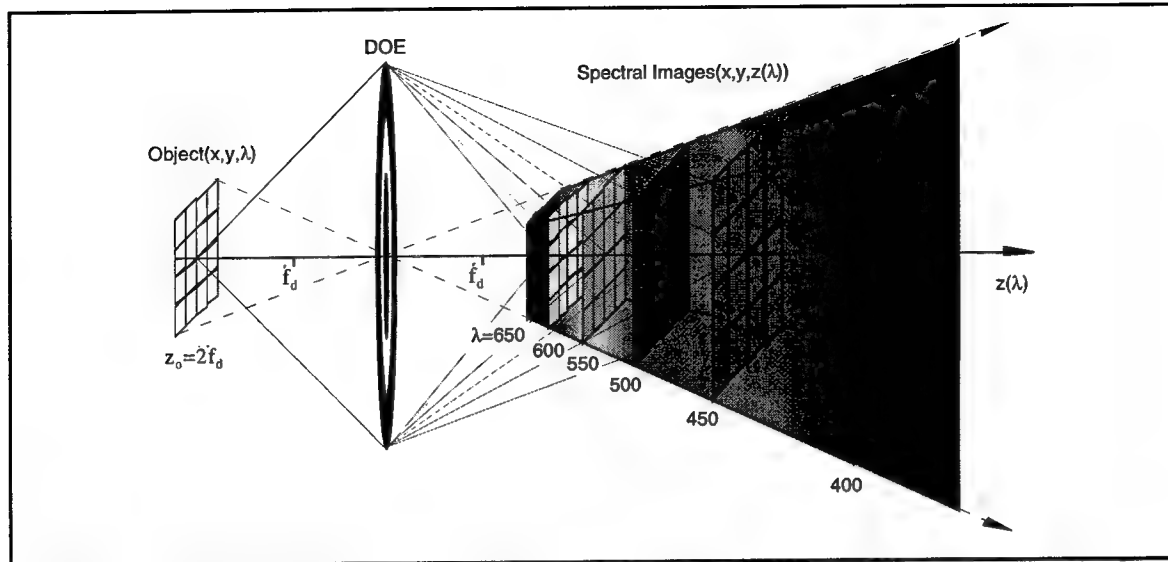


Figure 1.5: Three-dimensional Spectral imaging with a diffractive optical element (DOE).

λ [nm]	z_i	$M_{\text{Transverse}}$	$M_{\text{Longitudinal}}$
650	$1.7f_d$	0.83	0.68
600	$1.9f_d$	0.96	0.92
588	$2.0f_d$	1.00	1.00
550	$2.3f_d$	1.15	1.32
500	$2.9f_d$	1.43	2.04
450	$3.8f_d$	1.88	3.55
400	$5.5f_d$	2.77	7.69

Figure 1.6: The spectral image distances z_i and magnifications for an object at $z_o = 2f_d$.

The images captured by the CCD are a superposition of one channel's infocus image and defocused images of the surrounding channels. These defocused components cause blurring of the desired image.

Like a color filter, DOIS integrates over a bandpass, dictated by the DOE's incoherent point spread function. However, DOIS can provide greater spectral resolution by scanning along the z axis, shifting the center of the bandpass and sampling the spectra at several spectral points for every point that the filter could sample. Once sampled, digital image restoration techniques can be applied to remove the blurred information and reconstruct the original spectra.

The DOE dispersion is so great that each image is an integral of data in only a narrow spectral band, not the entire spectrum. This leads to a system that is useful both with and without post-detection processing. Without processing DOIS provides spectral images with spectral resolution that rivals color filter wheels. The spectral resolution is defined by the region of spectral integration measured to be as good as 1.5nm for spatially unresolved targets [Chapter 7]. Higher resolving power is achievable with DOIS by applying digital image restoration algorithms which improve the resolution by eliminating spectral and spatial blur [Chapter 8].

1.6 Dissertation's Objectives

Parallel to the efforts under this dissertation, Michele Hinnrichs from Pacific Advanced Technology (PAT) conceived and patented the mechanical design of the diffractive optic image spectrometer described in this dissertation [Hinnrichs 1995]. Although an IR system had been built and demonstrated on real-world targets, there was a lack of analysis theory and understanding of spectral imaging with a diffractive optic. This theory was needed for analytical modeling and simulation of the image spectrometer design, and required to develop object reconstruction algorithms for imaging resolved targets with high spectral and spatial resolution.

The objectives of this dissertation were to determine the theory behind diffractive spectral imaging, implement the theory in a software model to simulate DOIS image cubes, experimentally verify the simulated results with a hardware prototype imaging known spectral/spatial targets, and develop and apply object reconstruction algorithms to the simulated and experimentally measured image cubes. Additionally, an improved design was conceived to provide diffractive optic image spectrometry with constant magnification [Lyons 1997].

In the next chapter, the capabilities of the diffractive optic image spectrometer are first demonstrated. A visible spectral range DOIS prototype imaged an AppleColor™ high resolution RGB computer monitor with the words AFMC ROME LAB spelled out in blue, green and red phosphor respectively. Although a much more analytical characterization is presented later in Chapter 7, this experiment is useful for discussion and introduction to DOIS's operation.

Since the main component is a diffractive optical element (DOE) providing both imaging and dispersion for this image spectrometer, Chapter 3 details some important theory, design and characteristic equations, fabrication techniques and modeling schemes of the Fresnel Zone Plate which is the DOE used in DOIS.

The theory of image formation with the diffractive optic is developed in Chapter 4. The three-dimensional image cube is collected by recording a set of images taken at sequential focal planes. By analogy with physical sectioning techniques, this method is called diffractive spectral sectioning. For convenience, Figure 1.7 lists the six Cartesian Coordinate systems used throughout this dissertation.

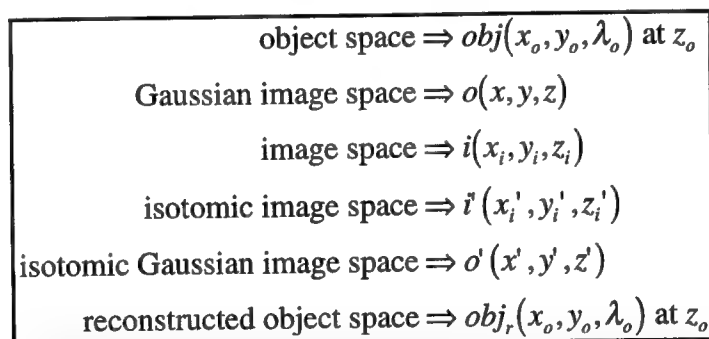


Figure 1.7: The six Cartesian Coordinate systems used in DOIS.

The DOIS prototype was fully characterized, first as individual components and then as a complete system. This characterization is presented in Chapter 5.

Chapter 6 presents both computer generated (CG) and experimentally determined image sets of known targets. As you will see, the linear system theory of Chapter 4

accurately predicts output images formed by DOIS. The CG images are very similar to those determined experimentally.

A multi-spectral, multi-spatial four target testbed was designed and built to further test the performance of DOIS. The four targets include a Tungsten-Halogen greybody source, a multi-line Mercury source and two Helium Neon lasers, a 632.8nm HeNe and a 542nm GreNe. Chapter 7 summarizes the testbed's known spectral characteristics and includes a collection of spectral images and spectral radiance curves measured with DOIS. Appendix A is a catalog of almost 600 images of the four targets that were recorded with the DOIS prototype. The most compelling results are the images and spectral plots of the Mercury doublet at 577nm and 579nm. Without any post-detection processing this doublet is resolved, demonstrating a spectral resolution of less than 2nm!

Chapter 8 presents the object reconstruction algorithms to generate in-focus spectral images, spectral distributions, and full three-dimensional representations. Since not all applications require the same spectral resolution, processing techniques which fall in three general categories are presented, each providing different amounts of deblurring at various computational expense; nearest neighbor, inverse filtering and constrained iterative deconvolution.

The algorithms were implemented in *Mathematica* and applied to reconstruct both CG and experimentally measured objects. The Nearest Neighbor algorithm estimates any spectral image with only three "snapshots" and minimal computational expense. However, greater resolution can be obtained using an SVD inverse Fourier deconvolution with regularization for noise suppression. For completeness, constrained iterative deconvolution is presented, although in practice this method has a relaxation function which must be optimized to a particular application.

All of the deconvolution algorithms provide improved resolution and remove the effects of large targets, higher diffraction orders and stray light. The choice between

reconstruction approaches will ultimately depend on the application dictating such issues as the required spectral/spatial resolution, data storage, computation time and memory.

Chapter 9 summarizes the conclusions drawn during the course of this research, recommending the most effective approach to transition this work into a fieldable image spectrometer. The advantages of DOIS over conventional image spectrometers are discussed. Finally, three designs for future DOIS systems are presented; a dual-waveband design for simultaneous spectral imaging in two spectral bands, such as the mid IR (3 to 5 μ m) and far IR (8 to 12 μ m), and two configurations that perform image spectrometry with no moving parts including a design which records the entire 3D image cube simultaneously in one "snapshot".

2. DOIS - DIFFRACTIVE OPTIC IMAGE SPECTROMETER

The principle shortcoming of DOEs for polychromatic imaging is abundant chromatic aberration. This chapter presents a patented design that exploits this typically unwanted effect to create an image spectrometer [Hinnrichs 1995, Lyons 1995]. Under this dissertation a visible regime Diffractive Optic Image Spectrometer (DOIS), shown in Figure 2.1, was designed, simulated, fabricated, demonstrated and characterized. A DOIS can be designed to operate at ultraviolet, visible or infrared wavelengths for multispectral and hyperspectral imaging in medicine, forensics, industrial and environmental monitoring, as well as military applications.

From Chapter 1, the goal of an image spectrometer is to obtain a set of spectral images of a target, forming an image cube. Each spectral image represents a spectral band or channel, defined by a central wavelength, λ_c , and its spectral bandwidth, $\Delta\lambda$. Referring to equation (1.1), the total number of channels is equal to the total wavelength range divided by the channel bandwidth.

$$\# \text{ of channels} = (\lambda_{\max} - \lambda_{\min})/\Delta\lambda$$

2.1 Basic Scenario

A color computer monitor serves as the polychromatic source object; it will be referred to as the target. The DOE provides both the spatial imaging and the spectral dispersion in this image spectrometer. A conventional monochromatic CCD camera is used to record the image cube. This camera, mounted parallel to the DOE, is stepped along the optical axis, \bar{z} . Each detector location, z , corresponds to a specific spectral channel of the image cube. At each step both an image frame and the corresponding detector location is recorded.

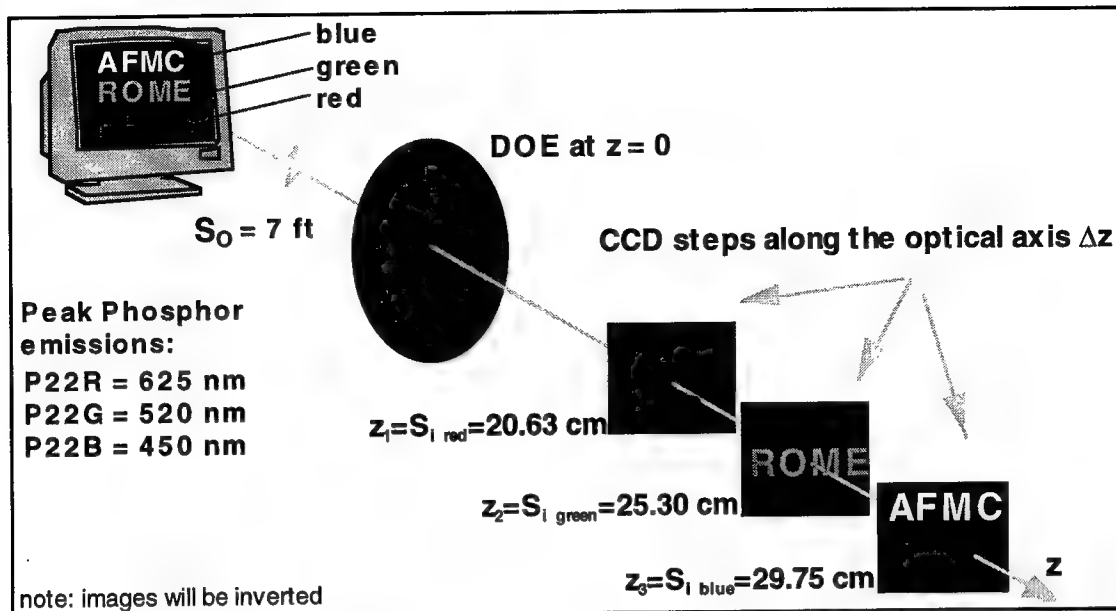


Figure 2.1: DOIS - Diffractive Optic Image Spectrometer basic scenario.

The camera is interfaced to a frame grabber board within a computer for image capture, analysis, display and post detection processing. The images captured by the CCD are a superposition of one channel's infocus image and defocused images of the surrounding channels. These defocused components cause blurring of the desired image. Post-detection, digital image restoration algorithms [Gonzalez 1987] are used to remove the unwanted blurred components, improving the imager's spatial and spectral resolution [Chapter 8].

The diffractive optic 1st order imaging equation relating spectra and the object and image distances, s_o and s_i is given in equation (2.1) [see Chapter 3 for the derivation]:

$$\frac{1}{s_{i\lambda}} = \frac{1}{f_\lambda} - \frac{1}{s_o} = \frac{\lambda}{\lambda_d f_d} - \frac{1}{s_o} \quad (2.1)$$

where f_λ is the focal length at wavelength λ , calculated from f_d and λ_d the DOE design focal length and wavelength.

solving for wavelength:
$$\lambda = \lambda_d f_d \left(\frac{1}{s_{i\lambda}} + \frac{1}{s_o} \right) \quad (2.2)$$

if $s_o \approx \infty$ then $s_{i\lambda} = f_\lambda$:
$$\lambda = \frac{\lambda_d f_d}{s_{i\lambda}} = \frac{\lambda_d f_d}{f_\lambda} \quad (2.3)$$

Figure 2.2 shows the use of equation (2.2) for the scenario in Figure 2.1.

With the target relatively close to DOIS as in the laboratory demonstration, it is best to keep the DOE fixed and the detector stepping, since an accurate target to DOE distance s_o is required. The practical field implementation would be designed for far range targets, $s_o \approx \infty$. At infinite conjugates the object distance s_o isn't sensitive to changes in the lens location, the DOE can be scanned and the detector can be kept stationary, a preferable scenario.

$s_o = 7 \text{ ft}$	$f_d = 20 \text{ cm}$	$\lambda_d = 588 \text{ nm}$
$s_{i1} = 20.63 \text{ cm}$ $\lambda_1 = \lambda_d f_d \left(\frac{1}{s_{i1}} + \frac{1}{s_o} \right)$ $\lambda_1 = 588 * 20 \left(\frac{1}{20.63} + \frac{1}{213.36} \right)$ $\lambda_1 = 625 \text{ nm}$	$s_{i2} = 25.3 \text{ cm}$ $\lambda_2 = \lambda_d f_d \left(\frac{1}{s_{i2}} + \frac{1}{s_o} \right)$ $\lambda_2 = 588 * 20 \left(\frac{1}{25.3} + \frac{1}{213.36} \right)$ $\lambda_2 = 520 \text{ nm}$	$s_{i3} = 29.73 \text{ cm}$ $\lambda_3 = \lambda_d f_d \left(\frac{1}{s_{i3}} + \frac{1}{s_o} \right)$ $\lambda_3 = 588 * 20 \left(\frac{1}{29.75} + \frac{1}{213.36} \right)$ $\lambda_3 = 450 \text{ nm}$

Figure 2.2: Algorithm for calculating wavelength from image distance, s_i .

When a target such as AFMC ROME LAB spelled out on a black background in blue, green and red respectively, is imaged with DOIS, each color or word will come to focus in a different position z_λ . The chromatic focal shift, $\Delta f = \frac{\Delta \lambda \lambda_d f_d}{\lambda_1 \lambda_2}$, is so severe that

the separation between a blue AFMC and a red LAB is almost 10 cm. This extreme fall off with color provides this image spectrometer with a FWHM spectral bandwidth ranging from 1 to 1.5 nm throughout the visible spectrum and over 100 possible spectral channels without post detection image processing. Once a series of images is captured, the image

cube can be displayed as series of spectral images, a normalized spectral radiance curve (intensity verses wavelength) for each pixel of interest or a two-dimensional spatial/spectral cross-section, xz_λ or yz_λ , of the image cube. The stepping can be controlled to tune to one particular channel, to step through a narrowband, wideband or the entire visible range in equal increments of dz , $d\lambda$, or any variation of user controlled steps. With proper control, a continuous video can be recorded matching the frame and scan rates, to calibrate the wavelength to time or frame number.

2.2 Experimental Demonstration with a RGB monitor

The Image Spectrometer of Figure 2.1 was built and demonstrated at Rome Laboratory's Photonic Center and is described below. This monitor demonstration is presented to facilitate an understanding of the basic operation and performance of DOIS. A much more analytical testing of the characteristics, performance and limitations of this Image Spectrometer is found in the following chapters; Chapter 5. Prototype Characterization and Chapter 7. Prototype demonstration with four targets.

The DOE is a 5 cm diameter, BK-7, 2 level phase grating with a design focal length, $f_d = 20$ cm at the design wavelength, $\lambda_d = 588$ nm. The CCD camera is a SONY XC-75, monochrome video camera. The sensing area is 1/2 inch with 768 (H) x 494 (V) pixel elements. Each pixel is $8.4 \mu\text{m} \times 9.8 \mu\text{m}$. The approximate pixel size of $10 \mu\text{m} \times 10 \mu\text{m}$ will be used for simplicity and to account for dead space between pixels. The camera was connected to a framegrabber board in a Macintosh PowerPC 8100/100AV. The images were recorded and displayed with *MacPhase* by Otter Solution, an image capture, analysis and visualization software package.

The target simulation monitor used in this demonstration is an AppleColor™ High Resolution RGB monitor. Each pixel of an RGB monitor is a cluster of three phosphor dots: a red, a green and a blue. All colors displayed on the monitor are a combination of these three basic colors. For instance, white is equal amounts of all three, bright yellow is equal amounts of red and green, pink is blue and red, and turquoise is blue and green. Adobe Photoshop™ is a software program which allows precise selection of text colors and was used to create the display target. The words AFMC ROME LAB were spelled out in Photoshop™ on a black background. The color picker was used to select 100% blue font color for the AFMC, and 100% green and red for the ROME and LAB respectively. Figure 2.3 is an example of the color picker window in Adobe Photoshop™ shown here with 100% blue for the AFMC text.

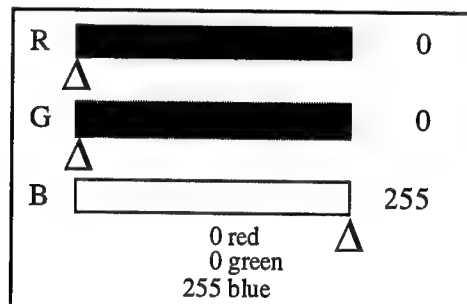


Figure 2.3: Example of the color picker window in Adobe Photoshop™ for the blue AFMC target.

Figure 2.4 shows the relative spectral emission curves of the red, green & blue phosphors. The general wideband spectral emission curves for the three phosphors; blue P22B, green P22G and red P22R [Fink 1989]. Experimental characterization of the monitor's spectral radiance was performed with an Oriel grating monochrometer and Newport power meter . This characterization confirmed the wide band spectral emissions of the blue and green phosphors. However, the red phosphor emitted in narrow lines, with two strong red lines, 625 and 617 nm, a few orange lines around 594 nm and even a few blips in the green region. Since the red emission differed so greatly from the textbook

P22R spectral curve, both are plotted in Figure 2.4. Unsuccessful attempts were made to verify the spectral radiance of the monitor with the manufacturer. The line nature of the red could indeed be from the P22R phosphor or a possible coating or filter on the monitor screen, and the lines in the green region could be from misalignment of the electron beam accidentally exciting the green phosphor dots. In any event, the band and line emission of this monitor makes an excellent demonstration target.

The horizontal curve in Figure 2.4 is the DOIS minimum detection threshold. DOIS is able to detect a faint green, an orange and the two strong red lines of the red phosphor and the continuous wideband emissions of the blue and green.

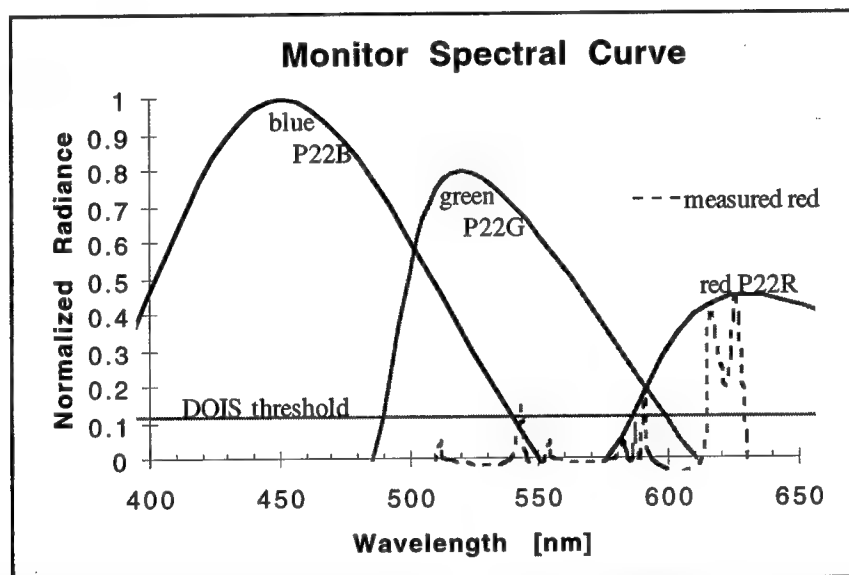


Figure 2.4: Phosphor emission curves for red (P22R), green (P22G), and blue (P22B) phosphor, the measured blue and green agree with wideband textbook curves however the measured red differs dramatically.

Spectral images of the monitor taken with DOIS are shown in Figure 2.5. These are raw (256 x 256) images, displayed without any processing. The images depict the band emission of P22B, P22G and the line nature of P22R. Scanning from 400nm to 650nm the blue AFMC is present alone (a) from 400nm to 490nm, at 490 the green ROME cuts on and both AFMC and ROME can be seen in varying intensities (b) until the blue falls off completely at 540nm. The green ROME is continually present until 595nm. The intensity of

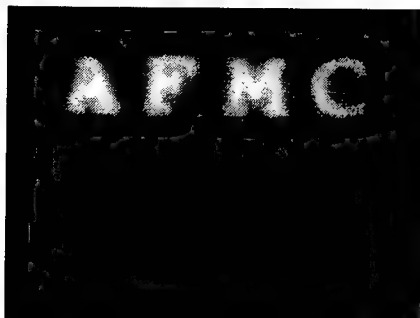


Figure 2.5: Spectral images recorded with DOIS. The target is text displayed on an AppleColor™ high resolution RGB monitor.

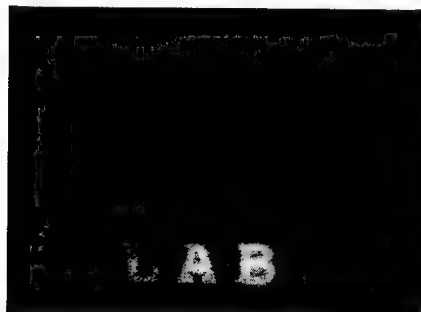
(a) $\lambda = 452$ nm, blue AFMC, mid blue focus. Blurring is from the wide band emissions of P22B.



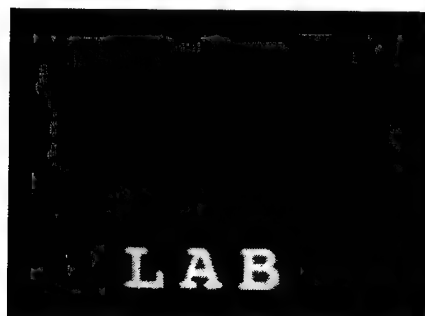
(b) $\lambda = 520$ nm, green ROME, mid green focus with the blur from the band emissions of P22G. Note that corresponding to Figure 2.4, P22B is still emitting.



(c) $\lambda = 594$ nm, green ROME and red LAB. Both P22G and P22R have slight emissions at this orange line.



(d) $\lambda = 617$ nm, red LAB. First strong P22R line with a halo from 625 nm line.



(e) $\lambda = 625$ nm, red LAB. Strongest P22R line. Note that P22G is completely cutoff.

the red LAB pops in and out as the scan progresses from 540nm to 650nm. A very dim LAB shows up at 542nm, then again at 594nm as in (c). It is absent until 615, with a crisp focus at 617 and 625nm, finally disappearing at 630nm.

2.2.1 Blue Background Demonstration

The monitor demonstration was repeated with a blue background instead of the black. This simulates a scenario with a target surrounded by a bright background (the sky).

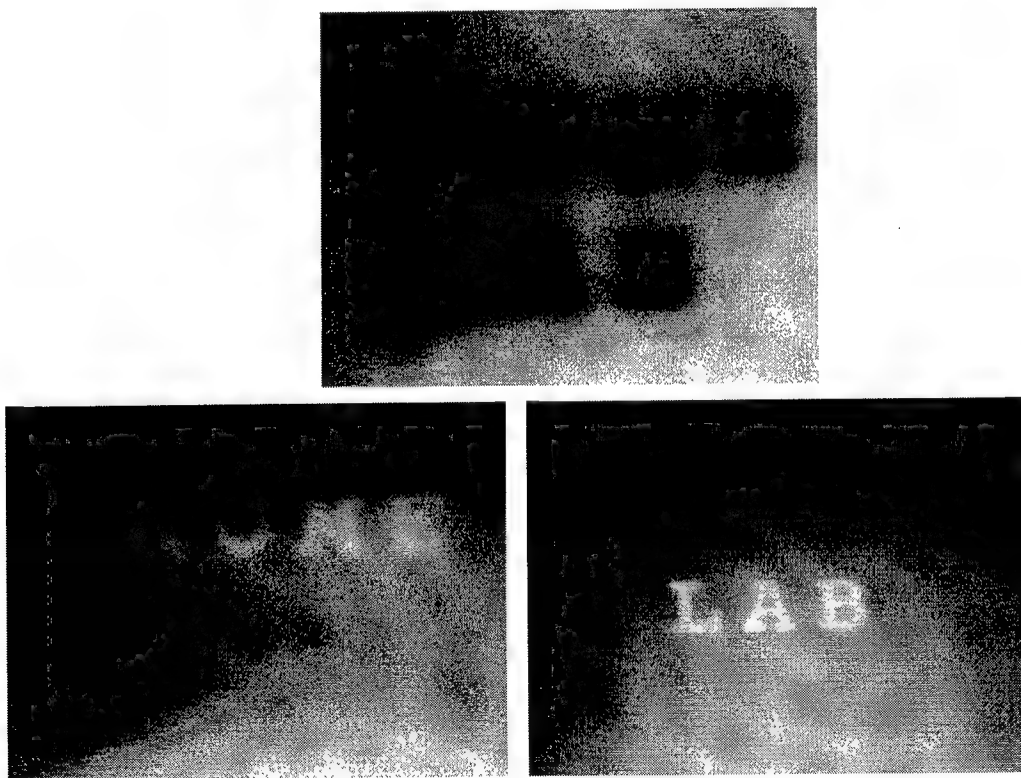


Figure 2.6: Images from green ROME and red LAB on a blue background (a) blue focus (b) green (c) red.

As shown above, DOIS is able to distinguish the targets. The defocused blue light adds to the noise floor and decreases the SNR. Notice that the green ROME is clear even though the blue phosphor is still emitting in that region.

2.3 Continuous Magnification

Recall from Figures 1.5 and 1.6 that the magnification changes with wavelength. Since the CCD pixel configuration is fixed, the image cube is recorded with non-uniform sampling. This creates problems in registering target information between spectral slices and limits the accuracy of image reconstruction algorithms.

2.3.1 Post-detection image resampling

To compensate for the changing magnification the image cube can be resampled to approximate constant magnification. Illustrated in Figure 2.7, a pixel footprint or field-of-view (FOV) is defined at the smallest magnification. Each spectral image is then resampled by integrating over the same pixel FOV, Ω_{pixel} .

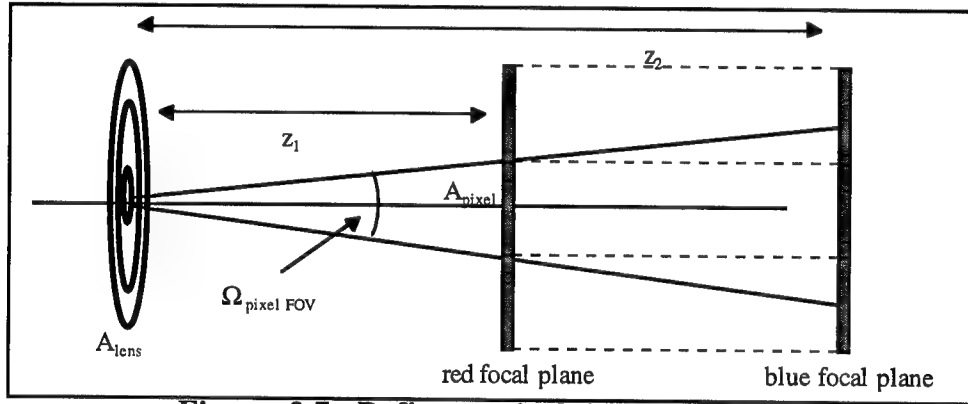


Figure 2.7: Define a pixel footprint Ω_{pixel} .

$$\Omega_{\text{pixel}} = \frac{A_{\text{pixel}}}{z_{\text{smallest}}^2} \quad (2.4)$$

$$\Omega_{\text{pixel}} = \frac{A_{\text{pixel}}}{z_1^2} = \frac{\text{integration area}}{z_2^2} \quad (2.5)$$

$$\Omega_{\text{pixel}} = \frac{10\mu\text{m} \times 10\mu\text{m}}{20\text{cm}^2} = \frac{\text{integration area}}{30\text{cm}^2} \quad (2.6)$$

$$\text{integration area} = 225\mu\text{m}^2 = 1.5\text{pixels} \quad (2.7)$$

In order to form a constant magnification image cube with each spectral image having 256x256 spatial pixels, the red image at $z=20\text{cm}$ is recorded with 256x256 and the

blue image at $z=30\text{cm}$ will need to be recorded with 384×384 pixels, then interpolated to fit the 256×256 spectral slices of the image cube.

Problems can arise with this technique. Resampling the detected image cube requires averaging a non-integral number of pixels. This can cause blurring of edges and inaccurate pixel registration. A more accurate optical method of obtaining an image cube with constant magnification is presented in section 2.3.2.

2.3.2 Optical designs for constant magnification

A second approach to DOIS imaging with constant magnification is a redesigned optical train. A refractive lens is added between the DOE and CCD to relay and magnify the DOE images [Lyons 1997]. The relay lens is the scanned element, and its position dictates the spectrum of the recorded image.

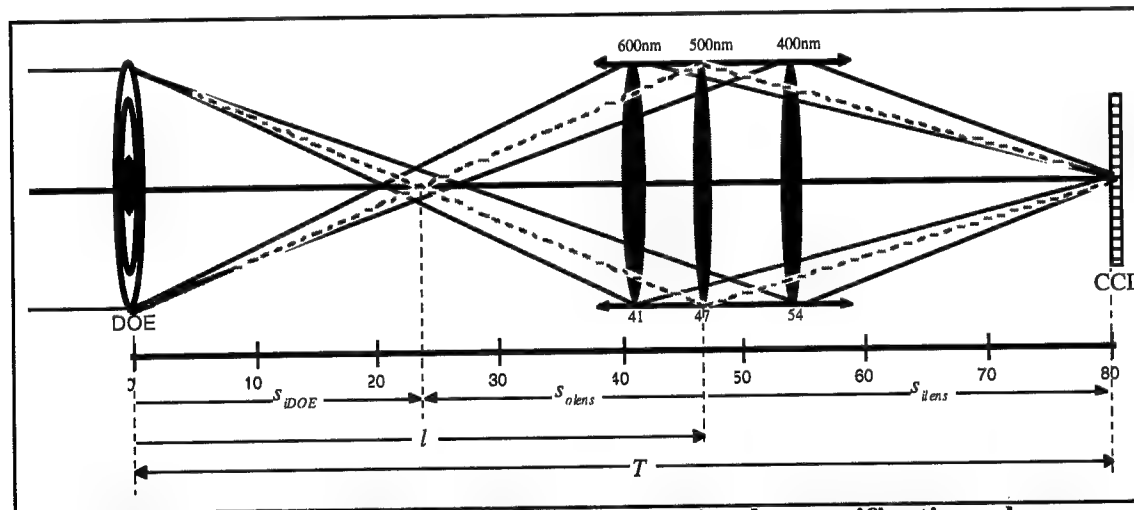


Figure 2.8: Relay DOIS design with minimal magnification change.

Shown in Figure 2.8, the total tube length or optical train length, T , is held constant. The DOE still performs the dispersion and forms an image space, however a refractive, non-dispersive lens is placed after the DOE image space relaying the DOE images to the CCD camera. The images formed by this intermediate lens on the CCD will

be erect and the spectra will depend on the lens' position, l , and the target's object distance, $s_{otarget}$. The following equations derive the relationship between spectra and lens location.

Starting from equation (2.2):
$$\lambda = \lambda_d f_d \left(\frac{1}{s_{iDOE}} + \frac{1}{s_{otarget}} \right)$$

$$s_{iDOE} = l - s_{olens} \quad (2.8)$$

$$s_{olens} = \frac{f_{lens} s_{ilens}}{s_{ilens} - f_{lens}} \quad (2.9)$$

$$s_{ilens} = T - l \quad (2.10)$$

$$s_{olens} = \frac{f_{lens}(T - l)}{T - l - f_{lens}} \quad (2.11)$$

$$s_{iDOE} = l - \frac{f_{lens}(T - l)}{T - l - f_{lens}} = \frac{lT - l^2 - 2f_{lens}l - f_{lens}T}{T - l - f_{lens}} \quad (2.12)$$

$$\lambda = \lambda_d f_d \left(\frac{T - l - f_{lens}}{lT - l^2 - 2f_{lens}l - f_{lens}T} + \frac{1}{s_{otarget}} \right) \quad (2.13)$$

The selected wavelength λ is calculated in equation 2.13 from the DOE design constants $\lambda_d f_d$, the tube length T , the focal length of the relay lens f_{lens} , the target's object distance $s_{otarget}$, and the lens position l .

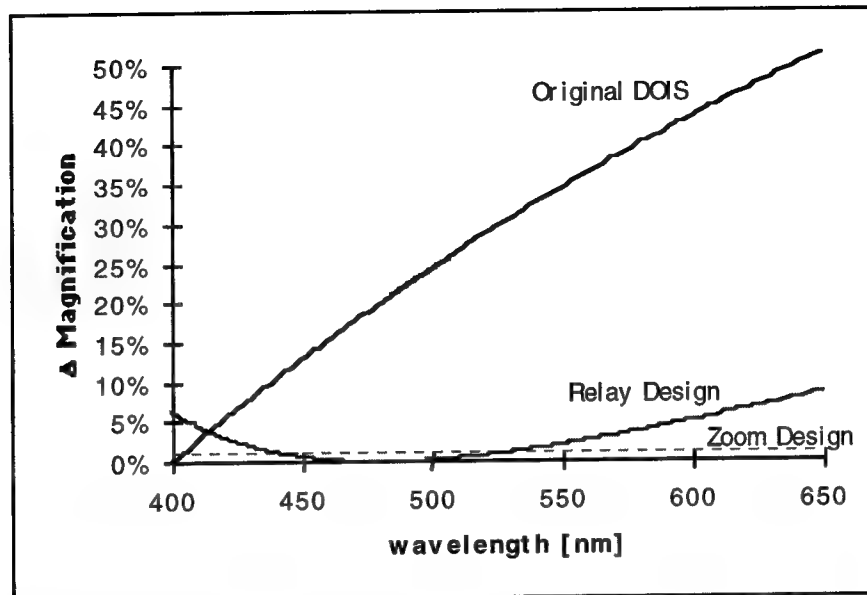


Figure 2.9: Magnification change vs. wavelength for original, relay and zoom designs.

The change in magnification verses wavelength for this relay design is plotted in Figure 2.9 along with that of the original design. Notice that although the magnification isn't constant, the change over the entire spectral band is substantially reduced to less than 10%. To further improve the changing magnification, the relay lens can be replaced with a pair of lenses forming a zoom lens, shown in Figure 2.10. The constant magnification of the zoom lens design is shown as a dotted line in Figure 2.9.

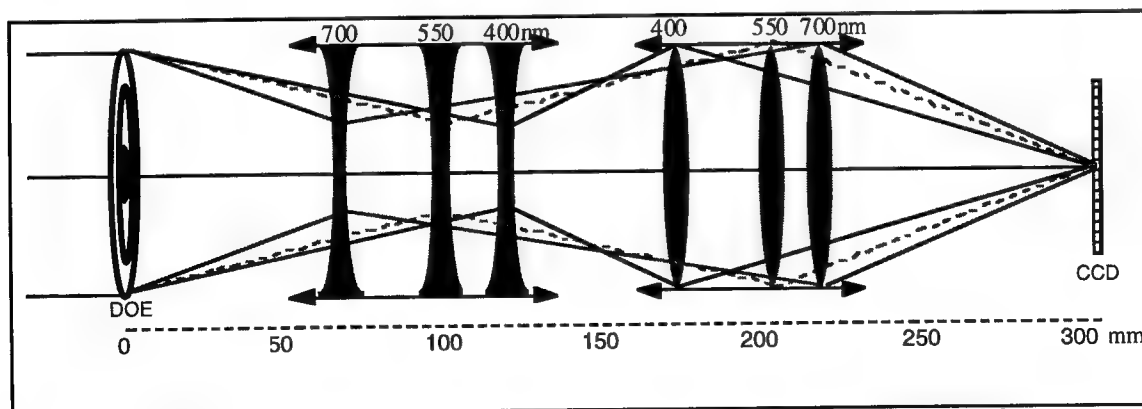


Figure 2.10: Zoom DOIS design with constant magnification.

3. DIFFRACTIVE OPTICAL ELEMENTS

The three main considerations in designing an optical system are cost, weight and performance. Diffractive optical elements (DOEs) have the potential to improve all three. DOEs have a spectral dispersion inversely proportional to wavelength, whereas refractive optical elements have dispersion proportional to wavelength. Typically lens designers combine these dispersion characteristics to obtain an achromat [Ward 1971, Stone 1990]. However in this system the DOE dispersion is used alone, and exploited to create an imaging spectrometer.

3.1 *Fresnel Zone Plate*

The potential usefulness of diffractive optical elements has been known for years. [Miyamoto 1961, Lesem 1969]. The problem with implementing them in real systems has been the lack of a process that can design and reliably produce the elements to the required tolerances necessary for high diffraction efficiency. Figure 3.1 (a) shows an example of a Fresnel zone plate phase profile needed to achieve high efficiency. The 2π phase depth corresponds to a material etch depth of about $2\mu\text{m}$ for midinfrared radiation and $1\mu\text{m}$ for visible. Several research teams are exploring techniques to produce this continuous phase profile with laser writers or greyscale masks [Morris 1994, O'Shea 1994]. However, it is common practice to approximate the continuous phase profile by quantized discrete phase levels [Goodman 1970, Swanson 1989]. Figures 3.1 (b), and (c) show the Fresnel zone plate phase profile quantized into two and four phase levels, respectively. The two level profile results in an efficiency of 40% and the four level profile results in an efficiency of 81%. For most systems, it is necessary to achieve diffraction efficiency of 99% or greater, this can be achieved with 16 levels created with 4 masks. Figure 3.2 shows the diffraction efficiency as a function of the number of phase levels and required masks. Since this

dissertation is only meant as a proof-of-concept, 40% is tolerable and a 2 level phase plate was fabricated with one mask.

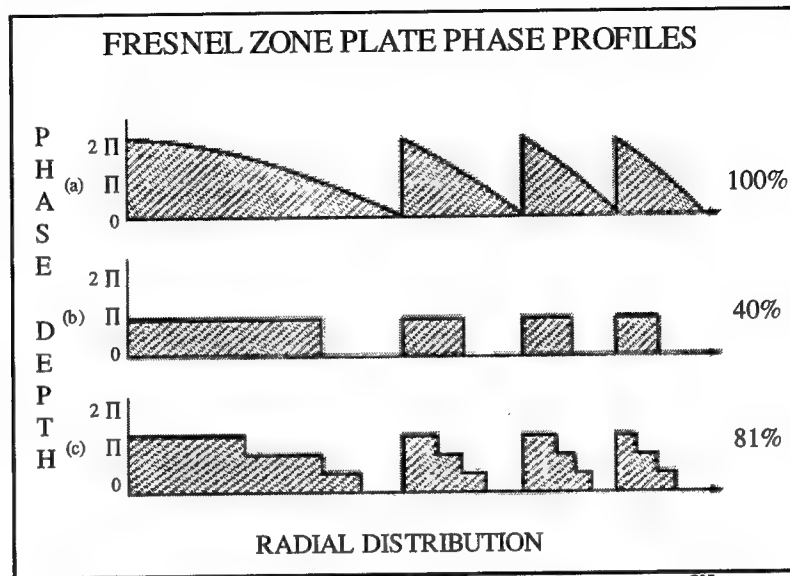


Figure 3.1: Fresnel zone plate phase profiles.

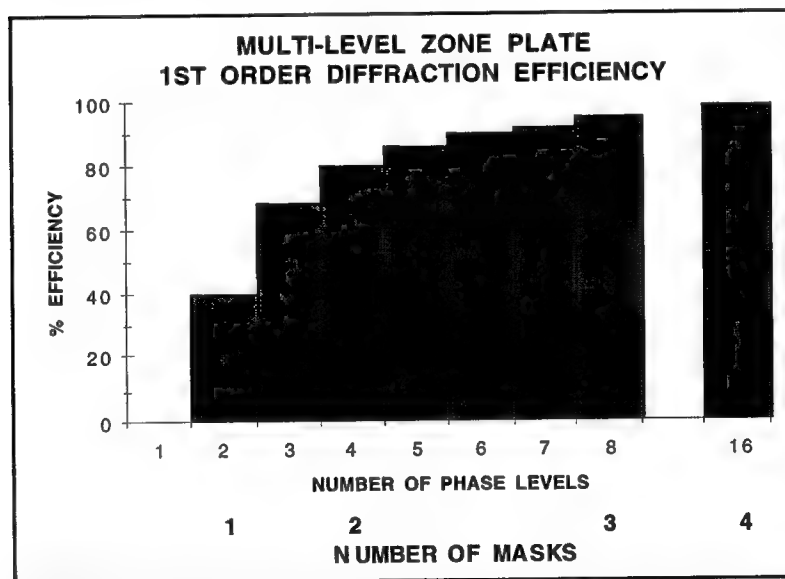


Figure 3.2: Diffraction efficiency vs. number of masks and phase levels.

3.2 DOE design and characteristic equations

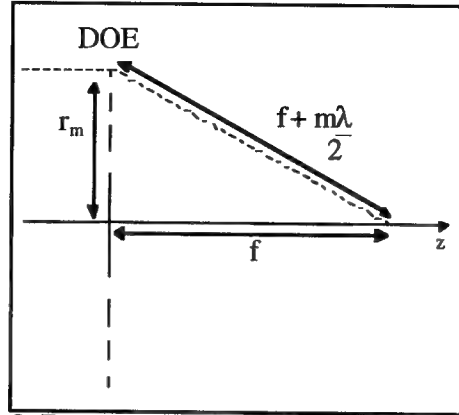


Figure 3.3 Ray trace that determines zone radii.

The zones of the Fresnel Zone Plate are defined when the optical path difference between adjacent zones is $\lambda/2$, causing constructive interference, shown in Figure 3.3 and characterized by equation 3.1 [Hecht 1989]. From Pythagorean's theorem, the radius of the m^{th} zone, r_m , is:

$$r_m^2 + f^2 = \left(f + m\frac{\lambda}{2}\right)^2$$

$$r_m = \sqrt{fm\lambda + m^2\left(\frac{\lambda}{2}\right)^2} \quad (3.1)$$

where m is the zone counter, r_m is the value of the m^{th} radius, λ is the design wavelength, and f is the primary focal length, corresponding to the 1st diffractive order.

$$\text{since } m\frac{\lambda}{2} \ll f$$

$$r_m^2 = fm\lambda \quad (3.2)$$

Solving for f :

$$f = \frac{r_m^2}{m\lambda} \quad (3.3)$$

The zone radii are calculated to focus a particular design wavelength, λ_d , at a design focal length, f_d .

$$r_m^2 = f_d m \lambda_d \quad (3.4)$$

Once the DOE is fabricated with these fixed zones determined from the design parameters, the focal position at wavelengths other than the design wavelength can be found from substituting equation (3.4) into (3.3):

$$f = \frac{r_m^2}{m \lambda} = \frac{f_d m \lambda_d}{m \lambda}$$

$$f(\lambda) = \frac{\lambda_d f_d}{\lambda} \quad (3.5)$$

This wavelength dependence is seen as chromatic aberration where the effective focal length is inversely proportional to wavelength. Adding it to the Gaussian lens formula yields the diffractive optic 1st order imaging equation:

$$\frac{1}{s_i(\lambda)} = \frac{1}{f(\lambda)} - \frac{1}{s_o} = \frac{\lambda}{\lambda_d f_d} - \frac{1}{s_o} \quad (3.6)$$

where s_o is the object distances and $s_i(\lambda)$ is the spectral image distance.

A critical figure of merit for this application is the first order diffraction efficiency, η_1 . It is dependent on the etch depth, the operational wavelength and the number of phase levels etched into the grating. The diffraction efficiency can be calculated from equation (3.7) below, and is plotted in Figure 3.4 for a 2 level zone plate and a high efficiency 16 level DOE [Swanson 1989].

$$\eta_m^N = \left[\frac{\sin\left(\pi\left(\frac{(n-1)d}{\lambda} - m\right)\right)}{\pi\left(\frac{(n-1)d}{\lambda} - m\right)} \right]^2 \left[\frac{\sin\left(\pi\left(\frac{(n-1)d}{\lambda N}\right)\right)}{\pi\left(\frac{(n-1)d}{\lambda N}\right)} \right]^2 \quad (3.7)$$

where: $d = \lambda_d / (n-1)$

η is the diffraction efficiency

n is the refractive index of the substrate

d is the etch depth

m is the diffracted order of interest, typically $m=1$

λ_d is the design wavelength

λ is the operational wavelength

N is the number of levels in the grating, DOIS prototype is 2

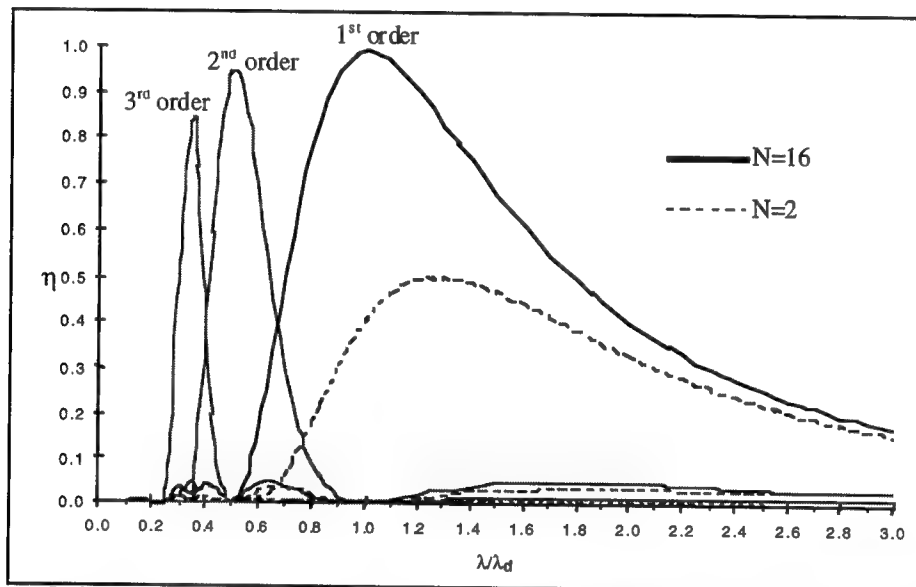


Figure 3.4: Diffraction Efficiency vs. Wavelength for $N=2$ and $N=16$.

The curve in Figure 3.4 is useful in selecting the proper design wavelength for applications where it is important to have high efficiency through a spectral range and not at just one wavelength, such as in DOIS. Note that the efficiency falls off much faster for smaller wavelengths, therefore λ_d should be selected near the shorter wavelength end of the range not simply the center wavelength.

An interesting note is that the peak for the two level grating is not at $\lambda/\lambda_d=1$ but at 1.3. This leads to the conclusion that calculation for etch depth, d , which is formulated for a continuous grating, isn't optimal when you have only 2 levels.

3.3 Fabrication of Multilevel Profiles

Swanson and Veldkamp developed a scheme that can accurately and reliably produce these multilevel diffraction surfaces with diffraction efficiencies in excess of 90% [Veldkamp1989]. Their technique takes advantage of technology the integrated circuit industry has developed for the miniaturization of circuits. Three essential tools that were developed are electron beam pattern generators, reactive ion etchers, and mask aligners. E-beam pattern generators are capable of drawing binary amplitude patterns with feature sizes of $0.1\mu\text{m}$ and positioning the features to an even greater accuracy. Reactive ion etchers can etch a binary profile to depths of a few microns with an accuracy on the order of tens of angstroms. Mask aligners are used routinely to align two patterns with an accuracy of fractions of a micron. These are key technological advances that make it possible to produce the high quality diffractive phase profiles.

Electron beam pattern generators produce masks that have binary transmittance profiles. A thin layer of chrome on an optically flat quartz substrate is patterned by the e-beam machine. The input to the e-beam pattern generator is a file stored on a computer tape and properly formatted for the particular machine. For multilevel diffractive elements the number of phase levels in the final diffractive element constructed from these masks is $2n$, where n is the number of masks. For example, only four masks will produce 16 phase levels, resulting in an efficiency of 99%.

The binary amplitude masks produced from the pattern generator are actually low efficiency zone plates themselves, but are used to construct the multilevel optical element. The fabrication process using the first mask is shown in Figure 3.5 . The optical surface on which the diffractive profile is to be etched is coated with a layer of photoresist. The e-beam generated mask is then placed over the substrate and illuminated with a standard UV photoresist exposure system. The photoresist is then developed, resulting in a properly

patterned layer of photoresist. The photoresist acts as an etchstop for the reactive ion etching.

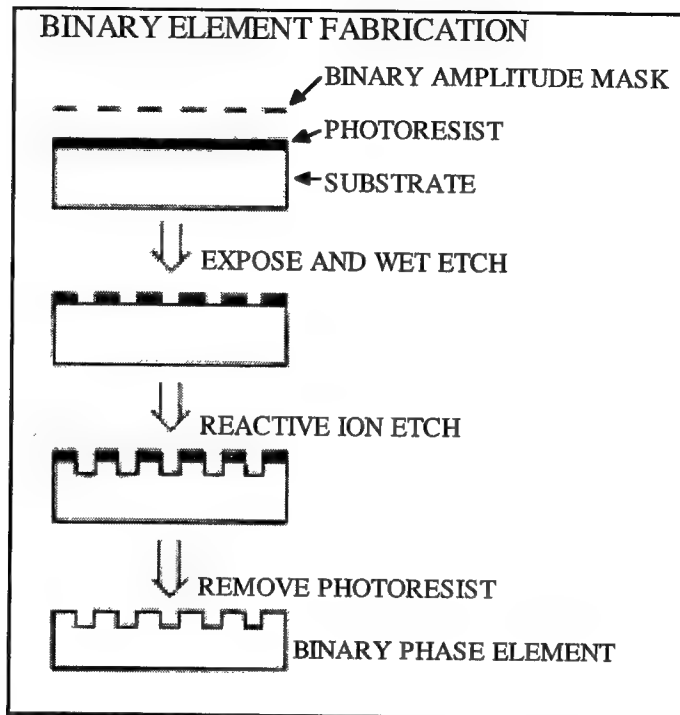


Figure 3.5: Photolithography multilevel fabrication algorithm.

Reactive ion etching is a process in which an RF electric field excites a gas, producing ions. The ions react with the material of the substrate and etch away the surface at a controlled rate. The reactive ion etching process is anisotropic, so the vertical side walls of the discrete phase profile are retained. Typical etch rates are on the order of 100Å to 200Å per minute. As an example, the required first-level etch depth for a BK-7 substrate to be used at a wavelength of $.588\text{ }\mu\text{m}$ is $1.176\text{ }\mu\text{m}$. The necessary etch time is on the order of an hour. Numerous elements can be etched simultaneously. After the pattern of the first mask has been etched into the substrate, any residual photoresist is stripped away.

For multilevel structures the same procedure is then repeated on the optical substrate, only this time the second mask and etching to one-half the depth of the first etch. For the second and subsequent masks an additional complication arises. These masks have to be accurately aligned to the already existing pattern produced from the first etch.

Commercially available mask aligners are capable of aligning two patterns to a fraction of a micron. This accuracy is sufficient to retain diffraction-limited performance for most multilevel structures designed to operate in the visible and infrared.

This technique was used at The Nanofabrication Facility at Cornell University to fabricate a DOE lenses for a DOIS prototype [Lyons 1994].. The DOE is a BK-7, 2 level Fresnel Phase Plate with approximately 2200 zones and a minimum feature size of $2.5\mu\text{m}$. Figure 3.6 is two scanning electron microscope (SEM) photos of the rings.

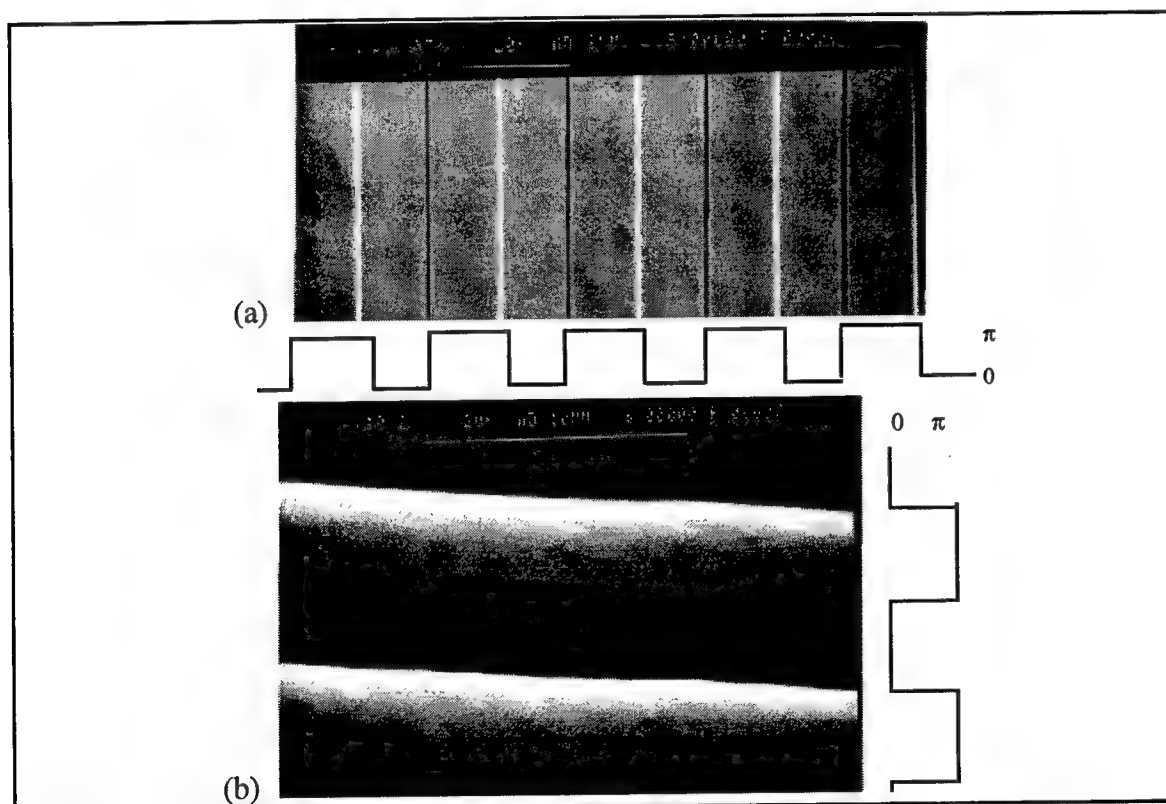


Figure 3.6: SEM photos of DOE rings. (a) Top view, feature size is $\approx 10\mu\text{m}$. (b) Side view of the outermost rings, feature size is $\approx 2.5\mu\text{m}$.

3.4 The Incoherent Point Spread Function

The key parameter for a successful simulation and reconstruction is an accurate psf, h . Since the equivalence between DOEs and lenses has been established [Sweatt 1979], the three-dimensional psf of a lens can be adapted to the DOE. The theoretical diffraction limited and experimentally measured intensity point spread functions are presented below.

3.4.1 Diffraction limited incoherent psf

Born and Wolf describe the normalized three-dimensional distribution of intensity in the neighborhood of focus, $I(v, u)$, for a rotationally symmetric optical system as a convergent series of Bessel functions with the two equivalent expressions [Born 1989].

$$h(v, u) = I(v, u) = \left(\frac{2}{u}\right)^2 \left[U_1^2(v, u) + U_2^2(v, u) \right] \quad (3.8)$$

$$h(v, u) = \left(\frac{2}{u}\right)^2 \left[1 + V_0(v, u) + V_1(v, u) - 2V_0(v, u) \cos\left\{\frac{1}{2}\left(u + \frac{v^2}{u}\right)\right\} - 2V_1(v, u) \sin\left\{\frac{1}{2}\left(u + \frac{v^2}{u}\right)\right\} \right] \quad (3.9)$$

where:

$$U_n(v, u) = \sum_{s=0}^{\infty} (-1)^s \left(\frac{u}{v}\right)^{n+2s} J_{n+2s}(v) \quad (3.10)$$

$$V_n(v, u) = \sum_{s=0}^{\infty} (-1)^s \left(\frac{v}{u}\right)^{n+2s} J_{n+2s}(v)$$

$$u = \frac{2\pi}{\lambda} \left(\frac{a}{f}\right)^2 z \quad \text{or} \quad z = \frac{\lambda}{2\pi} \left(\frac{f}{a}\right)^2 u \quad (3.11)$$

$$v = \frac{2\pi}{\lambda} \left(\frac{a}{f}\right) r = \frac{2\pi a}{\lambda f} \sqrt{x^2 + y^2} \quad \text{or} \quad r = \frac{\lambda}{2\pi} \left(\frac{f}{a}\right) v \quad (3.12)$$

Figure 3.7 is a density plot of equation (3.8), in terms of the dimensionless variables u and v , and the scaled dimensions $r[\mu\text{m}]$ and $z[\mu\text{m}]$ calculated from the specific parameters of the DOIS prototype design. In three-dimensions $h(v, u)$ is circularly symmetric about the optical axis, u . When evaluated with specific design parameters, λ , f ,

and aperture radius, a , the intensity point spread function will be scaled but maintain the fundamental spheroidal form.

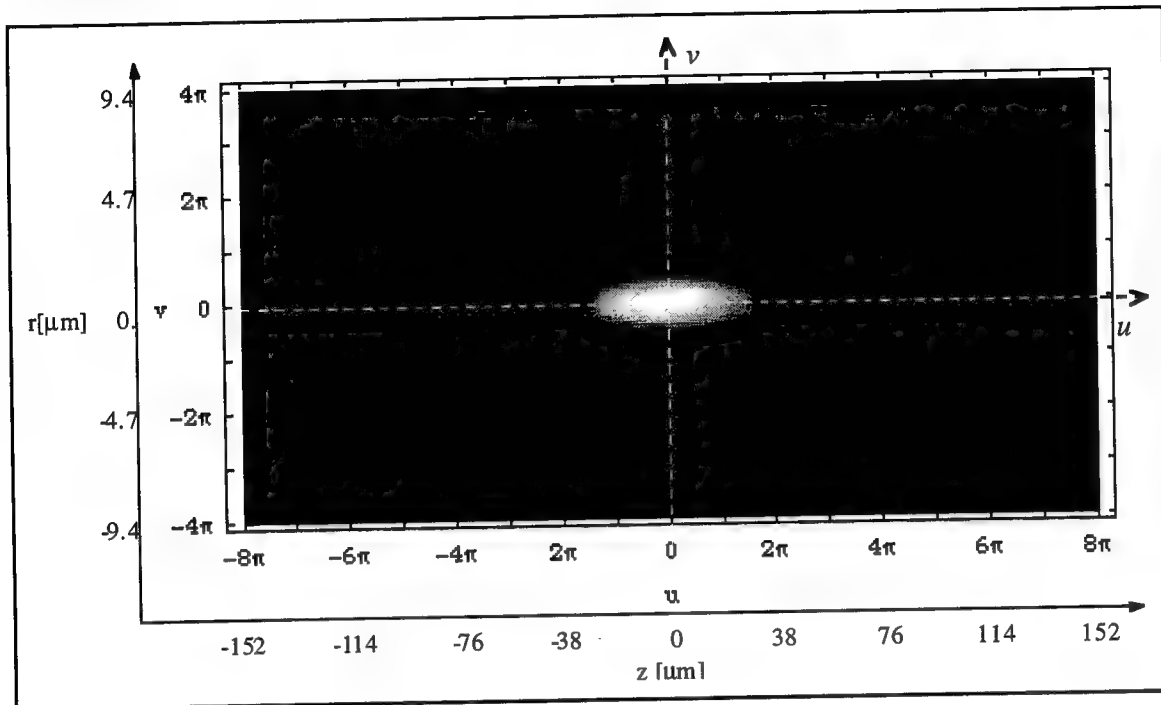


Figure 3.7: A density plot of the diffraction limited intensity psf, $h(v,u)$, it is rotationally symmetric around the u axis.

For graphical analysis it is appropriate to look at three different views or cross-sections. The first is a two-dimensional spatial psf in the plane perpendicular to the optical axis at focus, $h(v,0)$. Shown in Figure 3.8, this is a cross-section of an infocus monochromatic point source. It displays the expected amount of image degradation or blurring applied to spatially adjacent coordinates and is a limiting factor in determining the spatial resolution. Substituting $u=0$ into equation (3.8):

$$h(v,0) = \left[\frac{2J_1(v)}{v} \right]^2 \quad (3.13)$$

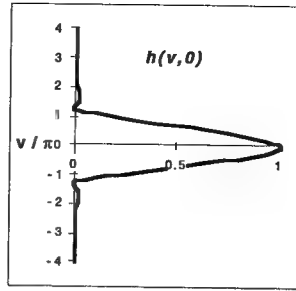


Figure 3.8: A theoretical plot of $h(v,0)$ in the focal plane.

When rotated around the optical axis this pattern is known as the airy disk. The majority of the intensity falls between the first zeros of the Bessel function at $\Delta r = \pm 1.22\lambda F/\#$. For the F/4 DOE designed for the prototype $\Delta r \approx 5.7\mu\text{m}$. This is smaller than the $10\mu\text{m}$ pixels of the CCD detector. Therefore, once detected, the infocus diffraction limited incoherent psf will look like a delta function.

The second view of interest is an intensity plot through focus, $h(0,u)$, along the optical axis, normally considered the depth of focus. Since DOIS interprets z as wavelength, $h(0,u)$ represents the expected amount of blurring applied to adjacent spectral slices. It is the limiting factor that determines the spectral resolution and bandwidth. Substituting $v=0$ into equation (3.9):

$$h(0,u) = \left[\frac{\sin u/4}{u/4} \right]^2 \quad (3.14)$$

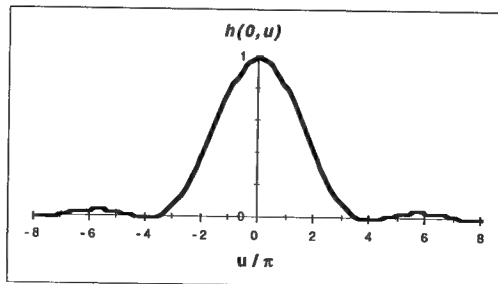


Figure 3.9: A theoretical plot of $h(0,u)$ along the optical axis.

In Figure 3.9, the first zero in intensity along the axis is at $\Delta z = \pm 8\lambda F/\#^2$. For the prototype $\Delta z = \pm 75\mu m$, predicting a theoretical incoherent diffraction limited spectral resolution of $\Delta\lambda \approx 0.256\mu m$.

The third view of the psf is along the geometrical boundary, where $u=v$. Calculated in equation (3.15) and plotted in Figure 3.10, $h(v,v)$ dictates the blur seen from coordinates that are different in both spectra and spatial location. Substituting $u=v$ into equation (3.9):

$$h(v,v) = \frac{1 - 2J_0(v)\cos v + J_0^2(v)}{v^2} \quad (3.15)$$

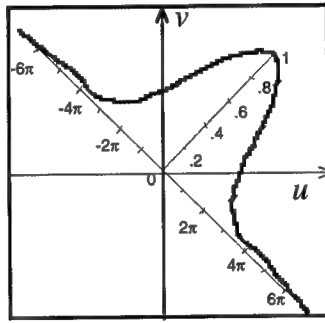


Figure 3.10: A theoretical plot of $h(v,v)$ where $u=v$.

3.4.2 Experimentally measured incoherent psf

Unfortunately, because of aberrations, noise and other errors, the blurring encountered in real systems is greater than predicted by the diffraction limited intensity point spread function. Another approach to obtain the three-dimensional incoherent psf is by direct experimental measurement using a laser illuminated pinhole to simulate a monochromatic point source. The following discusses the validity of simulating the incoherent intensity psf with images of a coherent pinhole.

3.4.2.1 Coherent vs. Incoherent Imaging

Coherent imaging is described by the amplitude convolution equation [Goodman 1968]:

$$U_{im}(x_i, y_i) = \iint \tilde{h}(x_i - x_o, y_i - y_o) U_{obj}(x_o, y_o) dx_o dy_o \quad (3.16)$$

where U_{im} represents the amplitude distribution in image space from the amplitude distribution in object space U_{obj} , and $\tilde{h}(x_i, y_i)$ is the coherent or amplitude impulse response. However it is actually the image's intensity I_{im} which is detected:

$$\text{coherent:} \quad I_{im}(x_i, y_i) = \left| \iint \tilde{h}(x_i - x_o, y_i - y_o) U_{obj}(x_o, y_o) dx_o dy_o \right|^2 \quad (3.17)$$

Incoherent imaging is a linear mapping of intensity described by the intensity convolution integral:

$$\text{incoherent:} \quad I_{im}(x_i, y_i) = \iint \left| \tilde{h}(x_i - x_o, y_i - y_o) \right|^2 I_{obj}(x_o, y_o) dx_o dy_o \quad (3.18)$$

where I_{obj} is the object's intensity distribution equal to $|U_{obj}|^2$, and $|\tilde{h}(x_i, y_i)|^2$ is the incoherent or intensity impulse response, previously represented by $h(x_i, y_i)$.

To find the impulse response, the input object $U_{obj}(x_o, y_o)$ is a perfect point source represented by a delta function, $\delta(x_o, y_o)$. Substituting the delta function into equation (3.17) for coherent imaging yields:

$$\begin{aligned} \text{coherent:} \quad I_{im}(x_i, y_i) &= \left| \iint \tilde{h}(x_i - x_o, y_i - y_o) \delta(x_o, y_o) dx_o dy_o \right|^2 \\ &= \left| \tilde{h}(x_i, y_i) \right|^2 \end{aligned} \quad (3.19)$$

Likewise for incoherent imaging, substituting the delta function into equation (3.18)

where $I_{obj}(x_o, y_o) = |\delta(x_o, y_o)|^2 = \delta(x_o, y_o)$:

$$\begin{aligned}
I_{im}(x_i, y_i) &= \iint |\tilde{h}(x_i - x_o, y_i - y_o)|^2 \delta(x_o, y_o) dx_o dy_o \\
\text{incoherent:} \quad & \\
&= |\tilde{h}(x_i, y_i)|^2
\end{aligned} \tag{3.20}$$

Showing that if the input object was indeed a delta function point source, the recorded intensity would represent the incoherent or intensity impulse response, $h(x_i, y_i) = |\tilde{h}(x_i, y_i)|^2$, of the system. However in practice every target has some finite width, thus the perfect delta function point source does not exist.

The implications of the difference between coherent and incoherent illumination can be seen if the object being imaged is a pair of delta function point sources separated by the Rayleigh distance denoted by x_r [Gaskill 1978]. If the two sources are incoherent, the total image irradiance is simply the sum of the image irradiance distributions of the individual sources:

$$\text{incoherent:} \quad I_{im}(x_i, y_i) = |\tilde{h}(x_i, y_i)|^2 + |\tilde{h}(x_i - x_r, y_i)|^2 \tag{3.21}$$

On the other hand if the two sources are mutually coherent, the overall image irradiance is given by the square modulus of the sum of the amplitude responses of the individual sources. If the phase difference between the two sources is Φ then the irradiance may be expressed as:

$$\begin{aligned}
I_{im}(x_i, y_i) &= |\tilde{h}(x_i, y_i) + e^{j\Phi} \tilde{h}(x_i - x_r, y_i)|^2 \\
\text{coherent:} \quad &= |\tilde{h}(x_i, y_i)|^2 + |\tilde{h}(x_i - x_r, y_i)|^2 \\
&\quad + e^{-j\Phi} \tilde{h}(x_i, y_i) \tilde{h}^*(x_i - x_r, y_i) + e^{j\Phi} \tilde{h}^*(x_i, y_i) \tilde{h}(x_i - x_r, y_i)
\end{aligned} \tag{3.22}$$

Notice that this is the incoherent result of equation (3.21) with additional interference terms. It is these interference terms which create the difference in images formed from

coherent and incoherent targets and the difference between the images of a laser illuminated pinhole and the desired incoherent intensity point spread function.

Reynolds *et al.*, depict the difference between the coherent and incoherent illumination of a slit object in the book, *The New Physical Optics Notebook: Tutorials in Fourier Optics*, which is reprinted in Figure 3.11. The theoretical intensity distribution of the coherent and incoherent images of a slit is shown in (a), notice the coherent illumination fringes caused by the interference terms of equation (3.22).

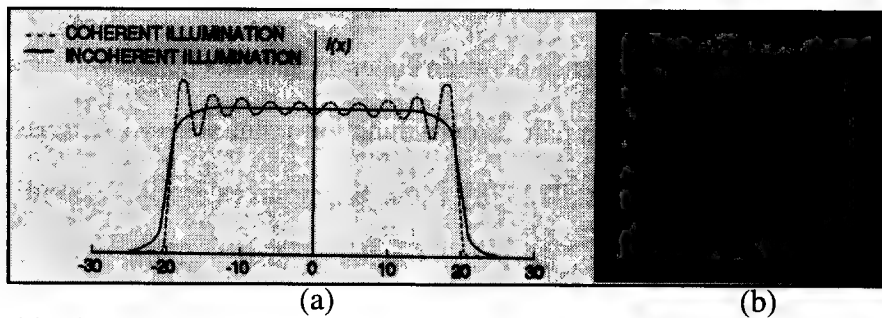


Figure 3.11: (a) The theoretical intensity distribution in the coherent and incoherent images of a slit. (b) the recorded image of a coherent slit. (reprinted from Reynolds 1989, page 115)

For this dissertation, the image distribution from a coherently illuminated $5\mu\text{m}$ diameter pinhole is detected, which is a circularly symmetric version of the slit. The diffraction limited intensity distribution in the coherent and incoherent images of various pinholes was calculated using the diffraction limited coherent and incoherent impulse responses from Figure 3.12.

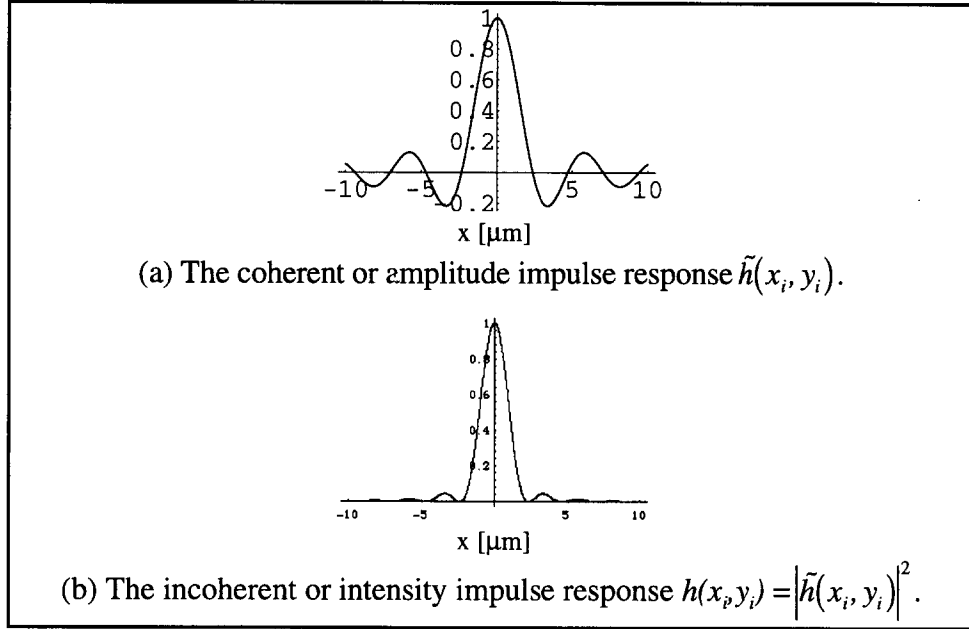


Figure 3.12: The diffraction limited impulse response for (a) coherent and (b) incoherent illumination.

Figure 3.13 shows cross-sections of various magnified pinholes in the left column ($M_T = -1$), alongside the resulting diffraction limited intensity distributions from coherent and incoherent illumination plotted together in the right column. Notice that for a large $160\mu\text{m}$ pinhole, Figure 3.13(a), the distribution resembles the slit image of Figure 3.11(a). The incoherent image (thin line) is a smoothed, slightly expanded version of the pinhole's rectangle function, whereas the coherent image (bold line) has additional ringing about the incoherent distribution due to the interference terms of equation (3.22). For smaller pinholes such as the $20\mu\text{m}$ in (d), the image distribution looks less like the slit image and more like the incoherent intensity impulse response. For the $5\mu\text{m}$ pinhole used in the experimental psf measurement shown in (e), the intensity distribution matches the intensity

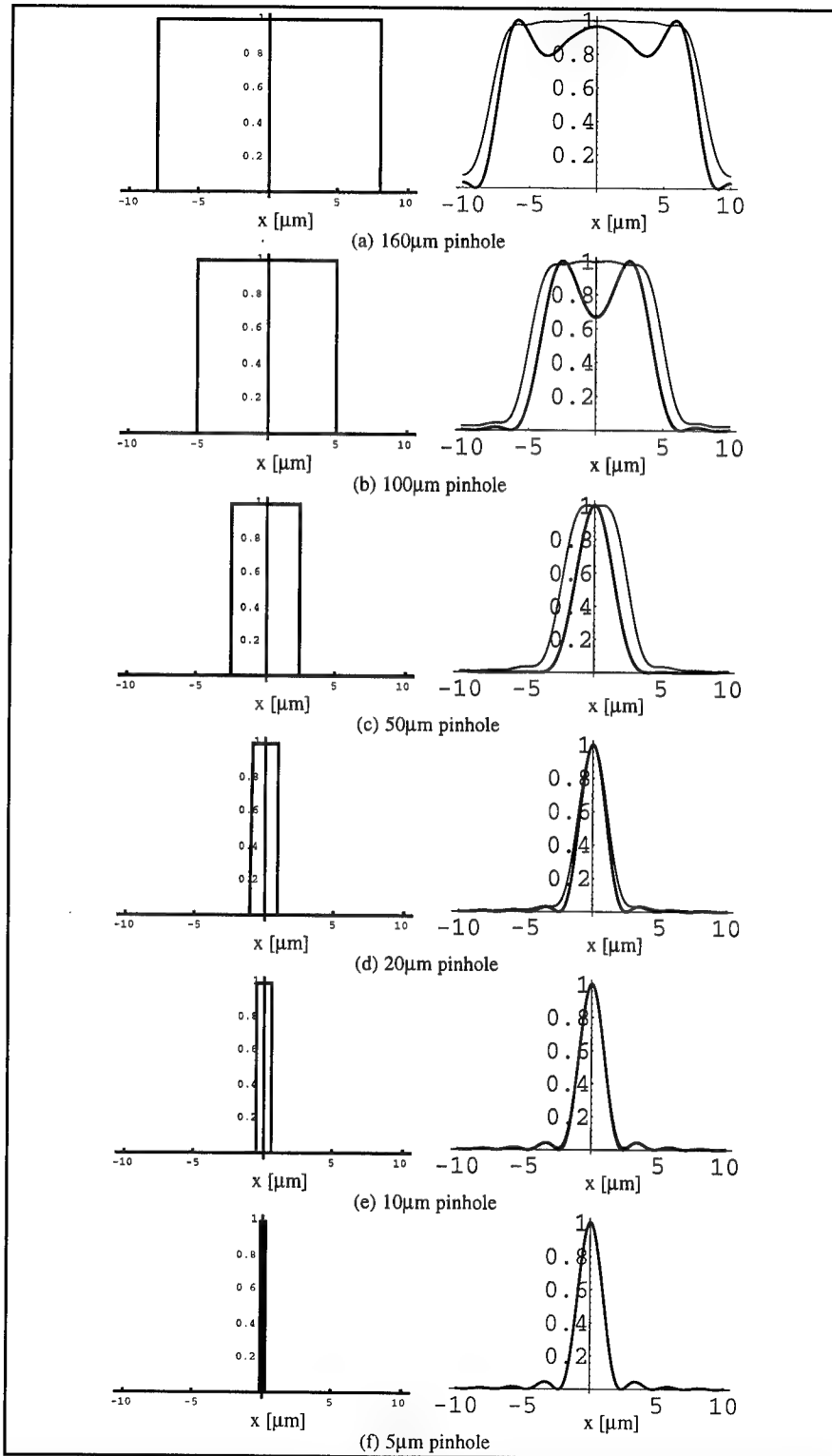


Figure 3.13: Cross-sections of various magnified pinholes, $M_T = -1$, (left column), alongside the resulting diffraction limited intensity distributions from coherent (bold line) and incoherent (thin line) illumination plotted together (right column).

impulse response and the difference between the coherent and incoherent illumination is negligible.

Another experimental consideration is that the detector pixels are $10\mu\text{m}$ wide. This creates a scenario where all of the distributions of Figure 3.13 are unresolved. The diffraction limited images of pinholes smaller than $100\mu\text{m}$ fall entirely within the boundaries of one pixel. Therefore, the interference effects of the coherent source aren't resolved and the coherent illumination can accurately simulate incoherent illumination.

3.4.2.2 Experimentally measured results

A set of images of the coherent illuminated $5\mu\text{m}$ pinhole taken at different levels of defocus is shown in Figure 3.14. For this data set the CCD was stepped along the optical axis with a step size of $dz=0.125\text{ mm}$. This series shows the effect of aberrations on the incoherent point spread function. The predominate aberration is spherical, visualized as lack of symmetry about best focus. The spherical aberration caustic creates a hard ring of intensity on the marginal side of focus and a softer, more evenly distributed blurring on the paraxial side of focus. Theoretically the coherent source will cause interference fringes on top of the aberrated intensity distributions, however again they are unresolved by the $10\mu\text{m}$ pixels and average to an appropriate representation of the incoherent intensity impulse response.

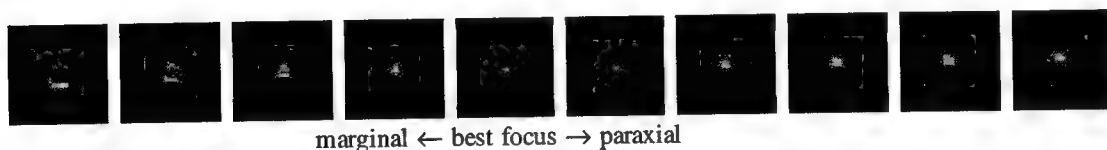


Figure 3.14: Series of images (32×32 pixels) of a $5\mu\text{m}$ pinhole illuminated by a HeNe laser recorded with DOIS through focus.

A measured 3D incoherent intensity point spread function was assembled from stacking 32×32 pixel images of a pinhole illuminated with a 542nm HeNe laser at 32 stages of defocus. The incremental step size was $dz=0.125\text{mm}$, corresponding to a

wavelength step size $d\lambda=0.25\text{nm}$. A cross-section of the psf cube, $h(r,z)$, is plotted in Figure 3.15 as (a) a density plot and (b) a three-dimensional plot. The 3D distribution is circularly symmetric about the $r=0$ optical axis.

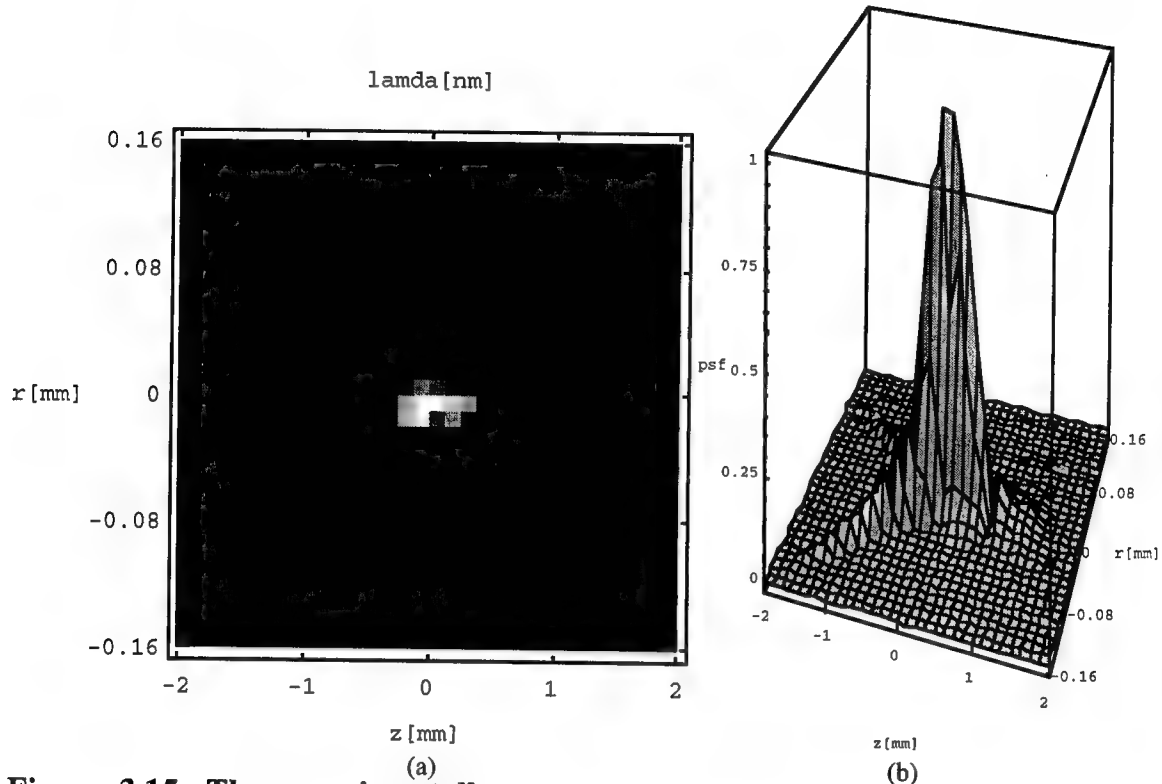


Figure 3.15: The experimentally measured intensity point spread function, $h(r,z)$, (a) a density plot (b) a 3D plot.

The measured spectral intensity point spread function, $h(z(\lambda))=h(0,u)$, is plotted in Figure 3.16 with the theoretical $h(z(\lambda))$ determined from both geometric and diffraction limited theory. The z axis labels include the spectral conversion. The full width at half max (FWHM) represents the spectral bandwidth of DOIS. The FWHM diffraction limited bandwidth is $\Delta\lambda=0.06\text{nm}$ and the measured spectral bandwidth is $\Delta\lambda=1.5\text{nm}$, both determined at $\lambda=542\text{nm}$. See Chapter 5 for more on the experimental characterization of DOIS.

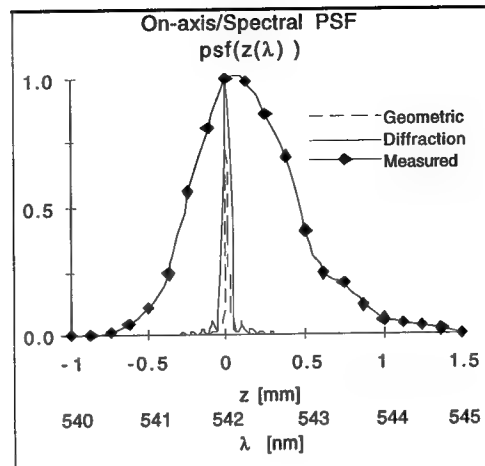


Figure 3.16: The theoretical and measured on-axis/spectral intensity psf, $h(z(\lambda))=h(0,u)$.

The three-dimensional intensity psf of Figure 3.15 can be Fourier transformed to yield the three-dimensional optical transfer function (OTF) shown in Figure 3.17. The OTF is required for several of the digital image restoration techniques in Chapter 8. It is important to note that there is a significant difference in the behavior of the experimental and theoretical OTFs. Thus it is extremely important to use the experimental OTF wherever possible. As there is probably less difference between similar DOE lenses than there is between experimental and theoretical functions, it is reasonable to simply interpolate from experimental curves to correct for changes in the design parameters.

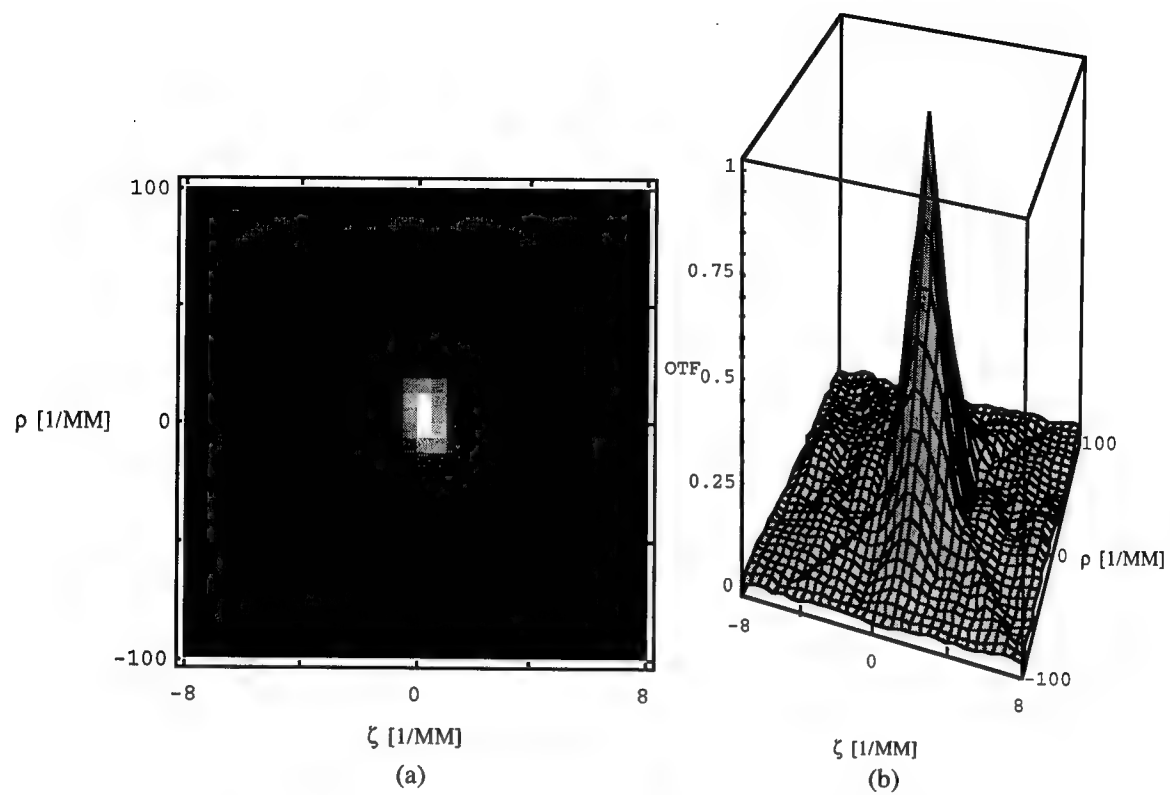


Figure 3.17: The experimentally measured $OTF(\rho, \zeta)$, (a) a density plot (b) a 3D plot.

4. THREE DIMENSIONAL IMAGE FORMATION WITH A DIFFRACTIVE OPTICAL ELEMENT (DOE)

The Diffractive Optic Image Spectrometer (DOIS) approach to image spectrometry has been broken into the series of coordinate transformations and operators that are depicted in the flow chart of Figure 4.1, [Sitter 1990, Frieden 1967, Barrett 1981] The top box represents imaging with the diffractive optical element (DOE) in DOIS and is described in section 4.1. The DOE performs two operations, Gaussian imaging with a *Spectral Gaussian Coordinate Transform* and image degradation characterized by *Three-dimensional Shift Variant Transfer Theory*. The image space is then sampled by the CCD camera.

The acronyms used below include coordinate transform (CT), shift variant (SV) and shift invariant (SIV).

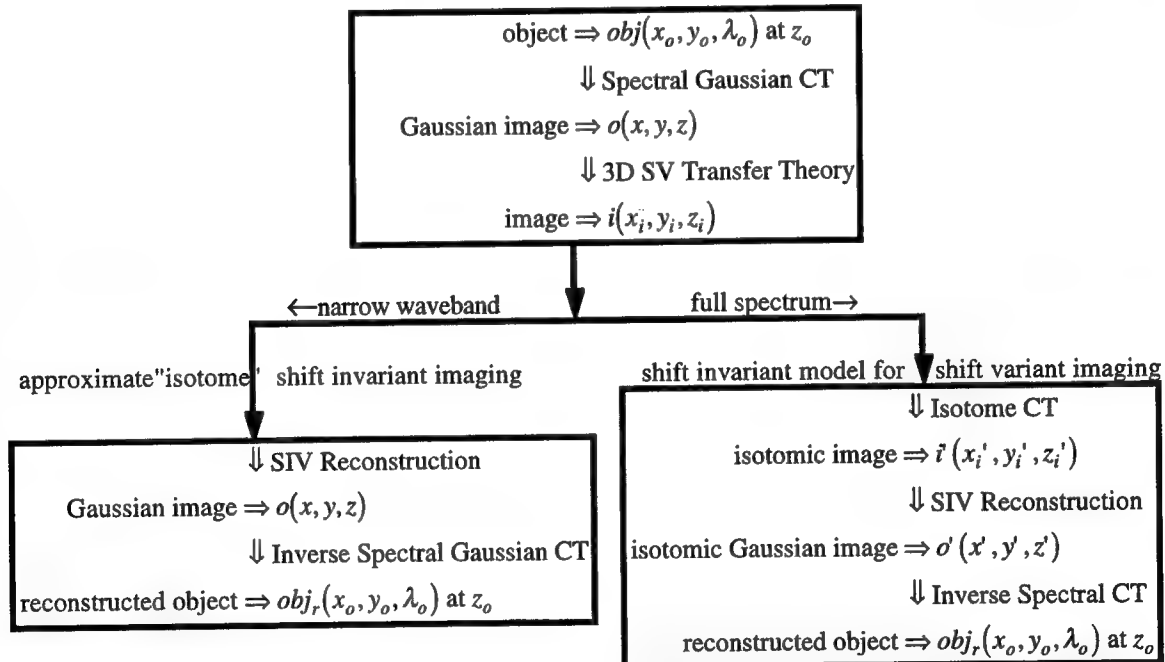


Figure 4.1: A flow chart depicting the manipulation of the three-dimensional object cube as it is imaged, and reconstructed.

Image processing can be applied to reconstruct the object under one of two conditions, shown as two possible paths. Selection of a path will depend on the extent of

the waveband desired. The left path can be taken within a narrowband image volume called an isotome and is discussed in section 4.2. In an isotome the point spread function (psf) is approximately unchanging and is considered shift invariant for modeling and reconstruction algorithms. It will be shown in section 4.2.2 that achievable isotomes have a bandwidth up to 20nm in the visible range prototype built for this dissertation.

When the spectra of interest includes the entire visible range it is necessary to perform the coordinate transform (CT) shown in the right path of Figure 4.1 and discussed in section 4.3. The CT converts the image space with a shift variant (SV) psf into an alternate coordinate system with a shift invariant (SIV) psf. The coordinate transform designed for this system is called the *Isotome Coordinate Transform*. Once applied, reconstruction algorithms using linear SIV filtering techniques can be applied to obtain an isotomic Gaussian image. The final step is to again transform the data. This time an *Inverse Spectral Coordinate Transform* is used to reconstruct the object.

4.1 Imaging with a Diffractive Optic

Although one normally thinks of a diffractive optical element (DOE) as a monochromatic imaging device, they can be used to image polychromatic sources. Sweatt has shown a mathematical equivalence between a diffractive optical element and an ultra high index lens [Sweatt 1979]. The DOE performs as a lens with severe chromatic aberration. It is this aberration which provides the dispersion for DOIS.

It is important to remember that all imaging systems are imperfect, introducing aberrations which distort the image. Although high-quality, diffractive/refractive optical kinoforms can be designed to minimize image distortion and aberrations such as spherical and coma [Stone 1988], the DOIS spectral sectioning technique is plagued with defocus from the chromatic aberration. This results in errors in the recorded spectral slices which have to be corrected with post-detection image processing.

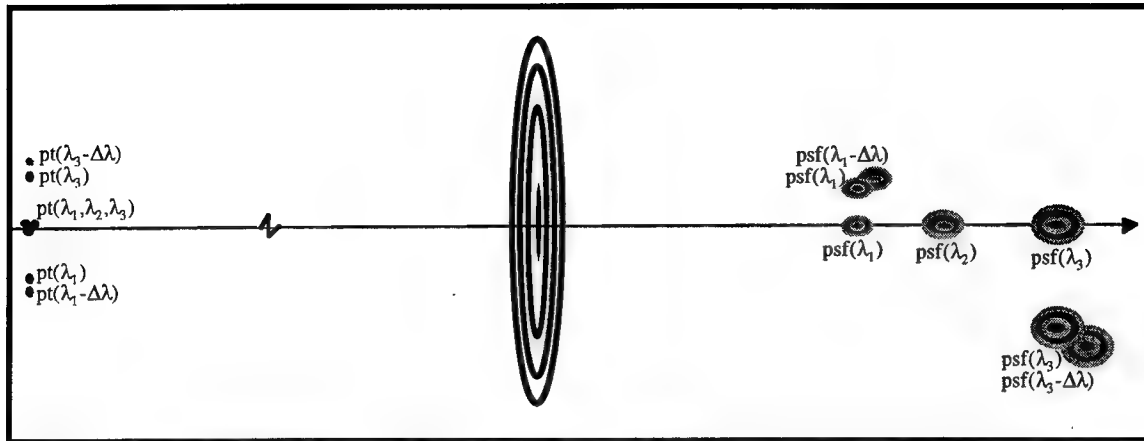


Figure 4.2: A diffractive optical element imaging various spectral point sources.

A good place to start this discussion is to consider imaging a point source. Figure 4.2 shows a DOE imaging point sources of various wavelengths. Notice that the DOE does several things. The spectra is spread out along the optical axis and the magnification is different in each focal plane. These functions are described by Gaussian imaging. Additionally, the images of the point sources are not perfect delta functions. Each is a spheroidal intensity distribution around the "ideal" Gaussian image point. This blurring is described by three-dimensional transfer theory. The spheroid intensity distributions represent the three-dimensional point spread functions of the DOE, and cause both spatial (transverse) and spectral (longitudinal) blurring.

4.1.1 Spectral Gaussian Coordinate Transform

The imaging can be represented by a coordinate transform, performing both a scaling function and transforming the spectral data into a spatial coordinate, z . Starting with the imaging equation:

$$\frac{1}{f_o} = \frac{1}{z_o} + \frac{1}{z} \quad (4.1)$$

where f_o is the focal length at λ_o , z_o is the object distance and z is the Gaussian image distance. Introducing the diffractive optic spectral response [Swanson 1989]:

$$f_o \lambda_o = f_d \lambda_d = D$$

$$f_o = \frac{f_d \lambda_d}{\lambda_o} = \frac{D}{\lambda_o} \quad (4.2)$$

D is the DOE design constant where f_d is the design focal length at the design wavelength, λ_d . Substituting (4.2) into (4.1) results in the diffractive optic imaging equations:

$$\frac{\lambda_o}{D} = \frac{1}{z_o} + \frac{1}{z} \quad (4.3)$$

$$\lambda_o = D \left(\frac{z + z_o}{z_o z} \right) \Leftrightarrow z = \left(\frac{D}{\lambda_o z_o - D} \right) z_o \quad (4.4)$$

The conversion between spectra and image distance, z , at a fixed object distance, z_o , is described by equation (4.4).

The transverse and longitudinal magnification, M_T and M_L , are:

$$M_T = -\frac{z}{z_o} = -\frac{D}{\lambda_o z_o - D} \quad \text{and} \quad M_L = -\left(\frac{z}{z_o} \right)^2 = -M_T^2 \quad (4.5)$$

Notice that the magnification is dependent on the design constant, D , and the fixed object distance, z_o , leaving wavelength, λ_o , as the only variable.

The DOE transforms the object $obj_r(x_o, y_o, \lambda_o)$ at z_o , into a Gaussian image, $o(x, y, z)$, with the following *Spectral Gaussian Coordinate Transform*:

$$o(x, y, z) = obj(M_T x_o, M_T y_o, -M_T z_o) \quad (4.6)$$

$$o(x, y, z) = obj\left(\left(\frac{-D}{\lambda_o z_o - D}\right) x_o, \left(\frac{-D}{\lambda_o z_o - D}\right) y_o, \left(\frac{D}{\lambda_o z_o - D}\right) z_o\right) \quad (4.7)$$

4.1.2 Three-dimensional Transfer Theory

As previously mentioned, the actual image of a point source formed by a DOE is a blurred version of the Gaussian point, seen in Figure 4.2. The blurring is represented by *Three-dimensional Transfer Theory*, based upon the assumptions of (1) superposition and (2) stationarity. It is well known that these conditions are met in two-dimensions by an object which radiates incoherently from an "isoplanatic" area of an object plane. These conditions can be extended to three-dimensional imaging within "isotomic" volumes of the object space [Frieden 1967]. Frieden's theory is extended below to describe the DOIS three-dimensional spectral/spatial system.

The theory of superposition implies that since the object is assumed to be incoherent, the intensities from different elements of the object, $o(x, y, z)$, are additive. The total intensity in the image, $i(x_i, y_i, z_i)$, is given by:

$$i(x_i, y_i, z_i) = \int_{-\infty}^{\infty} \int_{-\infty}^{\infty} \int_{-\infty}^{\infty} h(x, y, z; x_i, y_i, z_i) o(x, y, z) dx dy dz \quad (4.8)$$

where $h(x, y, z; x_i, y_i, z_i)$ is the space variant incoherent impulse response or psf. This impulse response physically represents the intensity distribution in image space from the illumination by a monochromatic point source in object space. It is particularly important for estimating the image degradation caused by surrounding coordinates. The three-dimensional psf predicts cross-talk and blurring from coordinates both within the same spectral image and from surrounding spectra.

Classical two-dimensional transfer theory defines an "isoplanatic" plane where the psf is slowly varying and approximately *stationary*. For DOIS an "isotomic" volume of the object or Gaussian image space, called an isotome, can be defined where the three-dimensional psf is dependent on the displacement from the Gaussian point and not the location of the Gaussian point itself, described by equation (4.9).

$$h(x, y, z; x_i, y_i, z_i) = h(x_i - x, y_i - y, z_i - z) \quad (4.9)$$

Physically, this requires that the psf must remain invariant under changes in position of the Gaussian point. This will be true if each point within an isotome has essentially the same wave aberrations and magnification.

Image space can be broken into several isotomic volumes, V . Each isotome, which represents a narrow waveband, can be treated by linear shift invariant filtering theory. If a particular spectral image or a narrowband spectral curve is needed, the detection and processing can be confined to an isotome following the left path of Figure 4.1.

4.2 Isotomic Imaging in a narrow waveband

Substituting equation (4.9) into (4.8), the way in which an arbitrary incoherent spectral image is distorted can be predicted from the resulting intensity convolution equation. It describes the convolution of the Gaussian image with the incoherent psf in an isotome.

$$i(x_i, y_i, z_i) = \int_{-\infty}^{\infty} \int_{-\infty}^{\infty} \int_{-\infty}^{\infty} h(x_i - x, y_i - y, z_i - z) o(x, y, z) dx dy dz \quad (4.10)$$

in short hand notation:

$$i(x_i, y_i, z_i) = h(x, y, z) * * * o(x, y, z) \quad (4.11)$$

Applying the Fourier Integrals:

$$\begin{aligned} O(\xi, \psi, \zeta) &= \int_{-\infty}^{\infty} \int_{-\infty}^{\infty} \int_{-\infty}^{\infty} o(x, y, z) e^{2\pi i(\xi x + \psi y + \zeta z)} dx dy dz \\ I(\xi, \psi, \zeta) &= \int_{-\infty}^{\infty} \int_{-\infty}^{\infty} \int_{-\infty}^{\infty} i(x_i, y_i, z_i) e^{2\pi i(\xi x_i + \psi y_i + \zeta z_i)} dx_i dy_i dz_i \\ H(\xi, \psi, \zeta) &= \int_{-\infty}^{\infty} \int_{-\infty}^{\infty} \int_{-\infty}^{\infty} h(x, y, z) e^{2\pi i(\xi x + \psi y + \zeta z)} dx dy dz \end{aligned} \quad (4.12)$$

The Fourier transform of the psf, $H(\xi, \psi, \zeta)$, is called the optical transfer function (OTF), or in three-dimensional microscopy texts, the contrast transfer function (CTF).

$$I(\xi, \psi, \zeta) = H(\xi, \psi, \zeta)O(\xi, \psi, \zeta) \quad (4.13)$$

Here capitals are used to refer to the Fourier transforms and the convolution is now simplified to a multiplication. In matrix form, dropping the variables:

$$\mathbf{I} = \mathbf{H}\mathbf{O} \quad (4.14)$$

If the isotome object and psf are known, the image can be modeled with equation (4.14), finishing with:

$$\begin{aligned} \mathbf{i} &= \text{InverseFourier}\{\mathbf{I}\} \\ i(x_i, y_i, z_i) &= \text{InverseFourier}\{I(\xi, \psi, \zeta)\} \end{aligned} \quad (4.15)$$

This will simulate the image without the errors and noise introduced by detection.

4.2.1 Reconstruction

Within the isotome, if the recorded spectral images, $i(x_i, y_i, z_i)$, the object distance, z_o , and the OTF are known, an *Inverse Shift Invariant Filter* and *Inverse Spectral Gaussian Coordinate Transform* can be applied to reconstruct the object, $obj_r(x_o, y_o, \lambda_o)$ at z_o . The above transfer theory can be applied in reverse using:

$$\mathbf{O} = \mathbf{H}^{-1}\mathbf{I} \quad (4.16)$$

$$\begin{aligned} \mathbf{o} &= \text{InverseFourier}\{\mathbf{O}\} \\ o(x, y, z) &= \text{InverseFourier}\{O(\xi, \psi, \zeta)\} \end{aligned} \quad (4.17)$$

where $\mathbf{I}=I(\xi, \psi, \zeta)$ is the Fourier transform of the image, $i(x_i, y_i, z_i)$, and \mathbf{H}^{-1} is the inverse of the OTF matrix which when applied as an inverse filter performs the required deconvolution.

To convert $o(x, y, z)$ into a reconstructed spectral/spatial object, $obj_r(x_o, y_o, \lambda_o)$ at z_o , the following *Inverse Spectral Gaussian Coordinate Transform* has been derived.

$$\text{at } z_o \quad obj_r(x_o, y_o, \lambda_o) = o\left(\frac{x}{M_T}, \frac{y}{M_T}, D\left(\frac{1}{z} + \frac{1}{z_o}\right)\right) \quad (4.18)$$

$$obj_r(x_o, y_o, \lambda_o) = o\left(-\frac{z_o}{z}x, -\frac{z_o}{z}y, D\left(\frac{z_o + z}{zz_o}\right)\right) \quad (4.19)$$

4.2.2 Define isotome bandwidth

To determine which path of Figure 4.1 should be taken, it must be determined if the image cube, or bandwidth of the image cube, can be modeled as a shift invariant isotome. To define an isotome the invariance on h must be quantified [Frieden 1967]. Refer to section 3.4.1 for the theoretical description of the incoherent point spread function h . The invariance over the isotome can be measured by the invariance of $h(u, o)$ and $h(0, v)$ under changes Δz or $\Delta \lambda$. This can be quantified by the differential radial distance $\Delta r = R_v$ to the first zero of $h(v, 0)$ in equation (3.13), and the axial distance $\Delta z = Z_u$ to the first zero of $h(0, u)$ in equation (3.14):

$$\Delta r = R_v = \pm 1.22 \lambda \left(\frac{f}{2a}\right) \text{ or } = \pm \frac{1.22 z_i \lambda}{2a} \quad (4.20)$$

$$\Delta z = Z_u = \pm 8 \lambda \left(\frac{f}{2a}\right)^2 \text{ or } = \pm \frac{2 z_i D}{a^2} \quad (4.21)$$

recall that D is the design constant $f_d \lambda_d$. The differentials ΔR_v and ΔZ_u measure the variance:

$$\frac{\Delta R_v}{R_v} = \frac{\Delta z_i \lambda}{z_i \lambda} \quad (4.22)$$

$$\frac{\Delta Z_u}{Z_u} = \frac{\Delta z_i}{z_i} = \frac{\Delta M}{M} \quad (4.23)$$

In practice, Frieden defines an isotome as a region where the magnification changes less than 10% ($\Delta M_L / M_L \leq 10\%$). Therefore, over small spectral regions or small amounts of axial translation the image space can be considered isotomatic and SIV linear filtering algorithms will hold. Using the differentials in equation (4.22) and (4.23), which are plotted in Figure 4.3, see that for a target at an image distance of $z_o > 10f$ and a bandwidth, $\Delta\lambda/\lambda$, up to 5%, that the variance $\Delta R/R \leq 1\%$ and $\Delta Z/Z \leq 6\%$. This indicates that the conditions for an isotome hold within a spectral region up to a 20nm bandwidth.

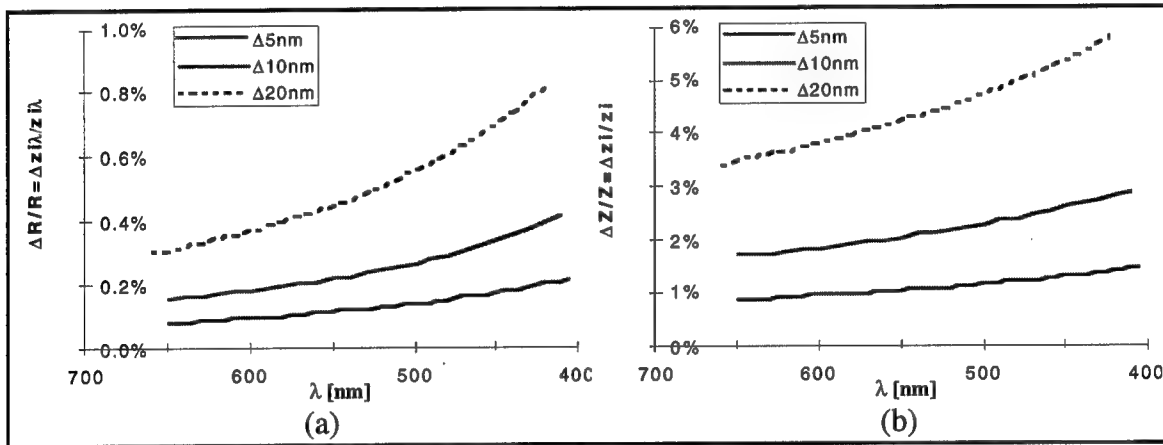


Figure 4.3: The variance on (a) R_v , and (b) Z_u , at $z_o = 10f_o$.

4.3 Full Spectrum Imaging

The technique of section 4.2 can be applied to individual isotomes to model and reconstruct data from a narrowband source. However, when the spectra of interest includes the entire visible range, it is necessary to perform the coordinate transform shown in the right path of Figure 4.1, which creates a *shift invariant model for shift variant imaging*.

Barrett and Sitter introduced a technique to model the shift variant blurring on three-dimensional images [Barrett 1981, Sitter 1990]. The model consists of a coordinate transformation of the object followed by a shift invariant blur operation, which is in turn

followed by a second coordinate transformation of the image. This technique can be rederived to apply to the reconstruction of the object when the image space is shift variant.

Recall from equation (4.8), if an imaging system is not isotometric, it is modeled by the shift variant integral of the form:

$$i(x_i, y_i, z_i) = \int_{-\infty}^{\infty} \int_{-\infty}^{\infty} \int_{-\infty}^{\infty} h(x, y, z; x_i, y_i, z_i) o(x, y, z) dx dy dz$$

where $i(x_i, y_i, z_i)$ represents the image space distribution, $o(x, y, z)$ is the Gaussian object distribution and $h(x, y, z; x_i, y_i, z_i)$ is the space variant incoherent psf. Sitter showed that for incoherent imaging systems, there exist coordinate transformations from object space and image space to an intermediate space (which will be denoted by primed quantities) where the integral of equation (4.8) can be expressed as a convolution. That is, there exists a coordinate transformation from $i(x_i, y_i, z_i)$ to $i'(x'_i, y'_i, z'_i)$ and from $o(x, y, z)$ to $o'(x', y', z')$ so that:

$$i'(x'_i, y'_i, z'_i) = \int_{-\infty}^{\infty} \int_{-\infty}^{\infty} \int_{-\infty}^{\infty} h'(x', y', z'; x'_i, y'_i, z'_i) o'(x', y', z') dx' dy' dz' \quad (4.24)$$

where:
$$h'(x', y', z'; x'_i, y'_i, z'_i) = h'(x'_i - x', y'_i - y', z'_i - z') \quad (4.25)$$

resulting in:

$$i'(x'_i, y'_i, z'_i) = \int_{-\infty}^{\infty} \int_{-\infty}^{\infty} \int_{-\infty}^{\infty} h'(x'_i - x', y'_i - y', z'_i - z') o'(x', y', z') dx' dy' dz' \quad (4.26)$$

where $i'(x'_i, y'_i, z'_i)$ and $o'(x', y', z')$ are the coordinate transformed irradiance distributions and h' is the incoherent psf in the transformed space.

4.3.1 Isotome Coordinate Transform

A coordinate transform was derived for the DOE to transform the shift variant image space i to the shift invariant isotome i' with the assumption that aberrations are

minimized and that magnification is the major cause of the space variance. The *isotome coordinate transform* applies an inverse magnification transforming a polygon shaped space with variable magnification into a unit magnification space pictured in Figure 4.4.

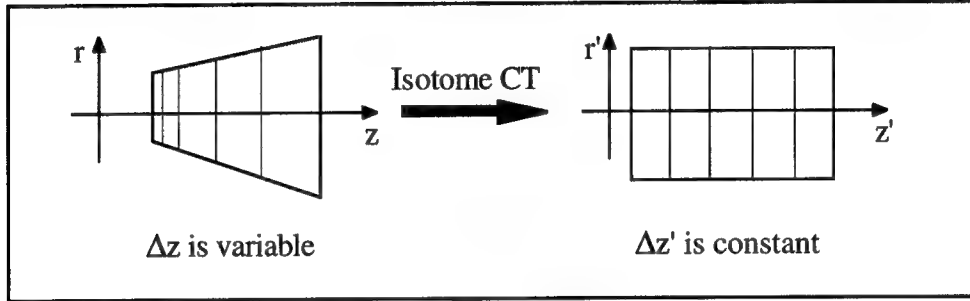


Figure 4.4: Visual representation of the *isotome coordinate transform* forming an image space with unit magnification

In order to remove the variable magnification which is a function of $z_i(\lambda)$, the following coordinate transform is used:

$$M_T = -\frac{z_i}{z_o} \quad M_L = -\left(\frac{z_i}{z_o}\right)^2 = -M_T^2 \quad (4.27)$$

$$\begin{aligned} i'(x'_i, y'_i, z'_i) &= i\left(\frac{x_i}{M_T}, \frac{y_i}{M_T}, \frac{z_i}{M_L}\right) \\ &= i\left(\frac{-z_o}{z_i} x_i, \frac{-z_o}{z_i} y_i, -\left(\frac{-z_o}{z_i}\right)^2 z_i\right) \end{aligned} \quad (4.28)$$

$$\begin{aligned} h'(x', y', z') &= i\left(\frac{x}{M_T}, \frac{y}{M_T}, \frac{z}{M_L}\right) \\ &= i\left(\frac{-z_o}{z_i} x, \frac{-z_o}{z_i} y, -\left(\frac{-z_o}{z_i}\right)^2 z\right) \end{aligned} \quad (4.29)$$

Equations 4.28 and 4.29 completely reverse the magnification of the Gaussian imaging. However in some applications it may be practical to transform the image cube to a intermediate magnification, such as to match the magnification of the measured image cube to the magnification of a measured point spread function.

4.3.2 Reconstruction

Now that the image space is essentially all one isotome, the entire full spectrum object cube can be reconstructed with the inverse transfer reconstruction that was used in section 4.2.1, substituting the primed variables:

$$i'(x_i', y_i', z_i') = h'(x', y', z') *** o'(x', y', z') \quad (4.30)$$

$$I(\xi, \psi, \zeta) = H(\xi, \psi, \zeta) O(\xi, \psi, \zeta) \quad (4.31)$$

$$\mathbf{O}' = \mathbf{H}'^{-1} \mathbf{I}' \quad (4.32)$$

$$\mathbf{o}' = \text{InverseFourier}\{\mathbf{O}'\}$$

$$o'(x', y', z') = \text{InverseFourier}\{O(\xi, \psi, \zeta)\} \quad (4.33)$$

4.3.3 Inverse Spectral Coordinate Transform

The magnification from the x_i and y_i coordinates was removed in the coordinate transform of equation (4.28). The final coordinate transform reconstructs the spectral information λ_o from z_i' , using equation (4.4).

$$\text{at } z_o \quad obj_r(x_o, y_o, \lambda_o) = o' \left(x', y', \frac{D}{z_o} \left(\frac{z_i'}{z_o} + 1 \right) \right) \quad (4.34)$$

5. PROTOTYPE CHARACTERIZATION

5.1 DOIS Prototype

A prototype of the DOIS described in Chapter 2 was assembled and characterized at Rome Laboratory's Photonics Center. Figure 5.1 is a photo of the DOIS prototype. The DOE is on the right and connected to the CCD camera with a tubular baffle. Although a system designed for field use would include electronic control translation stages, the laboratory prototype is manually controlled. The DOE is mounted on an Oriel rail carrier which slides on a 60 cm Oriel rail marked with a metric scale for location measurement.

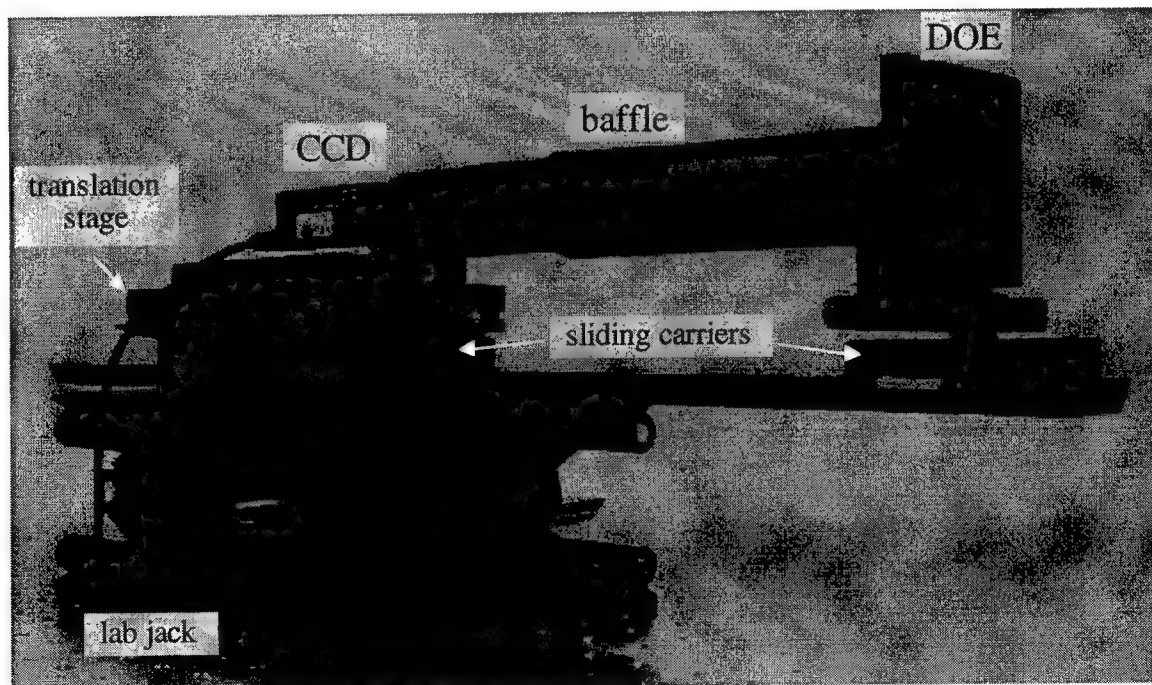


Figure 5.1: Photo of the DOIS prototype.

The camera is first secured to a micropositioning translation stage for fine control, then on another rail carrier. Each carrier is marked with a graduated rule for positioning on the rail within 1 mm, and the micropositioning vernier on the detector is accurate to .001 inches (25.7 μm). Manual translation of the camera or DOE is possible. With a target at infinity, the lens would be moved without adversely impacting the object distance s_o and

the detector to DOE distance $s_{i\lambda}$ for each wavelength would be the spectral focal distance, $s_{i\lambda} = f_{\lambda}$. However, for target distances restrained by the dimensions of the laboratory, the best results are obtained by keeping the DOE stationary and moving the detector. The detector carrier is stepped with coarse increments, $dz = 1 \text{ mm}$, corresponding to spectral step size $d\lambda$ ranging from 1nm to 3nm, at 400nm and 650nm respectively. For finer spectral measurements, the detector carrier was placed at a set position and the micropositioning vernier was tuned with $dz = .005''$, corresponding to a $d\lambda$ of .1nm to .4nm depending on the wavelength region.

5.2 The Diffractive Optic Element

The DOE fabricated for this prototype is a single etch Fresnel Zone Phase Plate. Figure 5.2 lists the figures of merit for the DOE in DOIS. The dominant effect of only a single etch DOE is the low first order diffraction efficiency. This limits the amount of light which is properly imaged and increases the minimum detectable target radiance, but it performs sufficiently for this proof of concept, laboratory demonstration. A well designed DOIS would incorporate a high efficiency phase grating with $\eta \approx 100\%$ at the design wavelength. The DOE could be a multilevel, $N \geq 16$ photolithography phase plate, or a continuous profile grating generated by holography, diamond turning or a laserwriter as discussed in Chapter 3.

DOE type	2 level, phase etched, zone plate
Fabrication at the National Nanofabrication Facility of Cornell University	ebeam mask generation contact lithography exposure ion reactive etched
substrate	BK-7 optical flat, 3mm thick
diameter	2", 5 cm clear aperture
design focal length f_o	200 mm
design wavelength λ_o	588 nm
theoretical diffraction efficiency, η	40 % at 588 nm
experimentally measured η	27% at 670 nm laser diode 35 % at 632.8 nm HeNe 30 % at 542 nm GreNe
MTF @ $1/e$	32 lp/mm

Figure 5.2: DOE figures of Merit

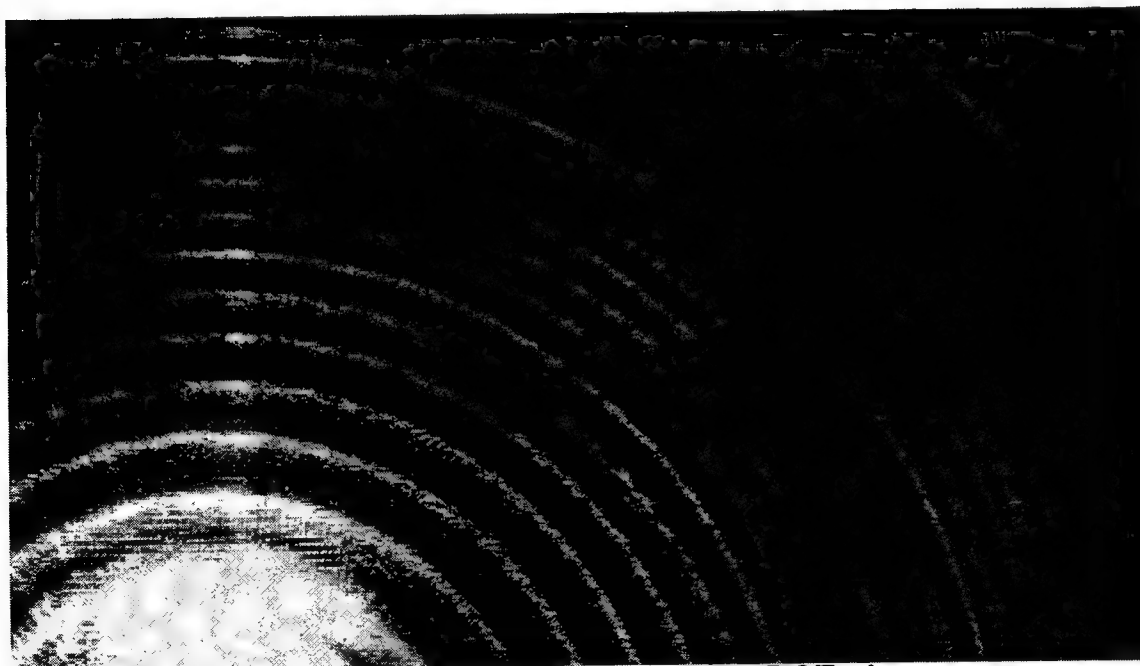


Figure 5.3: A partial image of the DOE rings.

The ring pattern of Figure 5.3 was recorded by illuminating DOIS with a high intensity HeNe beam. The first order focus is super saturated and is seen on the bottom left. The DOE's zero order diffraction efficiency is approximately 5% at 633nm. The resulting zero order beam has no optical power, passing straight through the lens. It adds background photon noise but is normally not intense enough to be detected as signal. However, when illuminated with the laser beam, the undiffracted light projects a shadow of the zone plate on the detector.

The first order diffraction efficiency is a measure of the percentage of the light collected that is imaged to the desired detector location. This figure of merit dictates the minimum target radiance that will be detected. The setup in Figure 5.4 was used to experimentally determine the DOE's diffraction efficiency. To determine the spectral dependence of the diffraction efficiency the DOE was characterized at three wavelengths. A laser diode was used which emitted at 670 nm and measurements were obtained at 632.8 nm and 542nm with two Helium Neon lasers. Figure 5.5 shows the experimental results plotted along with the theoretical spectral first order diffraction efficiency [Chapter 3].

The laser beam was directed into an integrating sphere/detector apparatus and the power was recorded, $P_{\text{total laser}}$. The DOE was then placed in the beam and the integrating sphere was aligned to collect only the first diffracted order and again the power was recorded, $P_{\text{1st order}}$. The diffraction efficiency is the ratio of these two values.

$$\eta_{1^{\text{st}} \text{ order}} = \frac{P_{1^{\text{st}} \text{ order}}}{P_{\text{total laser}}} \quad (5.1)$$

To account for the efficiency at different radii and zone spacing, η was determined with the beam hitting the DOE at half radius and repeated at almost full aperture. The two radii measurements were averaged.

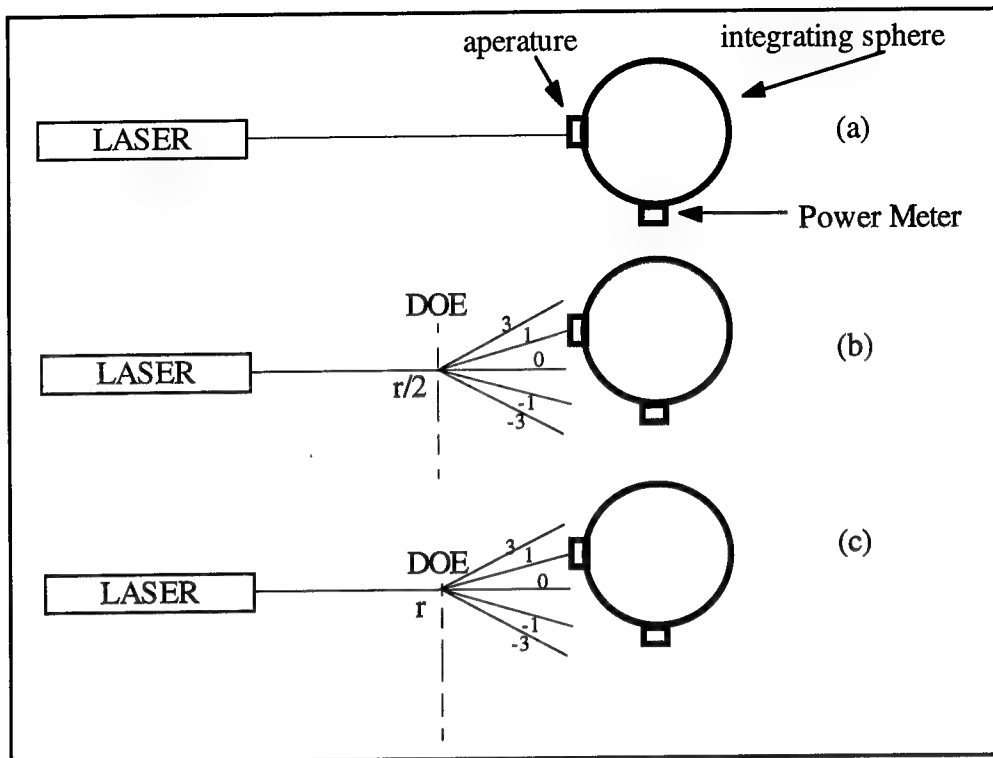


Figure 5.4: Diffraction efficiency experimental setup (a) determine the total power. (b) first order power at $r/2$. (c) first order power at full aperture.

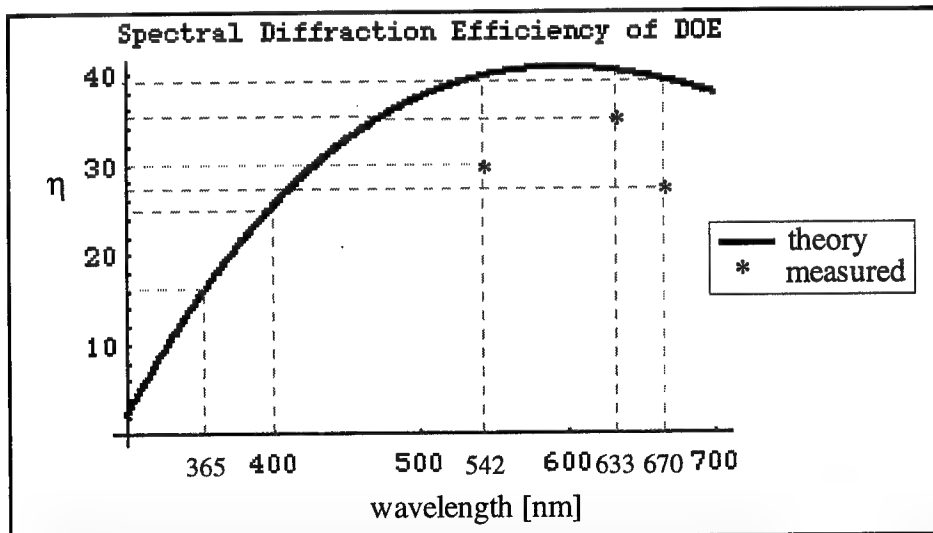


Figure 5.5: Theoretical and measured diffraction efficiency vs. wavelength.

The DOE MTF was measured at the Diffractive Optics Test Facility at Rochester Photonics Corporation, RPC. This is an automated testbed that measures the MTF of a diffractive optic using a double knife edge technique [Faklis 1993]. Figure 5.6 (a) shows the measured tangential and sagittal MTFs of the DOE at 540 nm, as well as the diffraction limited MTF. The dramatic drop from the DC term is due to the low diffraction efficiency of the DOE. The second curve (b) is the MTF normalized with the diffraction efficiency. Warren Smith, in his book on lens design [Smith 1992], gives the goal of a MTF of 50% at 50 lp/mm for high quality photographic lenses and 20% at 30 lp/mm over 90% of the field. This DOE falls well below this requirement, however Figure 5.6(c) is the measured MTF of a well designed, high efficiency DOE lens and is presented to show that this technology can greatly exceed standard design requirements. Additionally, the DOE design can be optimized using computer design codes such as ZEMAX to reduce aberrations both on and off axis. The substrate surface curvatures are used for minimizing aberrations by producing a kinoform, which adds a low power refractive surface for balancing aberrations such as spherical and coma.

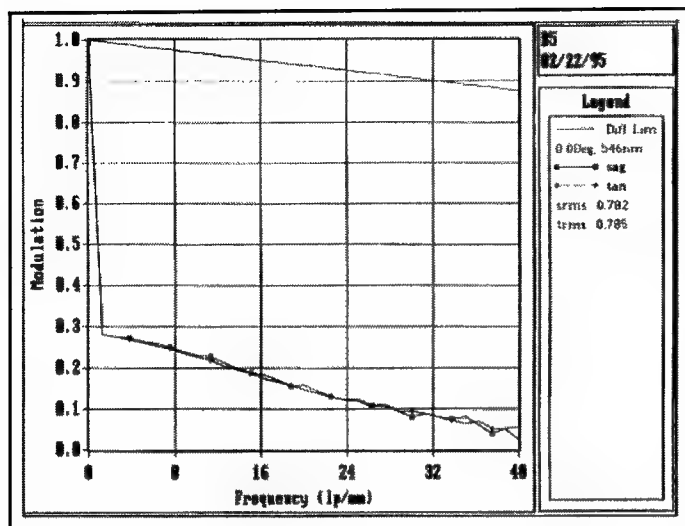
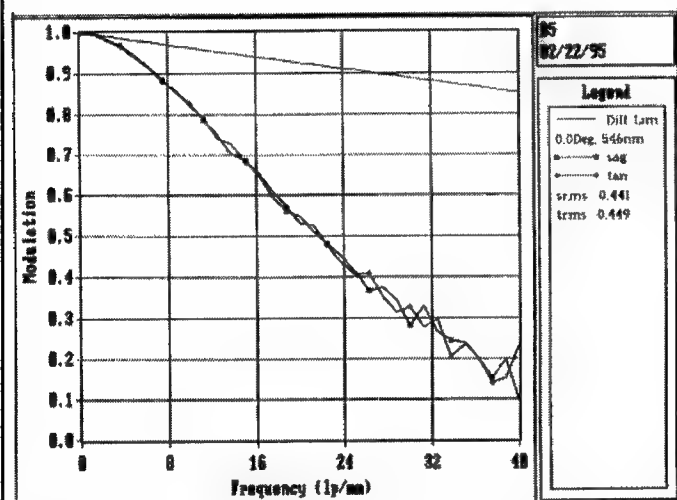
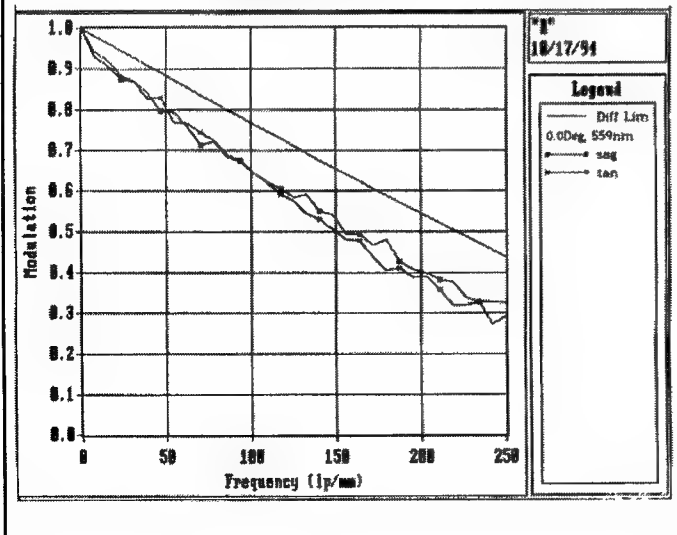


Figure 5.6: DOE MTF, measured at RPC Diffractive Optic Testing Facility.

(a) measured and diffraction limited MTF at 540 nm.



(b) Normalized 546 nm MTF, MTF/η .



(c) MTF performance of a well designed high efficiency DOE measured at 559 nm, provided as an example of the technology's capability.

5.3 The CCD camera

The CCD camera in the prototype is a SONY XC-75 whose specifications are found in Figure 5.7.

SONY CCD Monochrome Video Camera	XC-75
Pickup device	Interline-transfer CCD
effective picture elements (pixels)	768 x 494 (horizontal / vertical)
sensing area	1/2 inch
CCD drive frequency	15.7 kHz vertical 14.3 kHz horizontal
pixel size	8.4 x 9.8 μm (horizontal / vertical)
chip size	7.95 x 6.45 mm (horizontal / vertical)
scanning	525 lines, 2:1 interlace
gain settings	AGC automatic gain control F fixed or M manual
video S/N ratio	56 dB
minimum illumination	3.0 lux
sensitivity	400 lux with AGC ON

Figure 5.7: DOIS camera specifications.

The CCD camera was used without the conventional lens attachment, and the DOE was mounted ≈ 200 mm away from the camera with a homemade baffle of concentric tubes, depicted in Figure 5.1, blocking most stray photons from the room. The output of the camera was connected to a monitor, a framegrabber board and a video recorder. The images were recorded digitally, one image at a time. The computer has the capability of recording many frames consecutively, but memory constraints prevented this. The low efficiency of the DOE made it necessary to have the automatic gain control on for most of the experimental demonstrations. This is unfortunate because the capability of absolute intensity readings is lost. However, the AGC did a wonderful job of automatically adjusting to the spectral efficiency η_λ of the DOE and camera. In an improved system, the

gain will be set constant and the intensity will be corrected by dividing the spectral intensity data by the DOE spectral efficiency, η_λ , and the camera spectral response curve, measured below.

The camera spectral response was measured using a Tungsten Halogen lamp and an Oriel grating monochromator. Figure 5.8 is the relative spectral response of the CCD camera in its original packaging. This curve suggested that there was a filter on the camera, possibly to mimic the response of the human eye. After careful removal of the faceplate, a filter was found between the protective window and the CCD chip. Figure 5.9 is the spectral response of the same CCD with the unknown filter removed. The image of Chapter 2 were recorded with this filter, but the analytical demonstration in the next chapter was performed after the filter was removed.

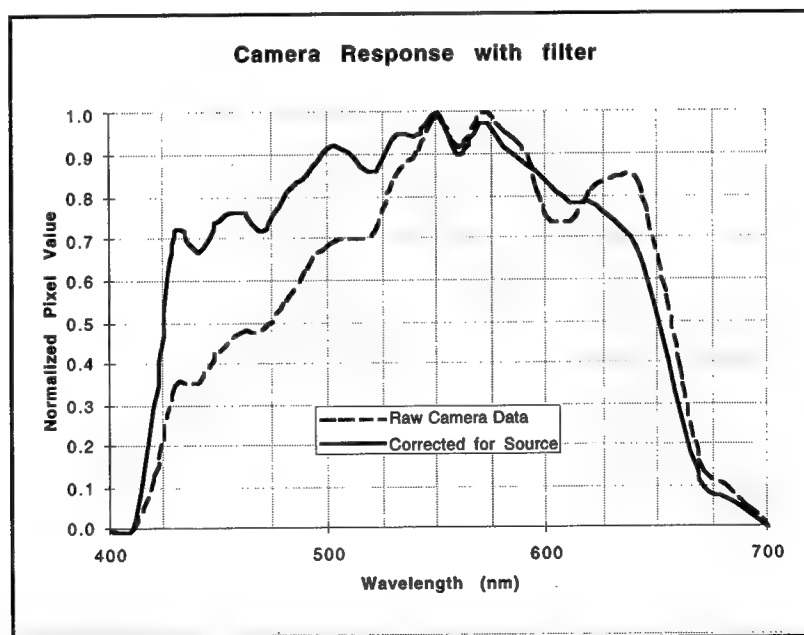


Figure 5.8: The experimentally determined spectral response curve of the SONY CCD. The dashed line is the raw data, and the solid line has the spectral curve of the lamp and monochromator grating divided out.

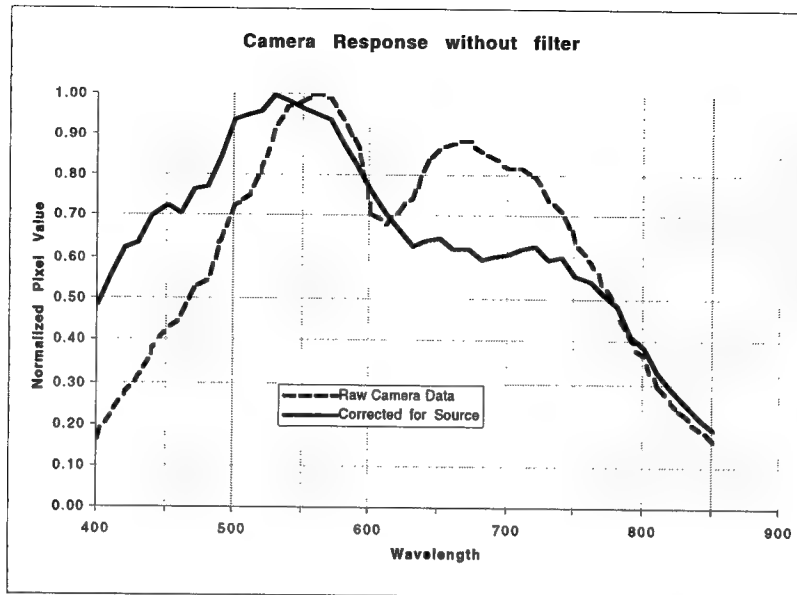


Figure 5.9: the experimentally determined spectral response curve of the SONY CCD after the removal of a factory placed filter. The dashed line is the raw data, and the solid line has the spectral curve of the lamp and monochromator grating divided out.

5.4 DOIS prototype characteristics

Since imaging is a large part of the requirements of the system, and many readers may not have seen the imaging capabilities of a simple Fresnel Zone Plate, a 256 x 256 image of the Air Force Resolution Target is included as Figure 5.10. The resolution target used was made of chrome on glass. It was illuminated with the Tungsten Halogen lamp and filtered with a 10 nm line width filter at 550 nm. The resolution target was placed over ground glass so that the target and not the filament was imaged. The resolution target was 12.5 x 12.5 mm, $S_o = 219.5$ cm and $S_i = 23.5$ cm. These distances correspond to a wavelength of 552 nm. The x and y extents of the image were measured in MacPhase to be 134 x 134 pixels, corresponding to a transverse magnification of 0.107 with 10 μ m pixels.

$$\begin{aligned}
 M_{transverse} &= -\frac{S_i}{S_o} = -\frac{x_i}{x_o} = -\frac{y_i}{y_o} \\
 &= -\frac{23.5cm}{219.5cm} = -\frac{134pixels * 10\mu m}{12.5mm} = -0.107
 \end{aligned}
 \tag{5.2}$$

These measurements confirm that the spectral imaging and transverse magnification equations hold true for this diffractive optic.

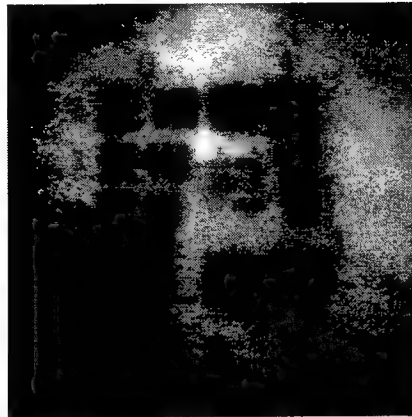


Figure 5.10: A pictorial representation of the system's MTF, a DOIS image of an Air Force Resolution Target.

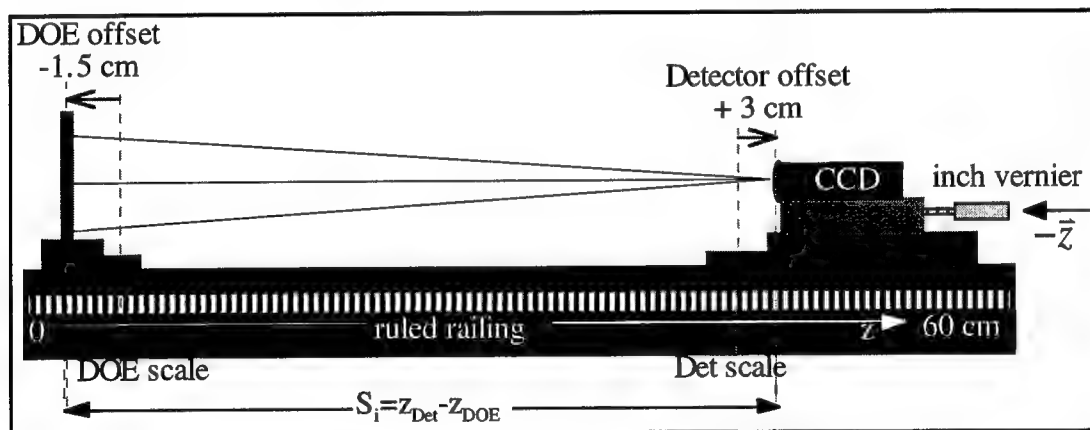


Figure 5.11: Schematic of DOIS.

It is necessary to determine the exact location of both the DOE and detector to properly determine the spectral value. Figure 5.11 is a schematic diagram of DOIS and illustrates the distances used in the excel spreadsheet, Figure 5.12, which calculates λ from S_o , the DOE and detector positions. Precise offsets between the carrier markings and the DOE and CCD surfaces are required. These were first roughly determined from the mounting parameters and then calibrated with the known HeNe and GreNe wavelengths.

Once set at -1.5 cm and +3 cm, they remained accurate for a variety of source targets, wavelengths and distances.

S _o [cm]	DOE scale [cm]	Det scale [cm]	Inch scale [in]	calculated Z _{DOE} [cm]	calculated Z _{Detector} [cm]	calculated S _i [cm]	calculated lamda [nm]
*	*	*	*	DOE scale -1.5 offset Z _{DOE}	Det scale + 3 offset - inscale*2.57 Z _{Detector}	Z _{Detector} - Z _{DOE} S _i	$\lambda = \lambda_d f_d * \frac{1}{f}$ $= \lambda_d f_d * (\frac{1}{S_o} + \frac{1}{S_i})$
-data is entered here --							

Figure 5.12: Excel spreadsheet calibrating the DOE and detector carrier locations z, to a corresponding wavelength, λ .

5.5 Spatial and Spectral point spread function (psf)

Figure 5.13 is a series of images (32 x 32 pixels) of a 5 μ m pinhole illuminated by a HeNe laser recorded with DOIS through focus. The separation between each image is $dz = .005''$, which is approximately a spectral step size of $d\lambda = 0.4$ nm. Each image is plotted with its own min, max plot range to maximize the contrast and boldly show the spot diagram pattern. The geometrical image at best focus is contained within one pixel, so this will experimentally represent the system's spatial psf for various stages of defocus. These images not only tell us the amount of blur added to our image, but they also graphically demonstrate the dominant lens aberration, third order spherical. The spot diagrams correspond to under corrected spherical aberration. Notice the soft even blur as the images progress into focus, but then the hard ring of light after focus. Figure 5.14 is a collection of the cross sections of each of these psfs grouped as "approaching focus" and "leaving focus" respectively, and plotted as greyscale intensity value verses pixel number. The spectral images are each 32x32 pixels. Notice that the 255 greylevel maximum of the psf is centered on pixel number 16 and falls off quickly to a greylevel of zero within 6 pixels on either side (shown are pixel numbers 10 through 22, beyond them the psf is zero).

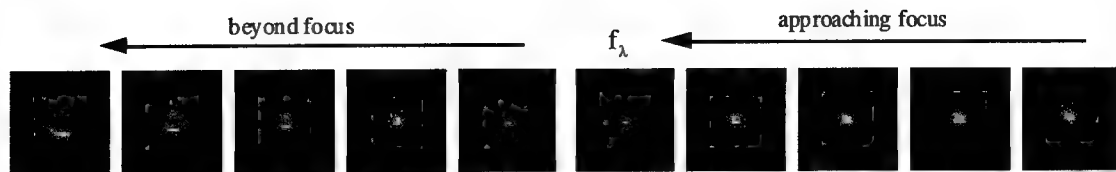


Figure 5.13: Series of images (32 x 32 pixels) of a 5 μm pinhole illuminated by a HeNe laser recorded with DOIS through focus.

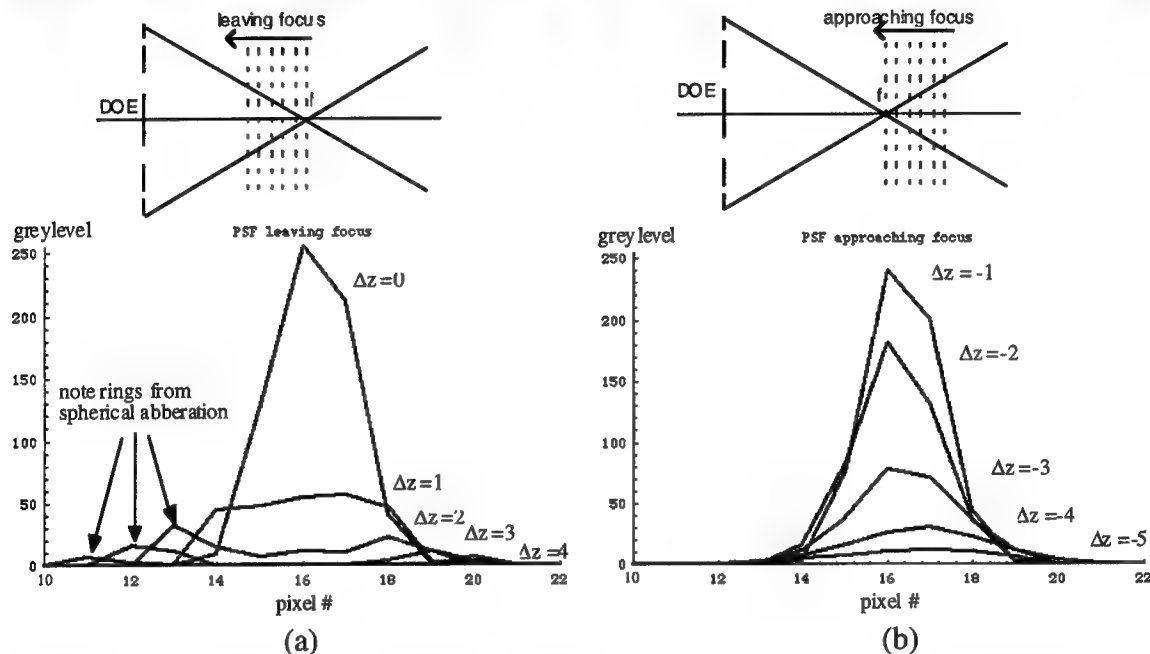


Figure 5.14: Spatial Impulse response $h(r)$ at 632.8 nm, plotted as greylevel vs. pixel number for locations (a) approaching focus. (b) leaving focus.

Another important system parameter can be obtained from this data set. Plotting the intensity distribution of one pixel through focus becomes a measure of the influence of one slice of the data on the next plane of data. In 3D microscopy this measures the degradation in image quality of one spatial plane z on the next, but in this configuration it is a measure of the degradation of one wavelength by the surrounding spectral channels. This translates into the spectral impulse function which determines spectral bandwidth or resolution of the system. The experimentally determined coherent spectral impulse function $h(\lambda)$ is plotted in Figure 5.15, the intensity distribution of the center pixel through focus at (a) 632.8 nm HeNe and (b) 542 nm GreNe.

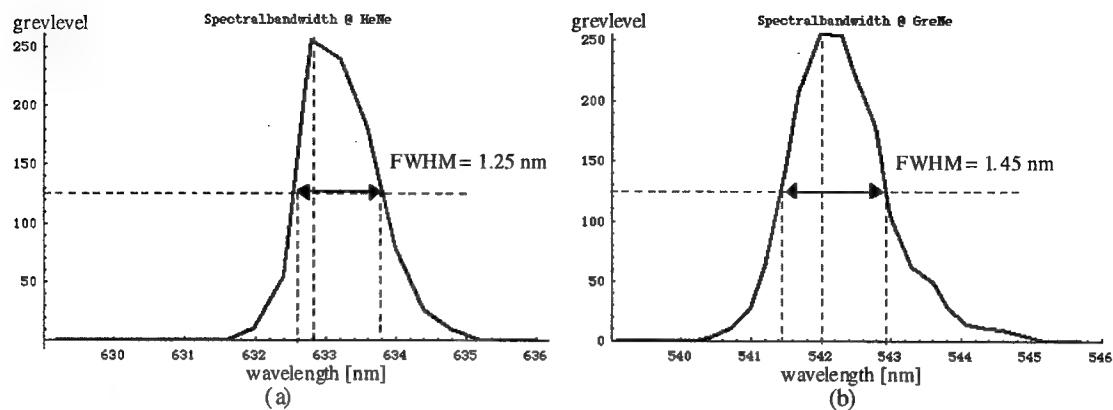


Figure 5.15: Spectral Impulse response $h(\lambda)$, plotted as intensity of one pixel through focus (a) for 632.8 nm. (b) for 542 nm.

calibration source	center wavelength λ_c	spectral resolution $\Delta\lambda$	relative resolution $\Delta\lambda/\lambda_c$	resolving power $\lambda_c/\Delta\lambda$
HeNe	632.8 nm	1.25 nm -0.25 and +1	0.197 %	527
GreNe	542 nm	1.45 nm -0.55 and +0.9	0.267 %	373

Figure 5.16: The experimentally determined spectral resolution.

These spectral psfs can be scaled with wavelength to translate through the entire visible range. Each step size is $dz=.005''=.127 \text{ mm}$, HeNe $dz/z_\lambda=.0127/20.93=.06\%$, GreNe $dz/z_\lambda=.0127/24.91=.05\%$. To use the experimentally determined GreNe psf data increments of $dz/z_\lambda=.05\%$ should be used. For example, to filter properly at 450 nm, $z=29.4 \text{ cm}$, the step size dz should be equal to $0.15 \text{ mm} \approx .006''$.

6. IMAGE FORMATION

The previous chapters have concentrated on describing DOIS's operation theoretically. At this point it is useful to try and verify that the theory does indeed predict the image formation function of DOIS. This Chapter presents both computer generated (CG) and experimentally determined image sets of known targets. As you will see, the linear system theory of Chapter 4 accurately predicts output images formed by DOIS. The CG images are very similar to those experimentally measured, which verifies that the theory is appropriate.

6.1 Mercury 577/579 nm doublet with an X aperture

An excellent example of DOIS's performance is its ability to resolve a two nanometer doublet (577/579nm) from a Mercury Lamp. To test both spectral and spatial imaging, a known aperture was placed in front of the lamp. The aperture was two crossed slits in metal that make an X. The lamp was positioned at the same object distance that the GreNe pinhole psf images were recorded at and images were recorded every $dz=0.125\text{mm}$ corresponding to a spectral step size of $d\lambda=0.3\text{nm}$.

The algorithm in section 4.2 was implemented in *Mathematica* and used to simulate the experimental scenario. Figure 6.1 highlights the *Mathematica* code for this model. It creates a three-dimensional (32x32x32) **image** matrix, from 2 three-dimensional input matrices, a spectral **object** matrix and the measured **psf** matrix [Figure 2.12]. Each is formed by stacking 32 images that are 32 by 32 pixels in dimension.

OBJ =centeredFourier[Flatten[object]]	(6.1)
OTF =centeredFourier[Flatten[psf]]	(6.2)
IMAGE = OTF * OBJ	(6.3)
image =Partition[Abs[centeredInverseFourier[IMAGE]]]	(6.4)

Figure 6.1: *Mathematica* code that implements the linear system algorithm.

For this simulation it was assumed that Mercury emits two narrow lines at 577 nm and 579 nm. Pictured in Figure 6.2 is the series of assumed input objects, paired with the CG output images that were generated from the *Mathematica* linear system algorithm, along side the experimentally measured images. The input object was assumed to have non-zero values in channels 7,8,9 and 14,15,16 exclusively, corresponding to wavelengths of 576.6, 576.9, 577.2, 578.7, 579.0 and 579.3 nm. The corresponding object spectral radiance curve is Figure 6.3(a) showing emission only around 577 nm and 579 nm. The experimentally measured OTF matrix from Figure 2.14 was used.

The images created by this algorithm accurately depict the image formation properties of DOIS. In Figure 6.2 you can see the excellent correlation between the CG and the experimentally recorded images of the third columns. The spectral radiance curve of the CG images is Figure 6.3(b). As expected the psf does degrade the spectral separation of the doublet. Yet, the doublet can still be detected and can be restored with various deconvolution techniques [Chapter 8]. The corresponding spectral curve from the experimental image set is Figure 6.3(c), which shows even better spectral separation.

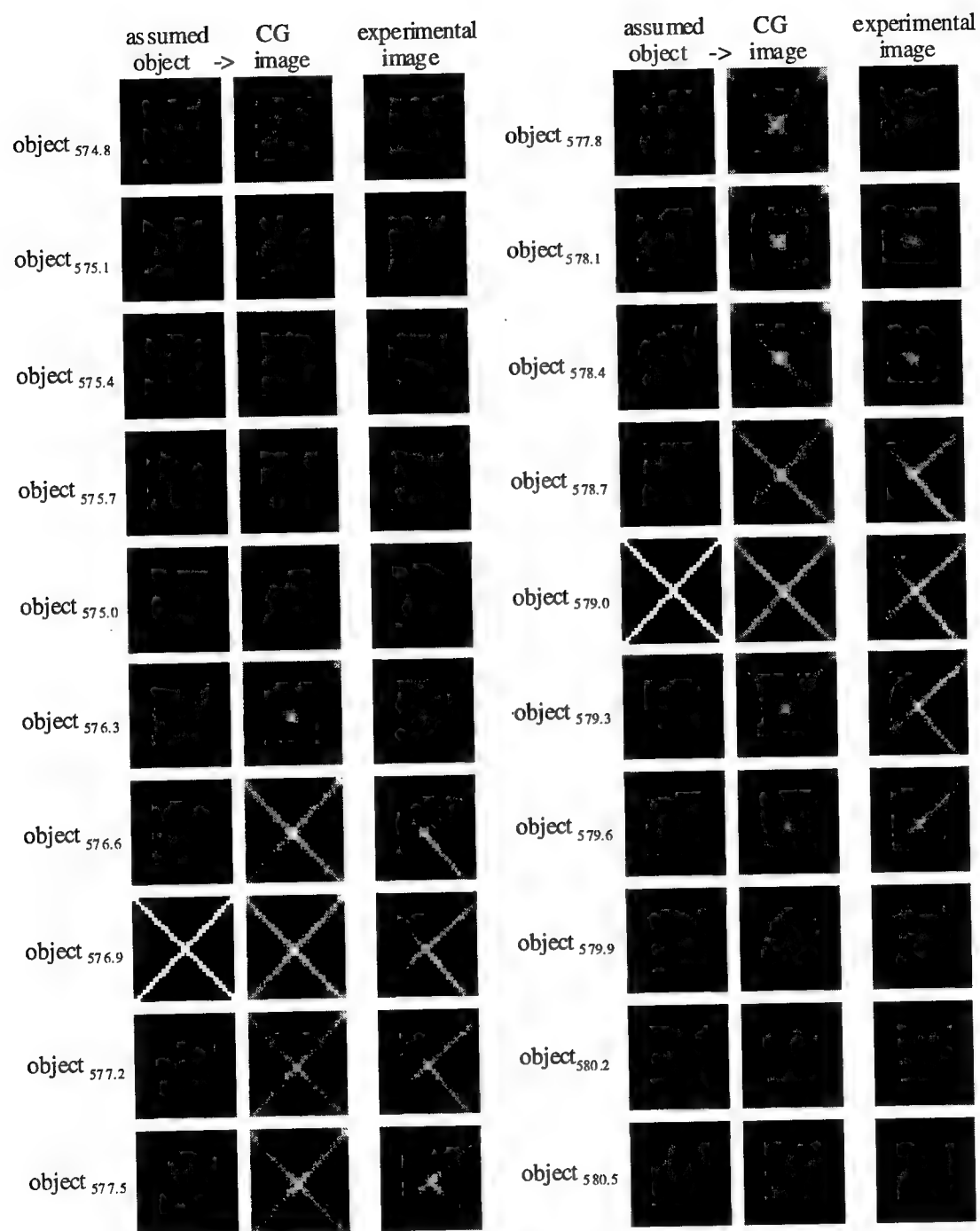
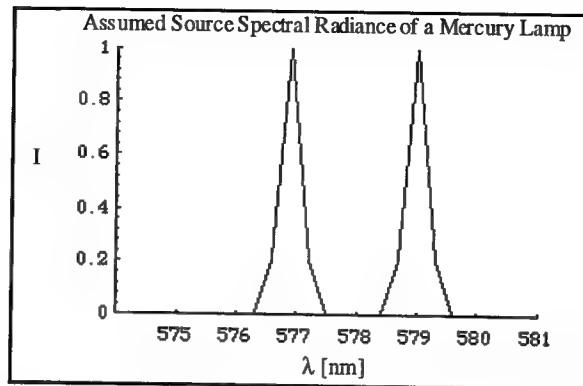
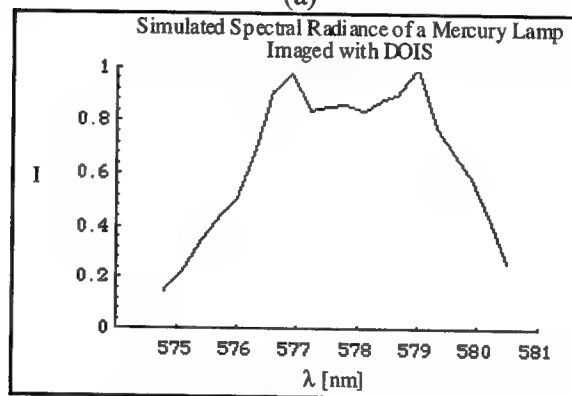


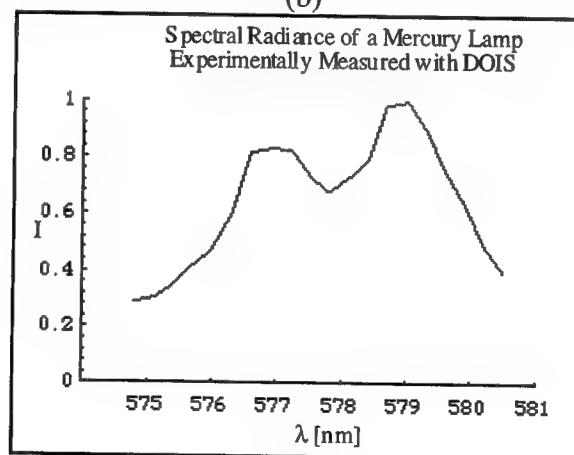
Figure 6.2: Simulated spectral object & image channels of a Mercury doublet X, using experimentally measured $\text{psf}(x,y,z(\lambda))$.



(a)



(b)



(c)

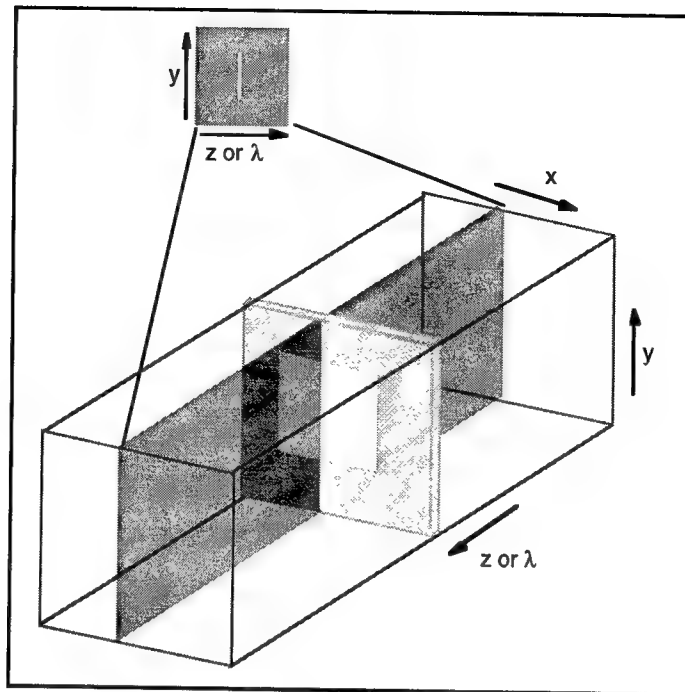
Figure 6.3: Spectral radiance plots of a Mercury doublet 577/579nm (a) the assumed input source object. (b) the computer generated results. (c) the experimental result.

6.2 Spectral/spatial analysis

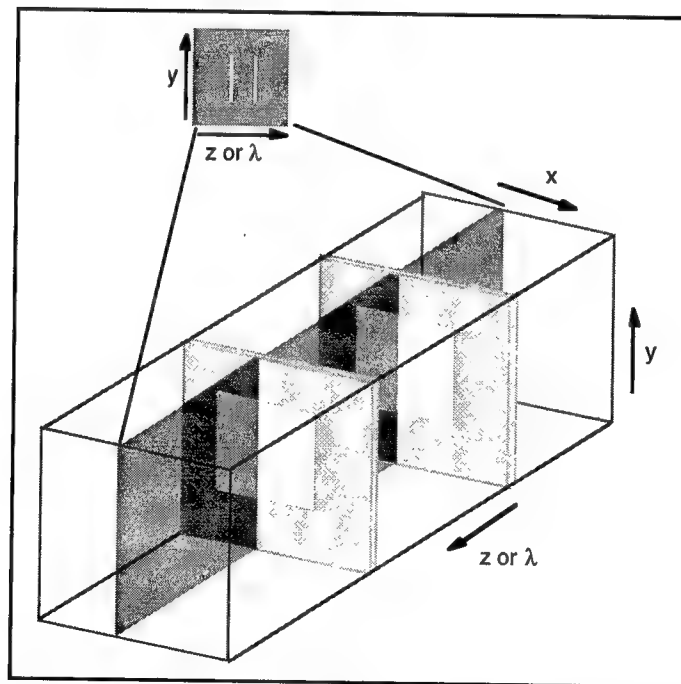
The above target demonstrated high spectral resolution by being able to discern a 2nm doublet while imaging the narrow slits of the X. Small targets encounter only minimal blurring; however as the target increases, so does the spectral/spatial blurring. This is investigated by generating CG images of targets of varying spatial extent with the Fourier model using the measured OTF.

The data can be displayed in many ways. A conventional representation is a series of spectral images like Figure 6.2, or a spectral curve at one pixel, Figure 6.3. However to visualize the spectral/spatial relationship, the following discussion will utilize a spectral/spatial cross-section image. Figure 6.4 shows two three-dimensional data cubes. The cross-section is formed as a $z_\lambda x$ or $z_\lambda y$ plane, shown as the images above the cubes.

Notice that the monochromatic $z_\lambda y$ image looks like a slit and the image from the doublet emission looks like a double slit. The height of the slit represents a dimension of the aperture of the target and the width is the spectral bandwidth of the emission line. Figure 6.5 presents the spectral/spatial on-axis cross-sections of the point spread functions used during this project. The contrast has been enhanced to show features.



(a)



(b)

Figure 6.4: 3D object cube and zy view of a rectangular aperture emitting (a) monochromatically (b) a doublet source.

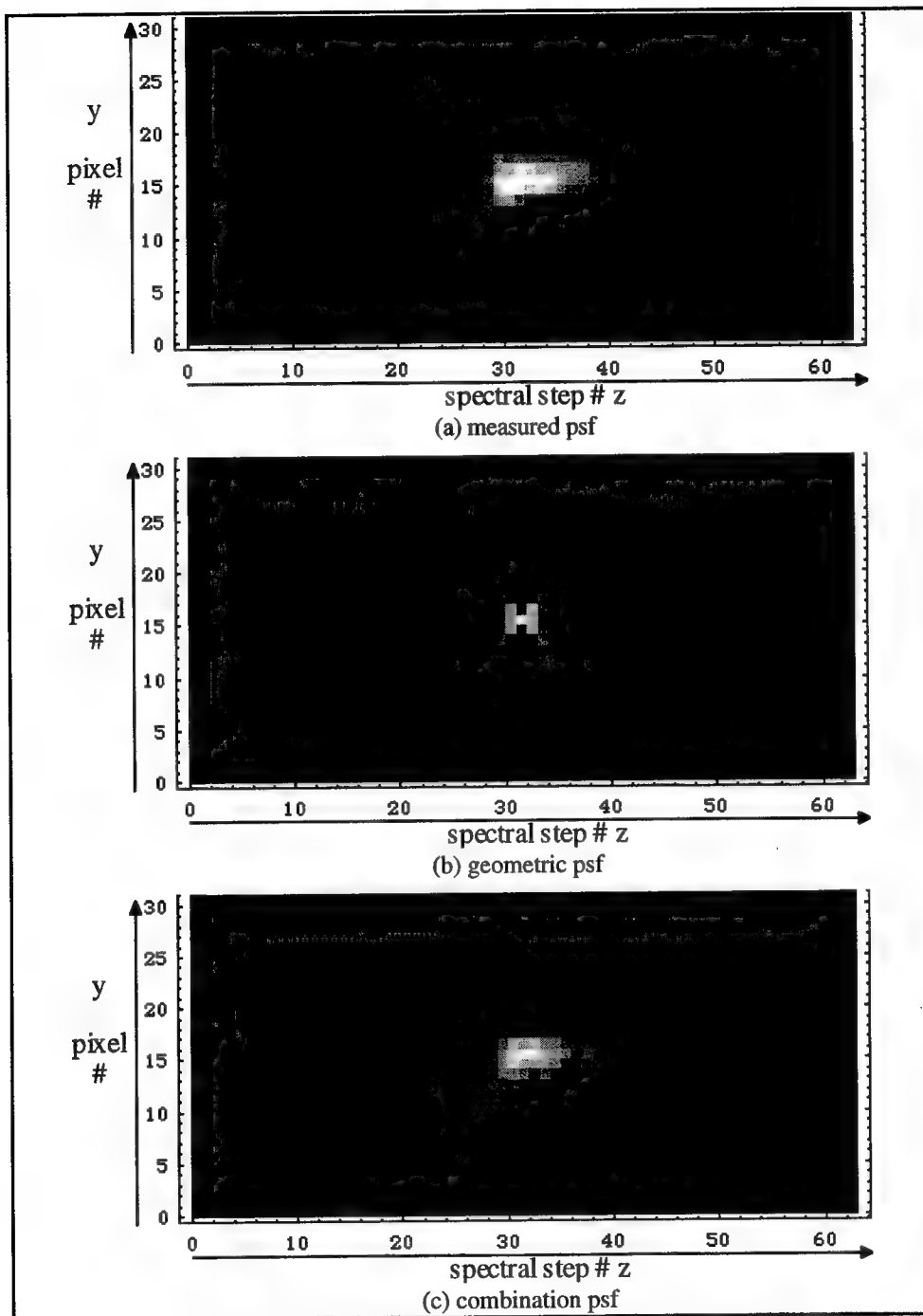


Figure 6.5: Cross-sections of the three-dimensional point spread functions used in CG image formation and object reconstruction.

6.2.1 Monochromatic target, increasing aperture

Linear system theory was used to model the images formed by DOIS of a monochromatic target with six rectangular apertures of different sizes. The cross-sections are shown in Figure 6.6. The images were generated by forming a 3D matrix, $32 \times 32 \times 32$ where the only non-zero elements are a square of ones in the 16^{th} plane, simulating a square monochromatic target. The size of the square is increased from 1 pixel to the full 32×32 plane (1, 2, 4, 8, 16 and 32 pixels respectively). As expected, as the target size is increased its total radiance is increased, causing increased blurring in both the spectral and spatial directions. Each two-dimensional image is a 32×32 $z_\lambda y$ cross-section of the total three-dimensional cube with the corresponding spectral curve plotted below it.

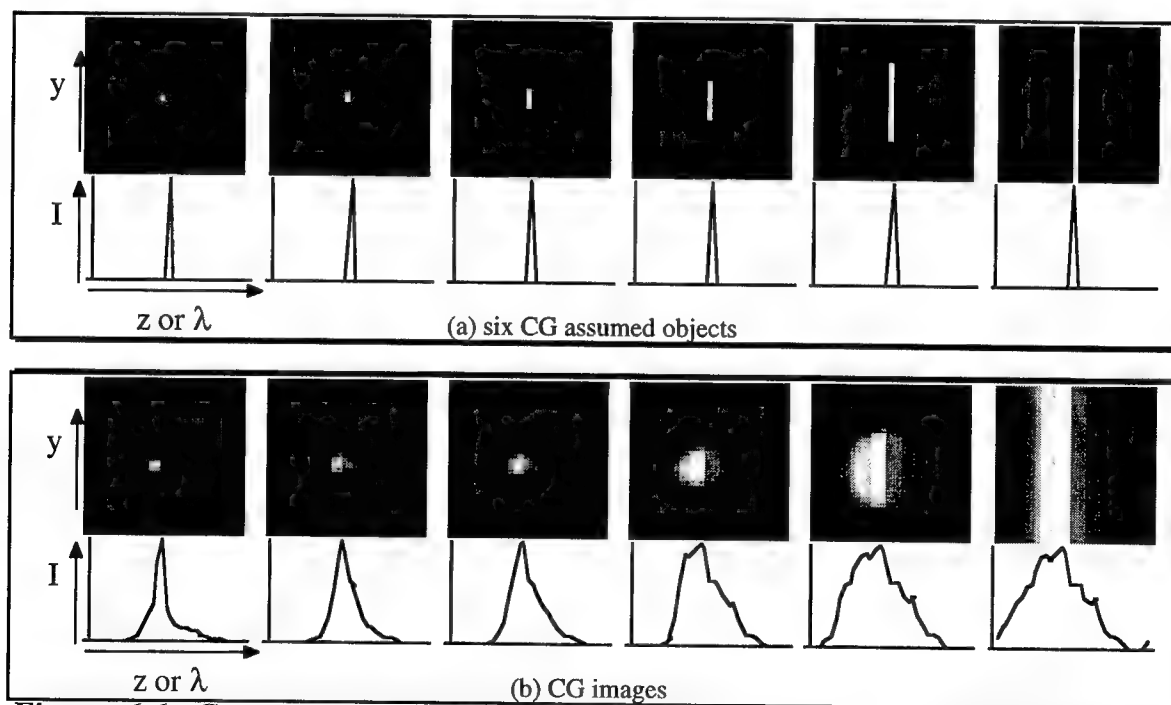


Figure 6.6: Computer generated monochromatic target of increasing size.

6.2.2 Doublet target, increasing aperture

A more interesting target is the same increasing square aperture in front of a doublet. The images in Figure 6.7(a) are the CG assumed input sources with the square

aperture at $z=14$ and 20 . The series in Figure 6.7(b) are the CG images which were calculated with the measured OTF. For comparison a mercury lamp with 577nm and 579nm line emissions illuminated various apertures. The measured z,y images were extracted from the measured cubes and shown in Figure 6.7(c). Notice the strong agreement between the simulated and experimental images and curves:

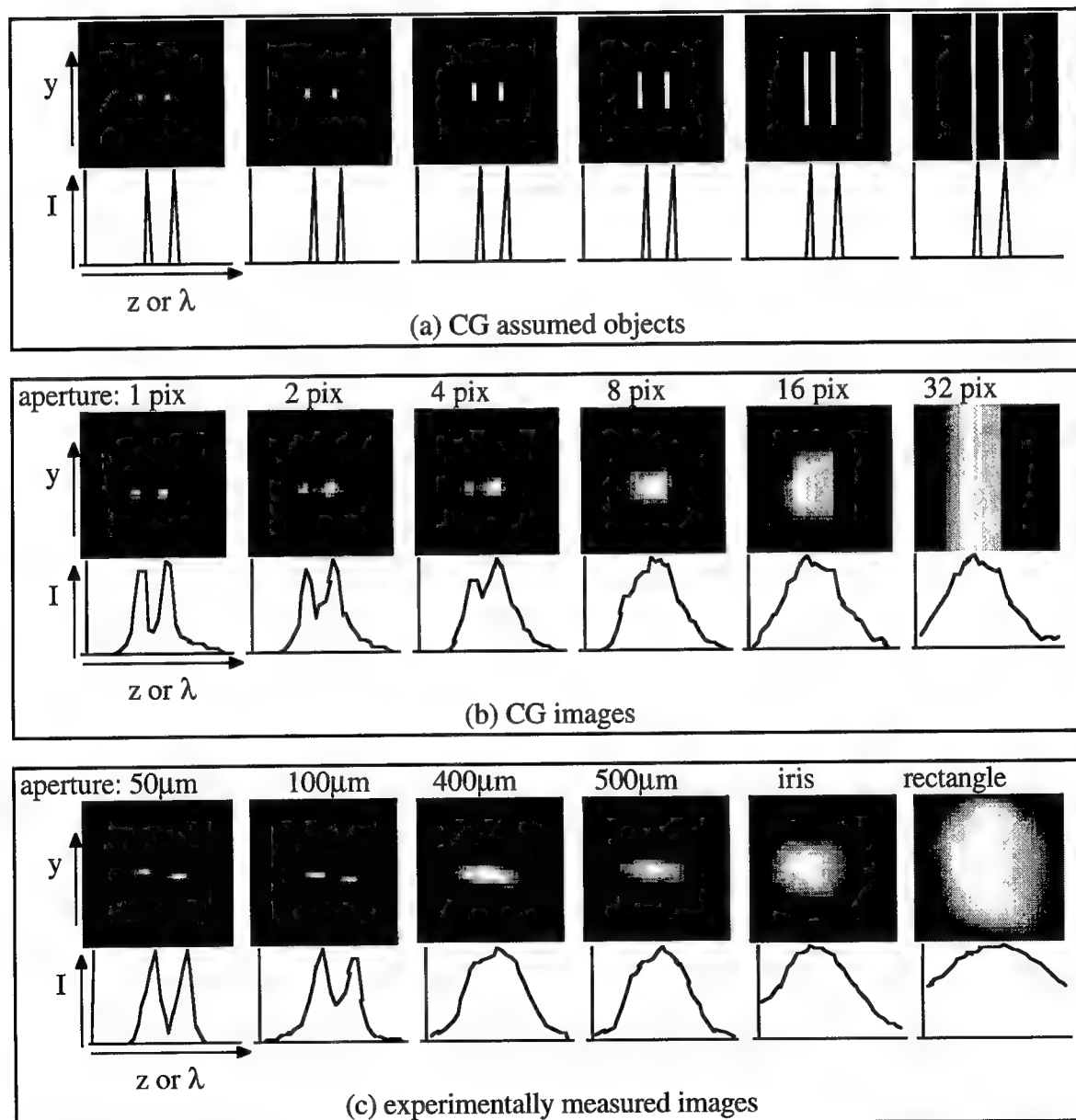


Figure 6.7: Computer generated (CG) and experimentally recorded doublets of increasing size.

Looking at the experimentally measured image of the 50 μ m and 100 μ m apertures on the left side of Figure 6.7, notice that the target drifted to a lower pixel in the y direction as the detector was scanned along the z axis. This misregistration visualizes the effect of both a changing magnification and off axis aberrations which skew the orientation of the point spread function, Figure 6.8. This artifact can be eliminated with a constant magnification design which is optimized for minimum aberrations.

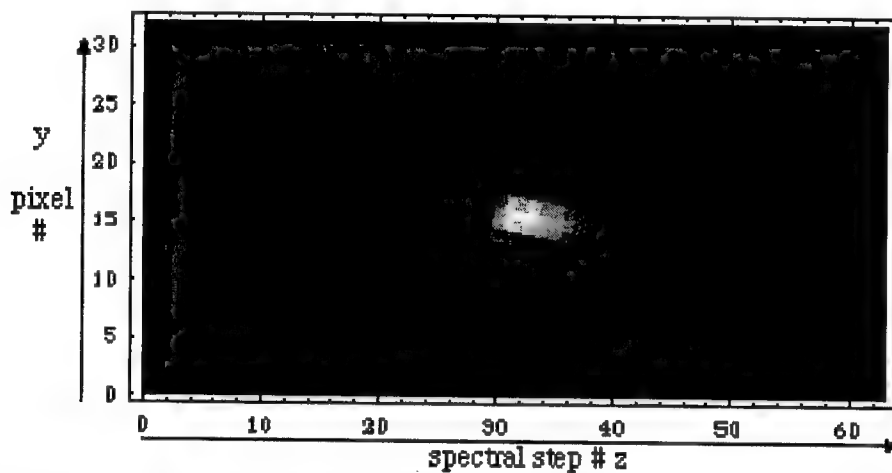


Figure 6.8: A point spread function askew from off-axis aberrations.

Another instance to be discussed while investigating targets of increasing size is when the target is imaged to the edge pixels of the CCD. If the target is imaged to the edge of the detector array field-of-view (FOV), the information about the target which is blurred outside of the FOV will be lost. Additionally, the simulation and reconstruction algorithms are based on transfer theory assuming a shift-invariant point spread function. Mathematically this assumes that the psf and OTF matrices are circulant, that each row has equivalent elements where the values are shifted and the end value wrap around to the other side as shown in equation (6.5).

$$\begin{bmatrix} a & b & c & d \\ d & a & b & c \\ c & d & a & b \\ b & c & d & a \end{bmatrix} \quad (6.5)$$

Figure 6.9 shows the wrap around in the y direction that is assumed if the psf is on the edge of the field. A field stop is proposed to limit the FOV to be smaller than the useable detector area. Pixels outside of the FOV will record the blurred intensity from targets imaged to the edge of the FOV. By recording the fully blurred target the reconstruction will be improved.

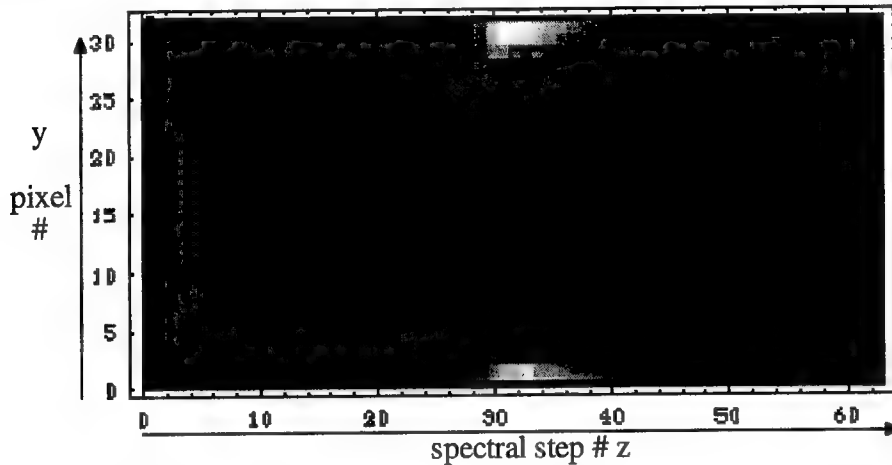


Figure 6.9: The psf of a pixel at the edge of the detection area.

7. PROTOTYPE DEMONSTRATION WITH FOUR TARGETS

The DOIS Prototype was demonstrated with four known multi-spectral/spatial targets. The sources include a Tungsten Halogen lamp, a Mercury lamp, a HeNe laser and a GreNe laser. For complete control, each source illuminated a known template which became the target. Figure 7.1 is a view of the targets imaged by a conventional lens and recorded with the monochrome CCD camera.

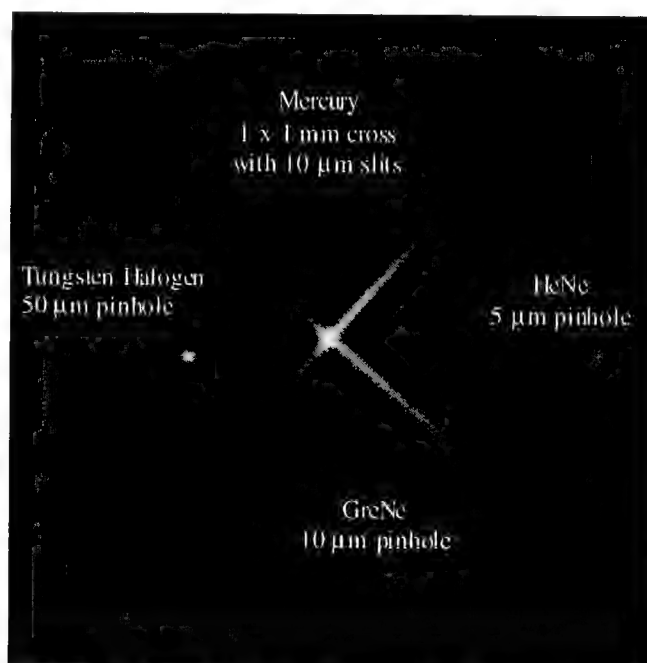
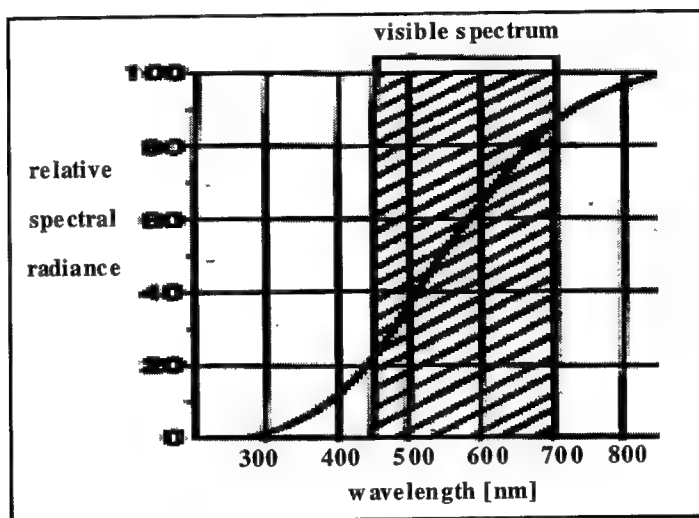


Figure 7.1: The four targets: a Tungsten Halogen Lamp, a Mercury Lamp, a HeNe and a GreNe.

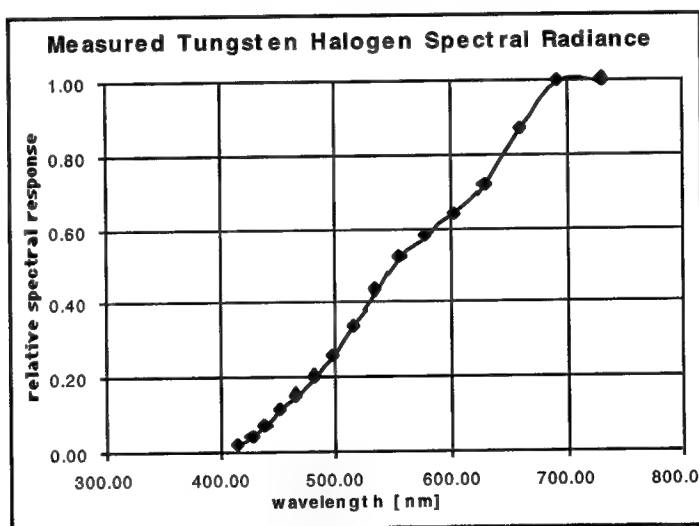
7.1 Testbed Specifications

The Tungsten Halogen lamp is a broadband source, as shown in Figure 7.2. It illuminated a 50 μm pinhole, creating a several pixel object and preventing images of the filament. The spectral emission of the Mercury lamp is shown in Figure 7.3. Mercury makes an excellent spectrometer target; it is a multi-line emitter with six major lines in the DOIS spectral range. Of particular interest are a pair of emission lines, called a doublet, at 577nm and 579nm. DOIS can resolve this doublet, demonstrating that the system's spectral

resolution is better than 2nm! The aperture used with the Mercury lamp is a 1 x 1 mm cross, X, with 10 μm slits. The remaining sources were two Helium Neon lasers. The HeNe emits at 632.8 nm and the GreNe at 542 nm. They illuminated a 5 μm and 10 μm pinhole respectively, simulating monochromatic point sources.

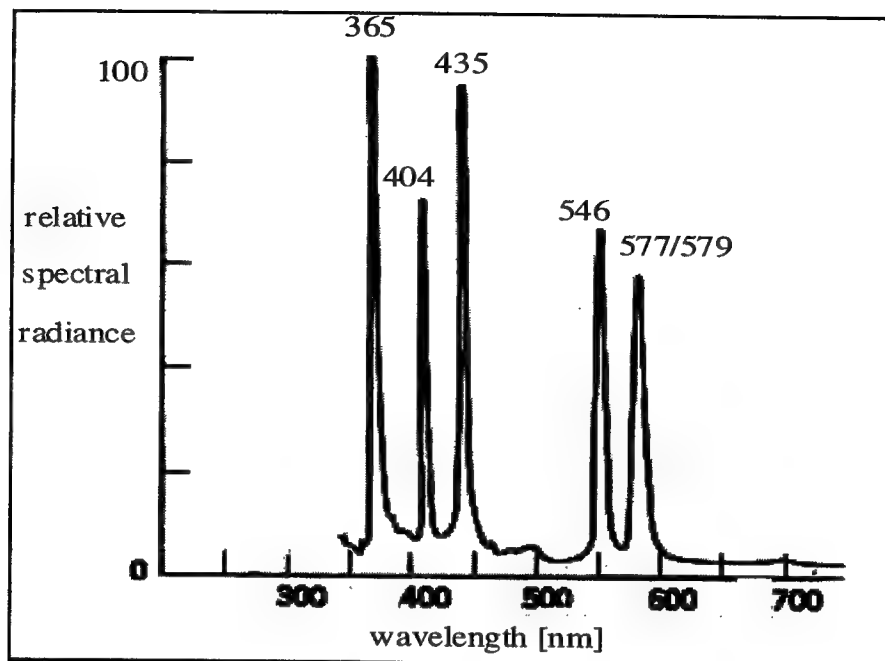


(a)

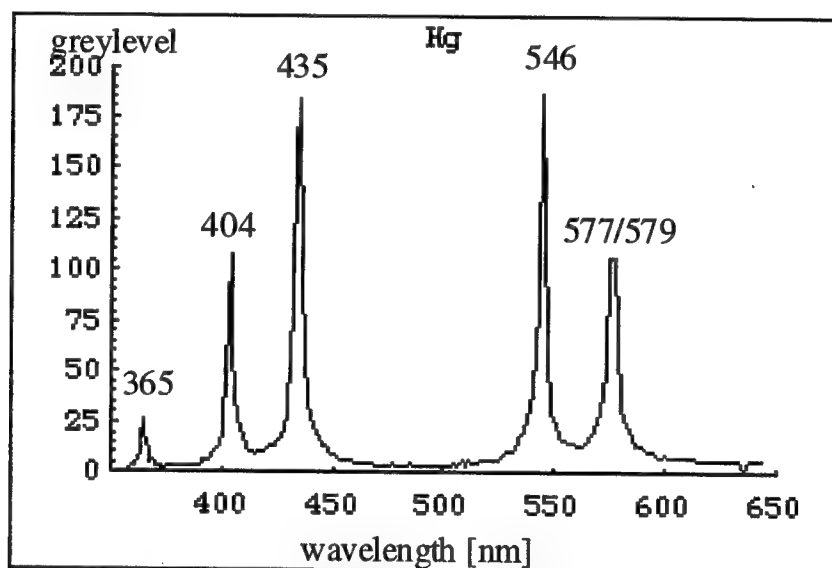


(b)

Figure 7.2: Spectral Distribution of the Newport Tungsten Halogen Lamp (a) reprinted from the Newport operations manual, (b) measured with DOIS.



(a)



(b) step size: $dz = 0.1\text{cm}$, $d\lambda = 0.8\text{nm}-0.3\text{nm}$

Figure 7.3: Spectral radiance curve of the Mercury Lamp (a) reprinted from Applied Optics, (b) measured with DOIS.

The four targets were placed an equal distance from DOIS and beamsplitters were aligned to create the illusion that they were all in the same object plane. Figure 7.3 is the schematic of the demonstration testbed. The Tungsten Halogen lamp was directly in line with DOIS. The Mercury and laser sources were reflected into the field of view with beamsplitters. The object distance s_o was 91.5" and the DOE was held constant. The CCD camera was manually scanned and the detector carrier location and inch scale readings were recorded for each spectral image. The 256x256 monochromatic images of each target at different wavelengths is given in Figure 7.5.

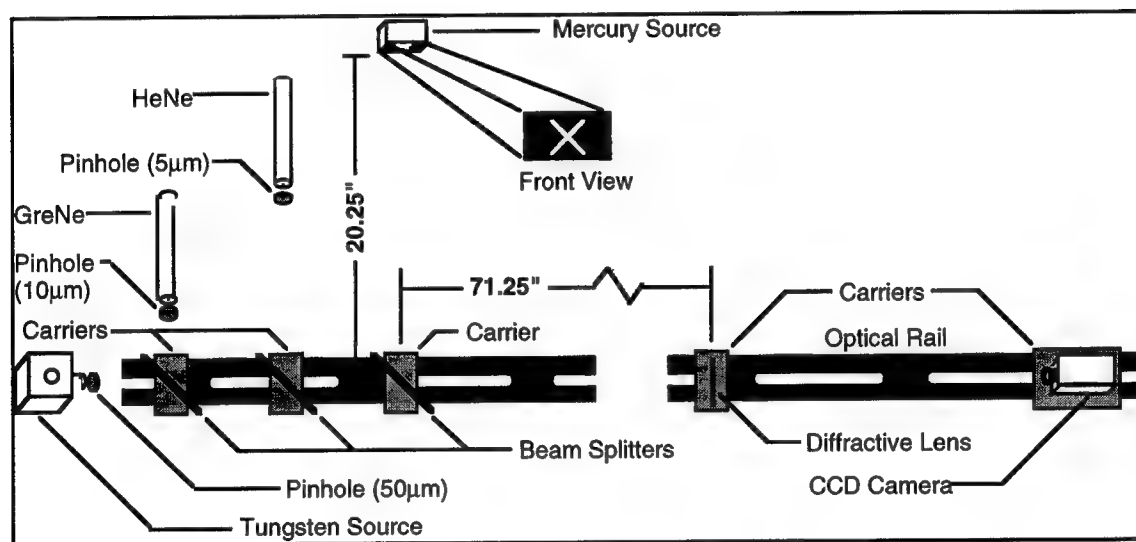
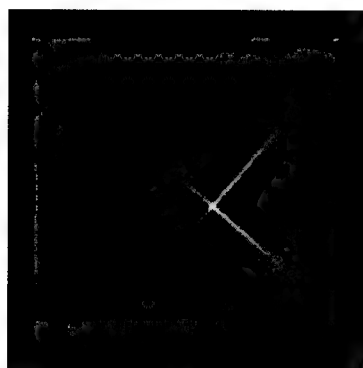
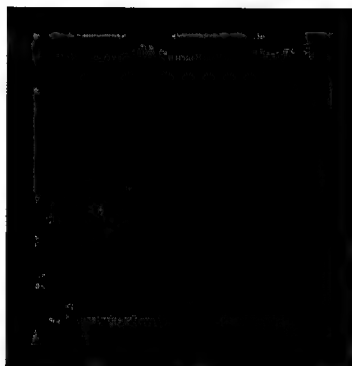


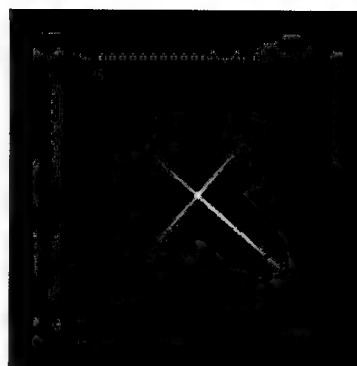
Figure 7.4: Schematic of the four target testbed.



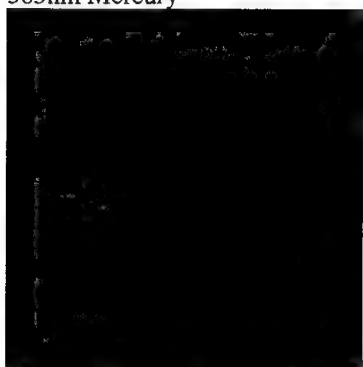
365nm Mercury



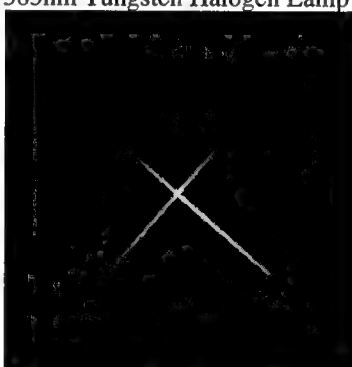
383nm Tungsten Halogen Lamp



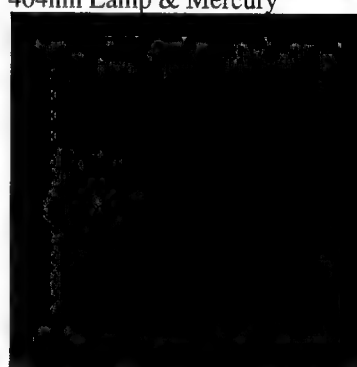
404nm Lamp & Mercury



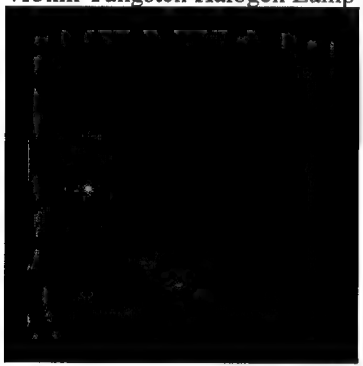
415nm Tungsten Halogen Lamp



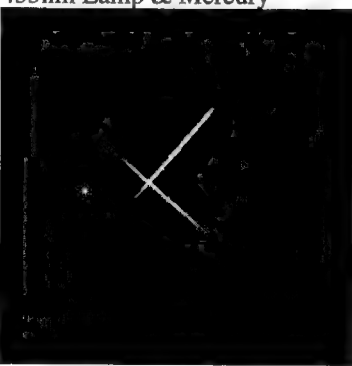
435nm Lamp & Mercury



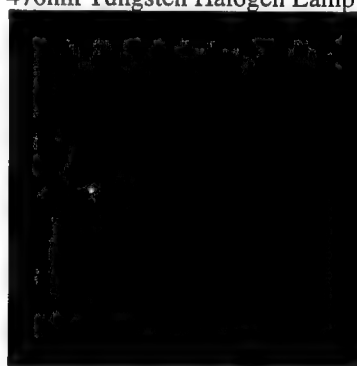
470nm Tungsten Halogen Lamp



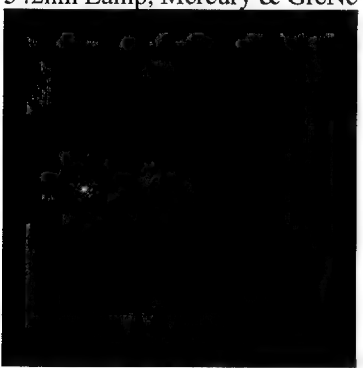
542nm Lamp, Mercury & GreNe



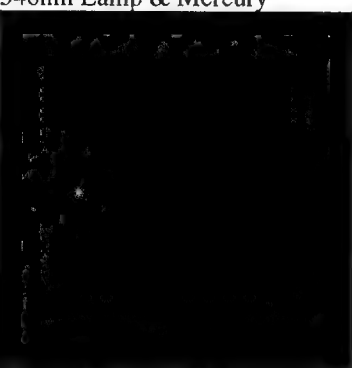
546nm Lamp & Mercury



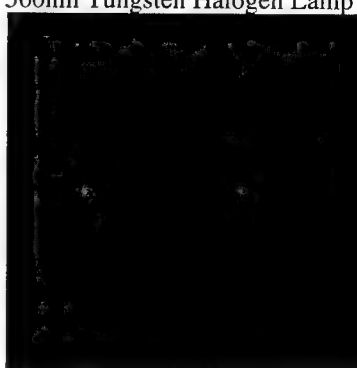
560nm Tungsten Halogen Lamp



578 Lamp & Mercury



600nm Tungsten Halogen Lamp



632.8nm Lamp & HeNe

Figure 7.5: Sample of the key spectral DOIS images in this demonstration.

7.2 Results

DOIS was used to image the multi spectral/spatial targets. As previously discussed, the DOE was kept stationary and the detector was stepped through a wide range of distances. As the detector was moved, the various targets popped in and out of the image depending on their spectral content, as seen in Figure 7.5. However, since Tungsten Halogen is a greybody emitting over the entire visible range, the image of the 50 μ m pinhole was present continuously in the z range for λ from 383nm to 650nm. The Tungsten pinhole's intensity grew at longer wavelengths and its center shifted several pixels because of the magnification changes. The best focus of each spectral line was determined and the corresponding detector locations were recorded. The table in Figure 7.6 shows the calculation of the emission line peak wavelengths from this experiment. The results correspond perfectly to the known emissions of the lasers and the Mercury lamp of Figure 7.4, and are remarkably precise considering the manual stepping and reading of the carrier location.

source	s_o [cm]	DOE carrier	Det carrier [cm]	Inch scale [in]	s_i [cm]	emission line peak wavelength [nm]
HeNe	232.41	7	24	0.508	20.2	633
Hg Lamp	232.41	7	26.1	0.515	22.3	579
Hg Lamp	232.41	7	26.1	0.481	22.4	577
Hg Lamp	232.41	7	27.5	0.4875	23.8	546
GreNe	232.41	7	27.7	0.504	23.9	542
Hg Lamp	232.41	7	34.3	0.488	30.6	435
Hg Lamp	232.41	7	36.8	0.51	33.0	407
Hg Lamp	232.41	7	36.8	0.396	33.3	404
Hg Lamp	232.41	7	41	0.43	37.4	365

Figure 7.6: Peak spectral lines of the target, calculated from the locations of best focus.

Attempts were made to experimentally verify the Mercury lamp's spectral emission curve with the grating monochrometer. Of particular interest is the doublet at 577 nm and 579 nm. The signal from the lamp was low and the smallest useable exit slit width was $\approx .2$ mm corresponding to a bandwidth of 5 nm making the results unusable. However, this emphasizes the usefulness of even this inefficiently designed DOIS.

To determine the spectral radiance curves of the targets, series of images were recorded with known increments of dz . The spectral radiance is defined as the intensity value of the image at various wavelengths. A C program was written to open each image and record the value of a specific pixel in a list. This list was plotted against wavelength creating a measured spectral radiance curve. A different approach needed to be implemented when the change in magnification throughout the spectral range caused the image to drift across several pixels. Under this condition, a window was defined around the image location and the value extracted for each image is the maximum pixel value in the window.

The experiment was executed twice, each time with a different spectral resolution. The first data run was low resolution, testing the entire visible spectrum. It incorporated manual translation of the detector carrier in increments of $dz=0.1\text{mm}$. The inch scale vernier was at a constant setting. The second was high resolution, concentrating on a limited spectral range around each emission line. The detector carrier was kept stationary and the inch vernier was adjusted in $0.005''$ or $0.01''$ increments.

The results from the $dz=0.1\text{mm}$, low resolution recording of the Mercury Lamp are plotted in Figure 7.4(b). There is excellent agreement between the measured and known spectral emission lines of the characteristic curve 7.4(a) from *Applied Optics*[Levi 1968]. However, the DOE diffraction efficiency [Figure 5.5] weighted the relative intensity of each spectral line.

The results from the Tungsten Halogen pinhole are found in Figure 7.7. Included are 6 spectral images clipped from the full images to show just the $50\mu\text{m}$ pinhole. The

spectral radiance plot is constructed from data recorded in low resolution steps. The measured data points are plotted as * and a line represents the best fit. An artifact of the changing magnification is that the image drifts from a condition of being centered on a pixel to one where the image straddles several pixels, as shown in Figure 7.8. This alignment problem explains the ripple effect on the intensity versus wavelength curve.

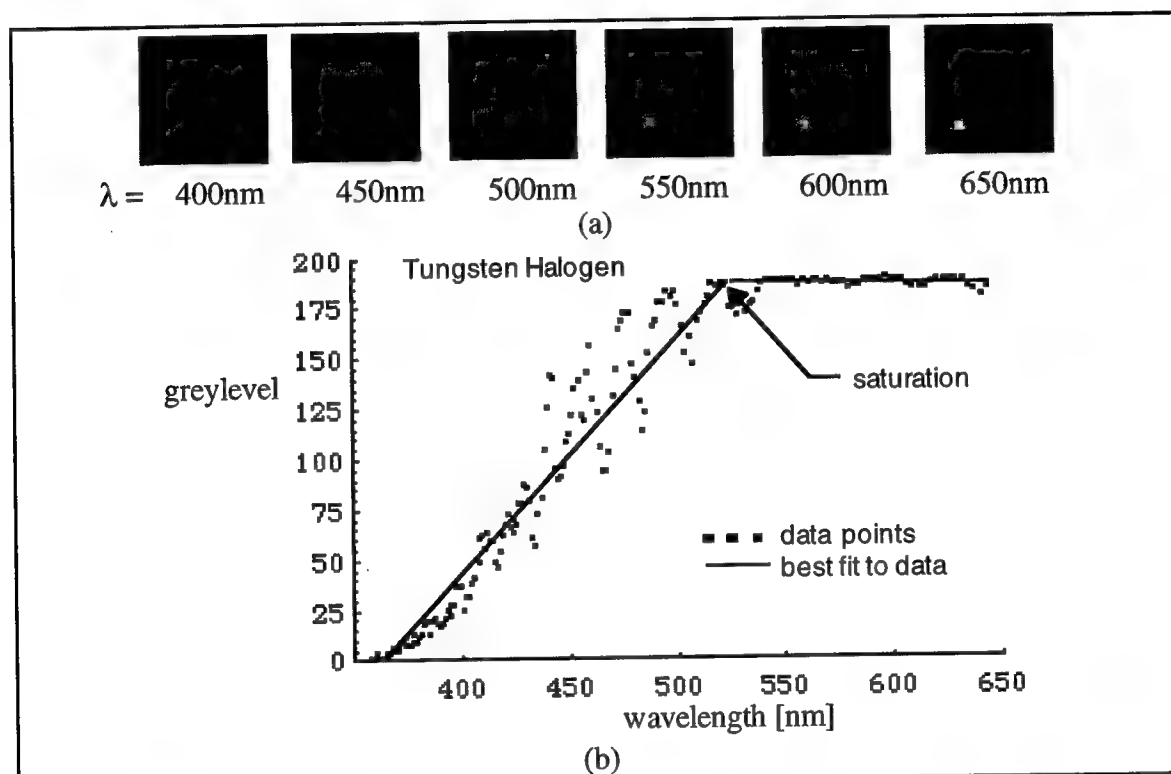


Figure 7.7: Tungsten Halogen Data (a) spectral images of the 50μm pinhole. (b) the measured spectral radiance curve.

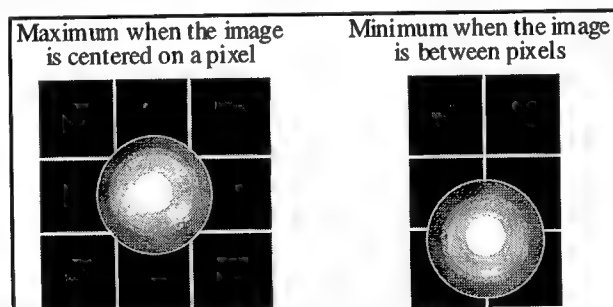


Figure 7.8: Sketch of image drifting between pixels.

Another difficulty of this data run was that the signal beyond 525nm saturated the detector array. A more accurate plot of the Tungsten Halogen is found in Figure 7.3(b). The experiment was run again with a larger source whose image was several pixels, avoiding pixel hopping, and with the gain set to prevent saturation. The results accurately measure the spectral radiance when compared to the handbook curve in Figure 7.3(a).

The results from the GreNe and HeNe laser sources are shown in Figures 7.9 and 7.10. In addition to the spectral radiance plots, a representative series of images is given in each figure. The images are 32x32 windows which have been clipped from the 256x256 recorded images. As expected DOIS recorded narrowband high intensity spikes for both. Figure 7.9 shows the HeNe narrowband spectral curve centered at 632.9nm. Figure 7.10 shows the same for the GreNe at 542nm. Notice that with constant spatial steps, $dz=0.005''$, the change in magnification causes the spectral step size to change within the spectral range. At 634nm, the spectral steps were 0.4nm, yet at 541.5nm, $d\lambda=0.2\text{nm}$.

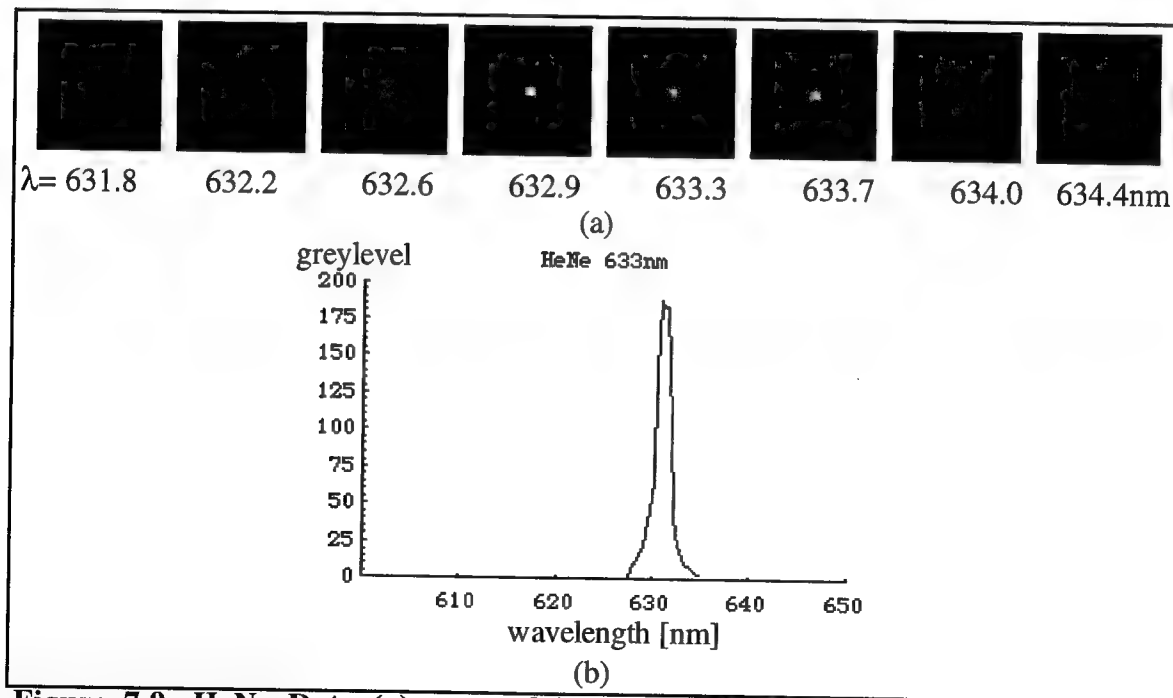


Figure 7.9: HeNe Data (a) spectral images of the 5 μm pinhole. (b) the measured spectral radiance curve ($dz=0.005''=0.0125\text{cm}$, $d\lambda\approx 0.3\text{-}0.4\text{nm}$).

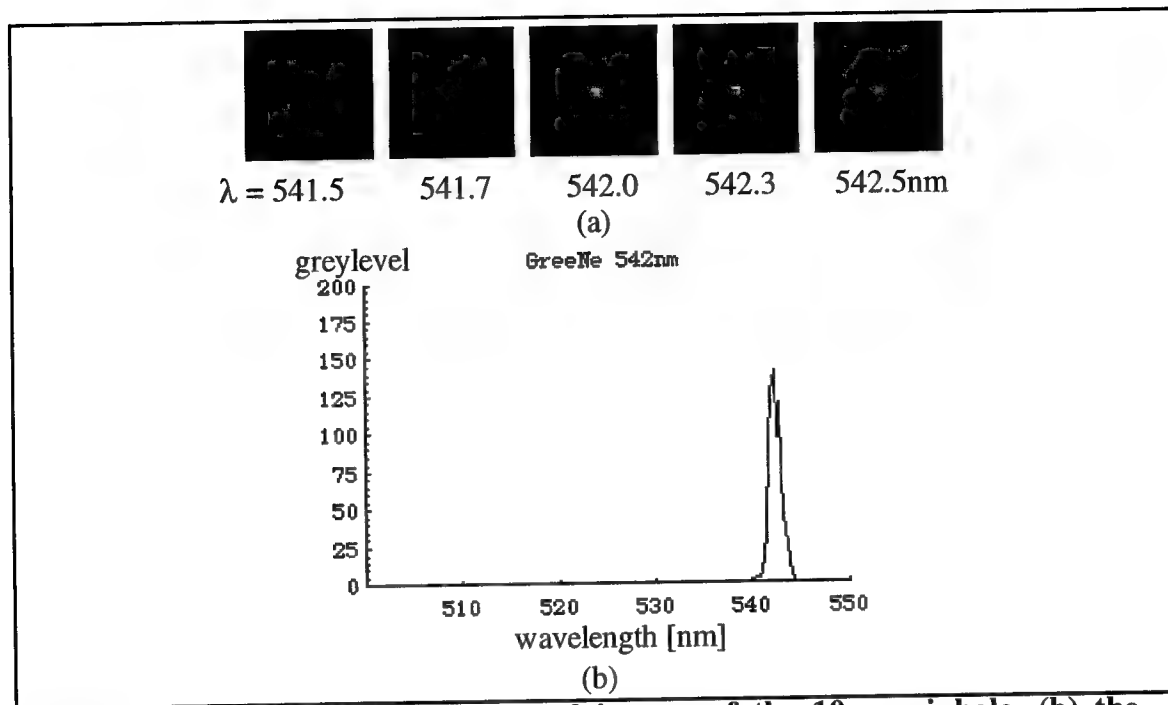


Figure 7.10: GreNe Data (a) spectral images of the 10μm pinhole. (b) the measured spectral radiance curve ($dz=0.005''=0.0125\text{cm}$, $d\lambda\approx 0.2\text{-}0.3\text{nm}$).

The Mercury target was examined a second time with small step sizes around each Hg emission line. Figure 7.11 shows the resulting spectral curves for the 365, 404, 435, 546 and 577/579nm lines with the clipped infocus spectral images.

Close observation of the 576.9nm image in Figure 7.11(e) reveals a focused cross with a highly defocused cross, and a the center that looks like a diamond. Moving to 579nm, the diamond comes to focus as the center of the 579nm image, and the 577 cross defocuses and disappears. This corresponds to the computer generated images in Chapter 6.1. This recorded data around the 577nm and 579nm Hg doublet shows that the doublet is resolved without processing. However, still greater discrimination is obtained with the processing applied in Chapter 8.

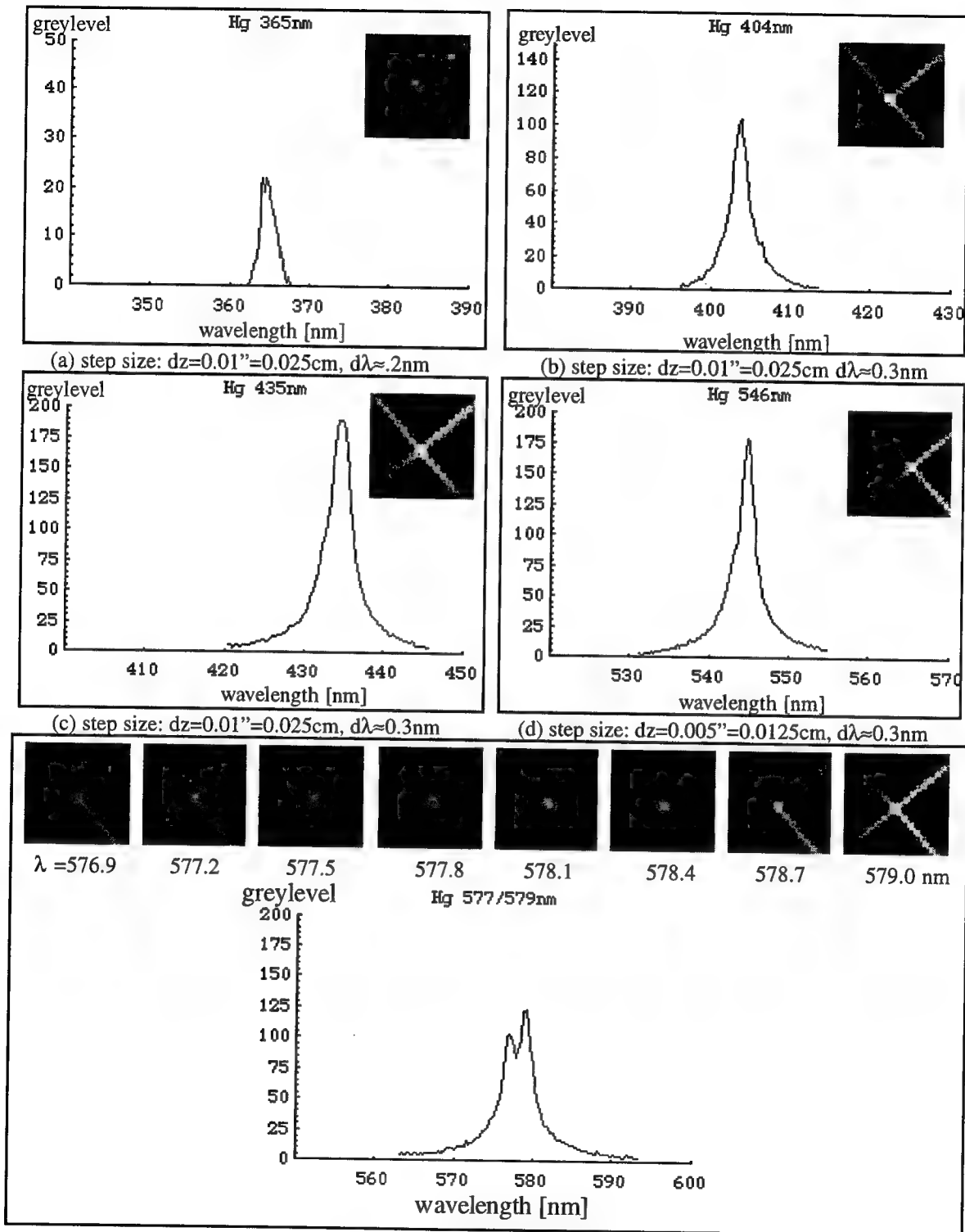


Figure 7.11: The measured spectral radiance curves of each Mercury line with the in-focus 32x32 pixel spectral image(s) of the center of the cross, (a) 365nm line. (b) 404nm line. (c) 435nm line. (d) 546nm line. (e) 577/579nm doublet.

8. OBJECT RECONSTRUCTION ALGORITHMS

The results in Chapter 7 show that DOIS performs image spectrometry. The image quality and spectral resolution available directly from DOIS will be useful in many applications. Notwithstanding, applying an object reconstruction algorithm can improve DOIS's performance by removing the blur from surrounding channels, resulting in a more accurate representation of the target's object cube. Several object reconstruction/deconvolution techniques are presented here. They have been applied to both computer generated (CG) and experimentally measured 3D DOIS image cubes.

In Chapters 1 and 4, DOIS was described as a diffractive spectral sectioning device. The output of the DOE, described by the *Spectral Gaussian Coordinate Transform*, is an image space which is mathematically equivalent to the output image space of a three-dimensional imaging microscope, described as spatial sectioning microscopy.

There are proven digital image restoration techniques used in 3D microscopy that eliminate blurring from out-of-focus adjacent slices of the 3D object. It follows that these same techniques can be adapted and applied to DOIS images to remove blurring caused by the out-of-focus spectral images. This chapter reviews the algorithms which have been adapted and applied to DOIS.

Since not all applications require the same resolution, three general processing techniques will be discussed in this chapter; nearest neighbor, inverse filtering and constrained iterative deconvolution. Each approach provides different amounts of deblurring at various computational expense

The nearest neighbor algorithm reconstructs an image by looking only at the impact from the adjacent images on either side. This requires very little prior knowledge and could be applied in real time.

Inverse filtering tries to eliminate the effect of the instrument function on the output image cube. The system OTF must be known from either theoretical prediction or direct measurement. The main task is to invert the OTF and multiply the image set by this inverse. Variations include applying an apodization or regularized inverse filter for noise suppression. Additionally, tools such as singular value decomposition may be required to invert the large, possibly singular, OTF matrix. Inverse filtering reconstruction is limited by the cutoff frequencies of the OTF; frequencies beyond the cutoff can't be recovered.

Iterative techniques which apply physical constraints, such as positivity, to the reconstructed object can theoretically reconstruct frequencies beyond the OTF cutoff. An additional advantage of iterative algorithms is that they don't require the possibly difficult task of inverting the OTF matrix.

These algorithms should provide equal or greater reconstruction to the DOIS spectral sectioning system than available with spatial sectioning 3D microscopy because of two advantages. First, when imaging a 3D spatial object such as a photo-luminescent cell, the cell itself will cause blurring and information loss due to absorption and scattering through the object. The spectral dimension in DOIS won't cause this degradation. Secondly, 3D microscopy has the demanding task of removing the blur from slices with very low z-spatial resolution. The spatial image in the z direction is normally on the order of the psf blur, requiring reconstruction in the very low and noisy regions of the OTF. However in DOIS the dispersion is so great that the total spectral range translates into a Δz spatial region which is many orders of magnitude greater than the spatial z width of the psf, with a ratio similar to the radial x,y spatial imaging. Therefore, in most situations reconstruction around and beyond the OTF cutoff isn't necessary.

It is important to note that even the simplest nearest neighbor method produces a substantial improvement. However the most accurate results are obtained with the SVD Inverse Filtering algorithm.

8.1 Digital Representation

In Chapter 4 the object and image cubes were represented as continuous functions of x, y, z and λ . However as seen in Figure 2.1, the images are sampled in x and y by the detector array and in z by stepping the array along the optical axis. This is best modeled by discrete object and image functions. In practice the object, image and psf cubes are more accurately represented by three-dimensional matrices. Recall equation (4.10):

$$i(x_i, y_i, z_i) = \int_{-\infty}^{\infty} \int_{-\infty}^{\infty} \int_{-\infty}^{\infty} o(x, y, z) h(x_i - x, y_i - y, z_i - z) dx dy dz$$

this equation can be written as summations rather than integrals with discrete axis intervals Δx , Δy and Δz .

$$i(l\Delta x_i, p\Delta y_i, j\Delta z_i) = \sum_{m=1}^N \sum_{q=1}^N \sum_{k=1}^N o(m\Delta x, q\Delta y, k\Delta z) h(l\Delta x_i - m\Delta x, p\Delta y_i - q\Delta y, j\Delta z_i - k\Delta z) \quad (8.1)$$

using subscripts to describe the Δz location:

$$i_j(x, y) = \sum_{m=1}^N \sum_{q=1}^N \sum_{k=1}^N o_k(x, y) *** h_{j-k}(x, y) \quad (8.2)$$

where $x = l\Delta x_i$ and $m\Delta x$, and $y = p\Delta y_i$ and $q\Delta y$. The value of $j-k$ represents the number of steps of defocus.

8.2 Nearest Neighbor Reconstruction

The Nearest Neighbor technique is routinely used in three-dimensional microscopy for deblurring optically sectioned image sets using data from a single focal plane above and a single focal plane below to correct the central plane. This is a reasonable approximation for two reasons. First, since spectral images from adjacent focal planes will contribute most strongly to the central plane, their effects are most important to consider. Secondly, these adjacent image planes are actually a collection of all of the object channels with various

amounts of defocus. This rationale was first used by Castleman [1979] and later by Agard [1989] to justify using only the nearest neighbors:

Simplifying equation (8.2) by dropping the x and y variables, models the system as a series of spatial slices:

$$i_j = \sum_{k=1}^N o_k * h_{j-k} = \sum_{k=1-j}^{N-j} o_{k+j} * h_k \quad (8.3)$$

This simply states that the j^{th} image is a sum of convolutions of the various object spectra with the appropriate defocus psfs. Pulling out and solving for the in-focus $k=0$ term:

$$i_j = o_j * h_0 + \sum_{k=1-j}^{-1} o_{k+j} * h_k + \sum_{k=1}^{N-j} o_{k+j} * h_k \quad (8.4)$$

$$o_j * h_0 = i_j - \sum_{k=1-j}^{-1} o_{k+j} * h_k - \sum_{k=1}^{N-j} o_{k+j} * h_k \quad (8.5)$$

The h_0 is the in-focus psf of the DOE. This equation states that the object at j , convolved with the in-focus psf, is given by the image at level j minus a sum of adjacent object channels that have been blurred by out-of-focus psfs h_k .

This suggests that the object at channel j can be recovered by subtracting from the image at channel j a series of adjacent objects blurred by the defocus transfer function. If a simultaneous solution approach is abandoned, the adjacent object channels o_{k+j} are not available. However, the adjacent images i_{k+j} are available. From equation (8.4) each image contains the corresponding object channel plus a sum of defocused adjacent object channels. Furthermore ignore the effect of the in-focus psf, and recognize that both the recorded image j_{+1} and image j_{-1} contain the out-of-focus contributions from the entire stack. In the positive direction, blurring image j_{+1} by one step of defocus provides a good approximation to the out-of-focus contributions that contaminate i_j . Combining this with a similar defocus in the negative direction:

$$o_j \approx i_j - c(i_{j-1} * h_{-1} + i_{j+1} * h_1) \quad (8.6)$$

where h_{-1} and h_{+1} are psfs that approximate the blurring due to defocus by one step in either direction ($-\Delta z$ and $+\Delta z$), and c is an adjustable constant ($c=0.45$ was found to be appropriate). This suggests that the defocused structures can be partially removed by subtracting images from adjacent planes that have been convolved with the appropriate defocus psf.

The nearest neighbor algorithm of equation (8.6) was implemented in *Mathematica* and applied it to twenty 2D spectral images of the Mercury doublet. The code is shown in Figure 8.1. The resulting reconstructed objects are shown along side the recorded images in Figure 8.2. This technique significantly reduced the image blurring and greatly improved the spectral resolution. The original and reconstructed spectral radiance curves of a pixel are in Figure 8.3. The dip between 577nm and 579nm was increased from 20% in (a) to 55% in (b). Additionally, since the psf is non-symmetric around focus, the recorded data had an incorrect higher value at 579 nm. The use of separate psfs for opposite defocus steps $\Delta z = +1$ and -1 reconstructed the equal intensities of each line. The best results were obtained with the section 3.4.2 experimentally measured psf images, one from each side of the infocus plane, for h_{-1} and h_{+1} .

The nearest neighbor algorithm is particularly useful when one specific spectral image is needed. It is very fast and requires little memory. Computations could be done using generally available image processing hardware. Thus, it should be possible to do the all of the required calculations in essentially real time. While one cannot expect this technique to recover the object function exactly, it does promise to improve images and spectral resolution at reasonable expense.

```

For[z=1, z<=20, z++,
  IMAGE[[z]]=cfft[image[[z]]];]

For[i=1, i<=32, i++,
  For[j=1, j<=32, j++,

    IMAGEP1[[1,i,j]]=IMAGE[[1,i,j]]OTF1[[i,j]];
    IMAGEP1[[2,i,j]]=IMAGE[[2,i,j]]OTF1[[i,j]];
    IMAGEP1[[3,i,j]]=IMAGE[[3,i,j]]OTF1[[i,j]];
    .
    .
    IMAGEP1[[20,i,j]]=IMAGE[[20,i,j]]OTF1[[i,j]];]

For[i=1, i<=32, i++,
  For[j=1, j<=32, j++,
    IMAGEN1[[1,i,j]]=IMAGE[[1,i,j]]OTFn1[[i,j]];
    IMAGEN1[[2,i,j]]=IMAGE[[2,i,j]]OTFn1[[i,j]];
    IMAGEN1[[3,i,j]]=IMAGE[[3,i,j]]OTFn1[[i,j]];
    .
    .
    IMAGEN1[[20,i,j]]=IMAGE[[20,i,j]]OTFn1[[i,j]];]

For[z=1, z<=20, z++,
  imagen1[[z]]=Abs[cinfft[IMAGEN1[[z]]]];
  imagep1[[z]]=Abs[cinfft[IMAGEP1[[z]]]];]

For[z=2, z<=19, z++,
  estimate[[z]]=image[[z]] - n * (imagen1[[z-1]]+imagep1[[z+1]]);]

estimate[[1]]=image[[1]] - 2n * imagep1[[1+1]];
estimate[[20]]=image[[20]] - 2n * imagen1[[20-1]];

```

Figure 8.1: *Mathematica* implementation of the Nearest Neighbor algorithm for 20 images.

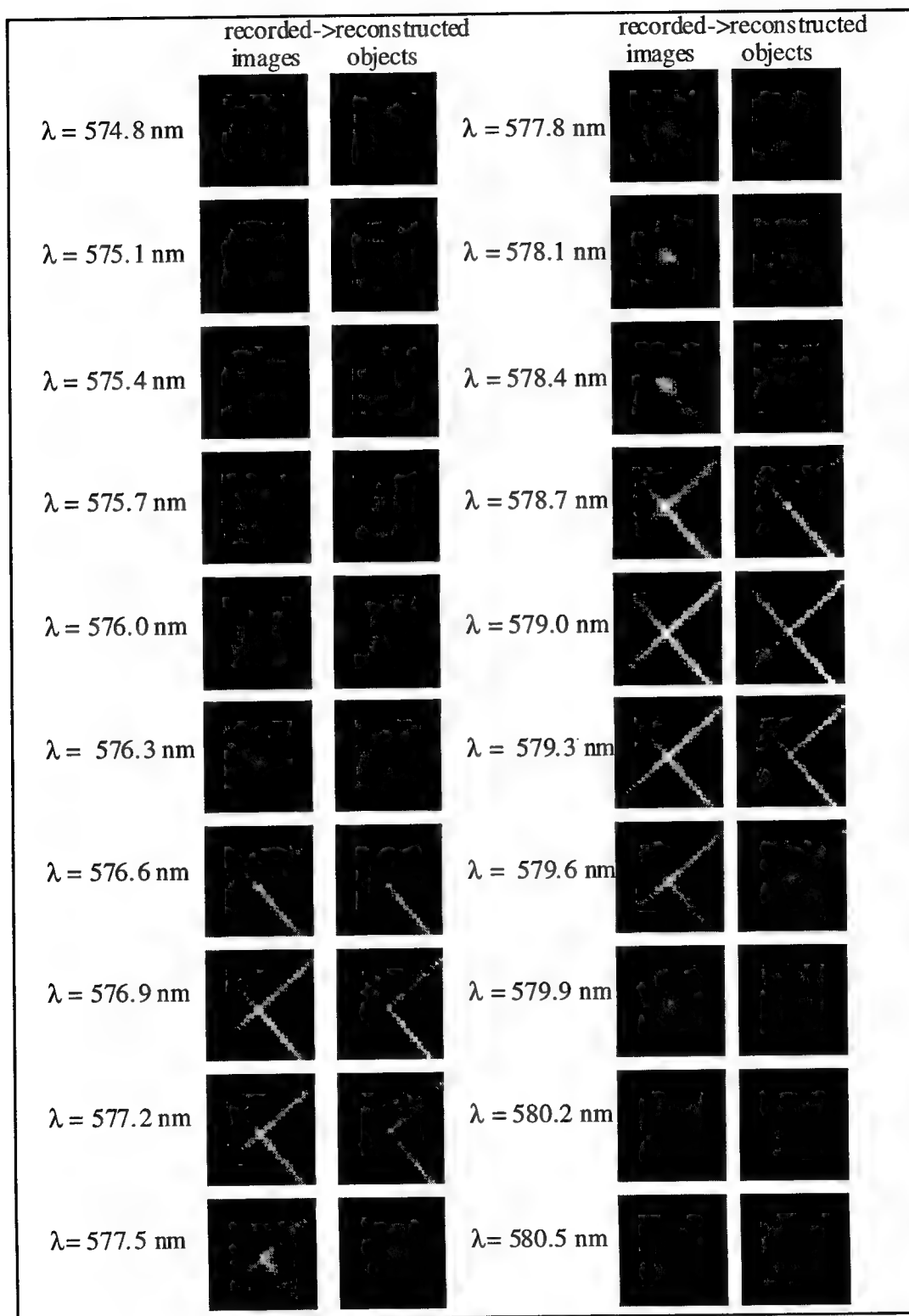


Figure 8.2: Recorded Mercury images and corresponding restored objects with Nearest Neighbor technique.

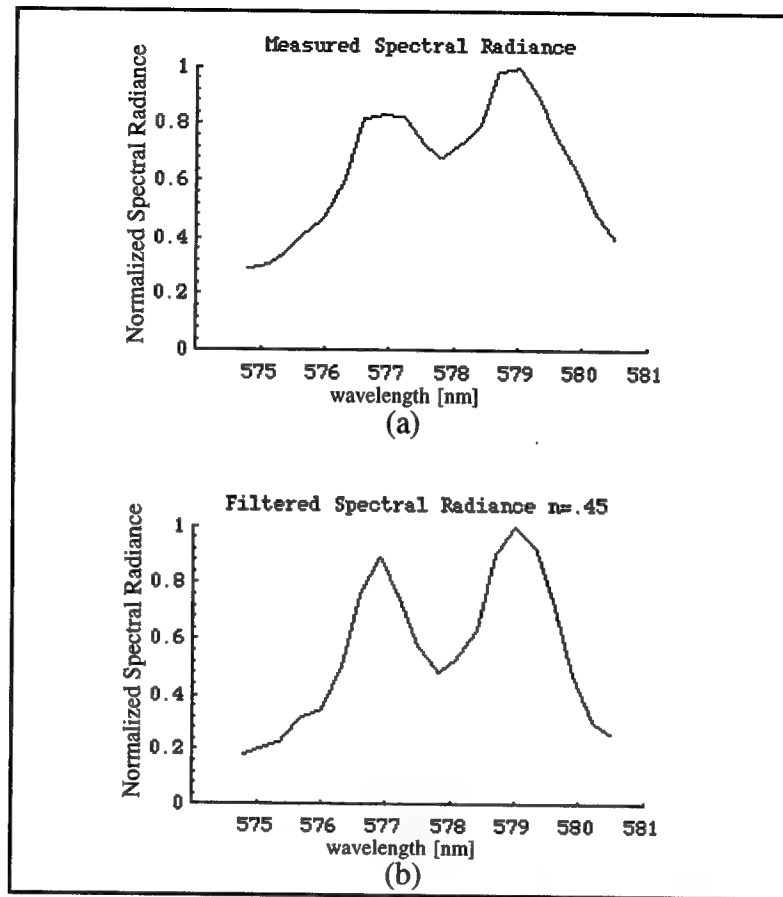


Figure 8.3: Restoration of Mercury spectral radiance curve with Nearest Neighbor technique. (a) the recorded spectra, and the reconstructed spectra with (b) $n=0.45$.

The Nearest Neighbor technique worked for the above application; however, it is important to recognize that the doublet X target has only a few high spatial and spectral frequencies. The computer simulation of section 6.2 predicts that this target would create little blurring, but as the target size increases and the emission broadens the blurring becomes stronger and the reconstruction more challenging. It becomes important to choose an algorithm which takes into account the influence of the whole image cube, not just the adjacent slices, such as Inverse Filtering.

8.3 Inverse Filtering

A more accurate approach to remove the out-of-focus information requires that the full contributions of all of the observed data be utilized. The most direct way to utilize the entire image cube is to perform the inverse filter operations presented in section 4.2 and

4.3.
$$\mathbf{O} = \mathbf{H}^{-1}\mathbf{I}$$

Starting with the object, image and point-spread function three-dimensional data cubes, recall equation 4.11:

$$i(x, y, z) = h(x, y, z) *** o(x, y, z)$$

A technique used in representing multi-dimensional data sets is lexicographical ordering. Each three-dimensional matrix, such as $o(x, y, z)$, can be converted to an $N^3 \times 1$ column vector by using a stacking operator [Hunt 1977]. Applying lexicographical ordering to $32 \times 32 \times 32$ data cubes forms vectors with 32768 elements each, leaving a one dimensional convolution:

$$i(v) = h(v) * o(v) \quad (8.7)$$

Taking the Fourier transform of each vector:

$$I(\psi) = H(\psi)O(\psi) \quad (8.8)$$

The object's Fourier spectrum vector $O(\psi)$ can be computer from:

$$O(\psi) = \frac{I(\psi)}{H(\psi)} \quad (8.9)$$

An inverse Fourier transform is applied to $O(\psi)$ to reconstruct $o(v)$, which can be repartitioned in three dimension.

The three-dimensional matrix calculation has been reduced to a scalar division. Notice that consideration must be given to the possibility of dividing by zero. Another

concern is that the regions in the image spectrum where the OTF values are very small correspond to frequencies that are mainly noise. Dividing these frequencies by the low values of the OTF would cause an over amplification of noise. Two methods are generally used to deal with this: apodization and applying a regularized inverse filter.

8.3.1 Apodization Inverse Filter

Apodization is a technique to deal with dividing the image spectrum with the lowest values of the OTF, by simply setting a maximum for the value of $\frac{1}{H(\psi)}$ equal to a constant,

a . Values greater than a are set to zero [Erhardt 1985].

$$\frac{1}{H(\psi)} = \begin{cases} \frac{1}{H(\psi)} & \text{if } \leq a \\ 0 & \text{if } > a \end{cases} \quad (8.10)$$

An apodized inverse filter was implemented in *Mathematica*. The code is presented in Figure 8.4. The lexicographical ordering function is performed by the command **Flatten[]** and was used throughout the image processing, allowing the data cubes to be "unwrapped". The function **Partition[]** is used after the processing has been performed to regenerate the three-dimensional organization of the data cube. Erhardt used this approach with a theoretical OTF. However, the differences between experimental and theoretical OTFs are significant; hence better results were obtained using the experimental OTF of Figure 3.17. Figure 8.5 contains plots of lexicographical vector versions of the measured 3D psf and OTF. Figure 8.6 shows the results obtained from applying the apodized inverse filter to the challenging iris target and its computer generated 16 pixel counterpart.

```

For[p=1, p<=5,p++,
For[m=1., m<=32768, m++,
If[Abs[1./FLATOTF[[m]]]<=(20*(p-1)+10),INOTF[[p,m]]=1./FLATOTF[[m]],
INOTF[[p,m]]=0.;];];

FLATMIMAGE=cflatfft[Flatten[timage3D]];
FLATMIMAGE=cflatfft[Flatten[iris]];

For[m=1., m<=5, m++,
OBJ=FLATMIMAGE*INOTF[[m]];
obj=Abs[cflatinfft[OBJ]];
parimagemono=Partition[obj,1024];

For[k=1., k<=32, k++,
obj3D[[m,k]]=Partition[parimagemono[[k]],32];
tobj3D[[m,k]]=Transpose[RotateRight[Transpose[RotateRight[obj3D[[m,k]],16],16]]];];

For[z=1, z<=32, z++,
trans[[z]]=Transpose[tobj3D[[m,z]]];
heightrecon[[m,z]]=trans[[z,16]];
zrrecon[[m,z]]=tobj3D[[m,z,16]]];];
heightrecon[[m]]=Transpose[heightrecon[[m]]];
zrrecon[[m]]=Transpose[zrrecon[[m]]];];

```

Figure 8.4: The Mathematica code for inverse reconstruction with apodization.

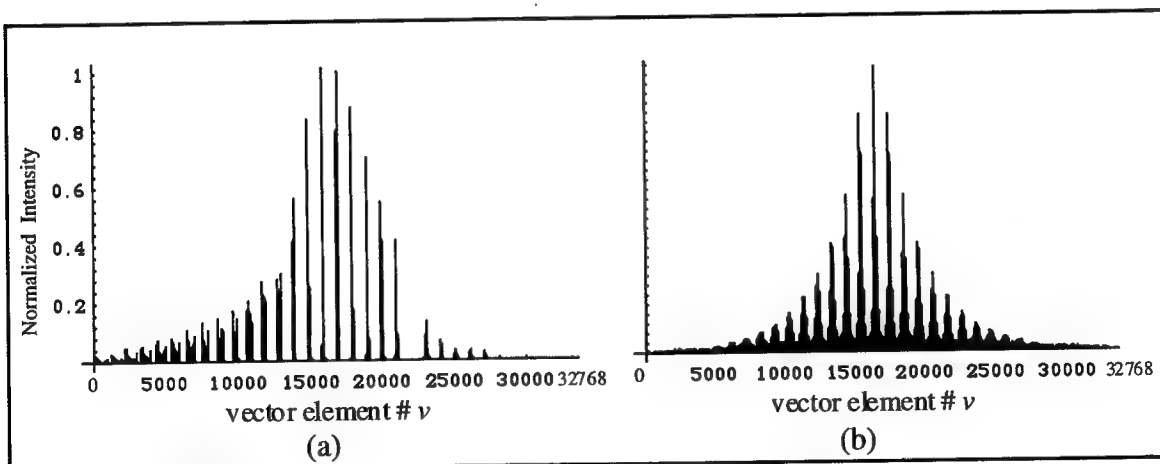


Figure 8.5: List Plot of the flattened (a) psf. (b) OTF.

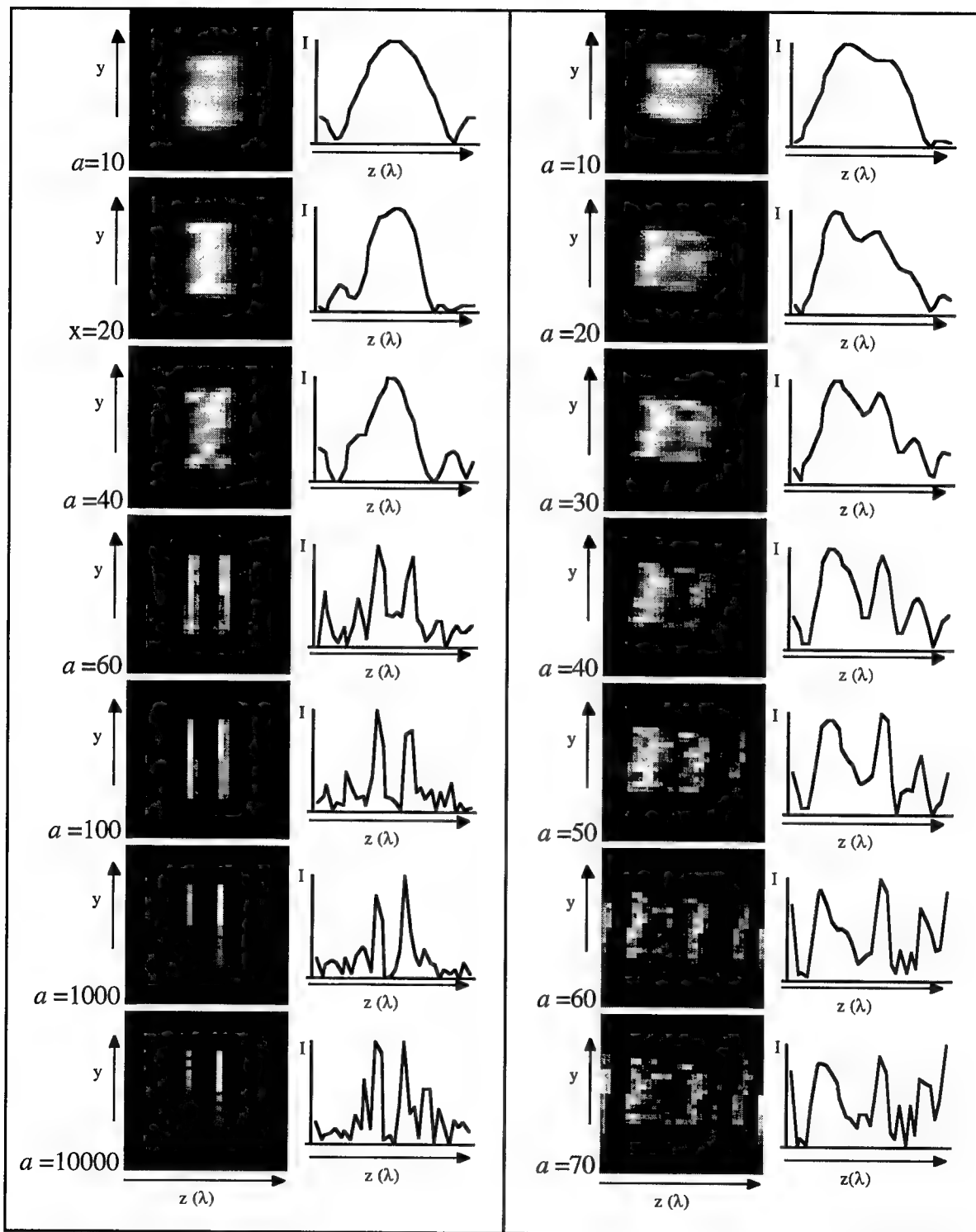


Figure 8.6: Object results from apodization reconstruction with CG images (left column) and recorded iris images (right column).

8.3.2 Regularized Inverse Filter

In inverse filtering situations, it is standard practice to use a regularized inverse filter to minimize the effects of noise that can dominate at high spatial frequencies [Sezan 1992]. The form of the regularized inverse filter for the scalar equation (8.9) is:

$$O(\psi) = \left(\frac{H(\psi)^*}{H(\psi)^* H(\psi) + \alpha} \right) I(\psi) \quad (8.11)$$

where α is a constant whose choice is based on the signal-to-noise ratio of the data and should be in the range of 0.001 to 0.1. In the experimental reconstruction a value of $\alpha=0.005$ was found to be appropriate. Notice that like the apodization technique, the α in the denominator of equation (8.11) essentially sets a threshold maximum of $\frac{1}{H(\psi)}$ to deal with the low values of the OTF.

A regularized inverse filter can also be applied in the three-dimensional inverse equation:

$$O(\xi, \psi, \zeta) = \mathbf{H}(\xi, \psi, \zeta)^{-1} \mathbf{I}(\xi, \psi, \zeta) \quad (8.12)$$

$$O(\xi, \psi, \zeta) = \left[\mathbf{H}(\xi, \psi, \zeta)^* \mathbf{H}(\xi, \psi, \zeta) + \alpha \right]^{-1} \mathbf{H}(\xi, \psi, \zeta)^* \mathbf{I}(\xi, \psi, \zeta) \quad (8.13)$$

however this requires taking the inverse of the $[\mathbf{H}^* \mathbf{H} + \alpha]$ matrix, a task which can be difficult if the data is singular. Further discussion can be found below in section 8.3.3.

The scalar regularized inverse filter of equation (8.11) was implemented in *Mathematica* and applied it to the 32x32x32 recorded image cube of the same Mercury X target. The code is printed in Figure 8.7.

```

flatimage=Flatten[image];
flatpsf=Flatten[psf];

FLATIMAGE=cfft[flatimage];
FLATOTF=cfft[psf];

a=.005;
FLATOBJ=FLATIMAGE*Conjugate[FLATOTF]/((FLATOTF*Conjugate[FLATOTF])+a);

flatobj=Abs[cinfft[FLATOBJ]];

parobj=Partition[flatobj,1024];

3Dobj=Table[0.,{z,32},{x,32},{y,32}];
For[j=1.,j<=32,j++,
3Dobj[[j]]=Partition[parobj[[j]],32];];

t3Dobj=Table[0.,{z,32},{x,32},{y,32}];
For[j=1.,j<=32,j++,
t3Dobj[[j]]=Transpose[RotateRight[Transpose[RotateRight[3Dobj[[j]],16],16]]];];

```

Figure 8.7: Mathematica code for the regularized inverse filter.

The results from applying the regularized inverse filter to the Mercury X target are presented in Figure 8.8. Pictured in Figure 8.8(a) when $\alpha=0$ the regularized inverse filter defaults to standard inverse filter of equation (8.9). The results show that the reconstruction is ineffective because of the noise. The addition of the regularized inverse filter noise term, α , significantly improved the image quality. The image sets in Figure 8.8 (b), (c) and (d) show the reconstructed object sets with α equal to 0.1, 0.01 and 0.005 respectively. A large α such as 0.1 in Figure 8.8 (b) is similar to a low pass filter. Setting α to a smaller number increases the band pass for better reconstruction but also increases the possibility of noise. Figure 8.9 shows the normalized spectral radiance of one pixel before and after processing.

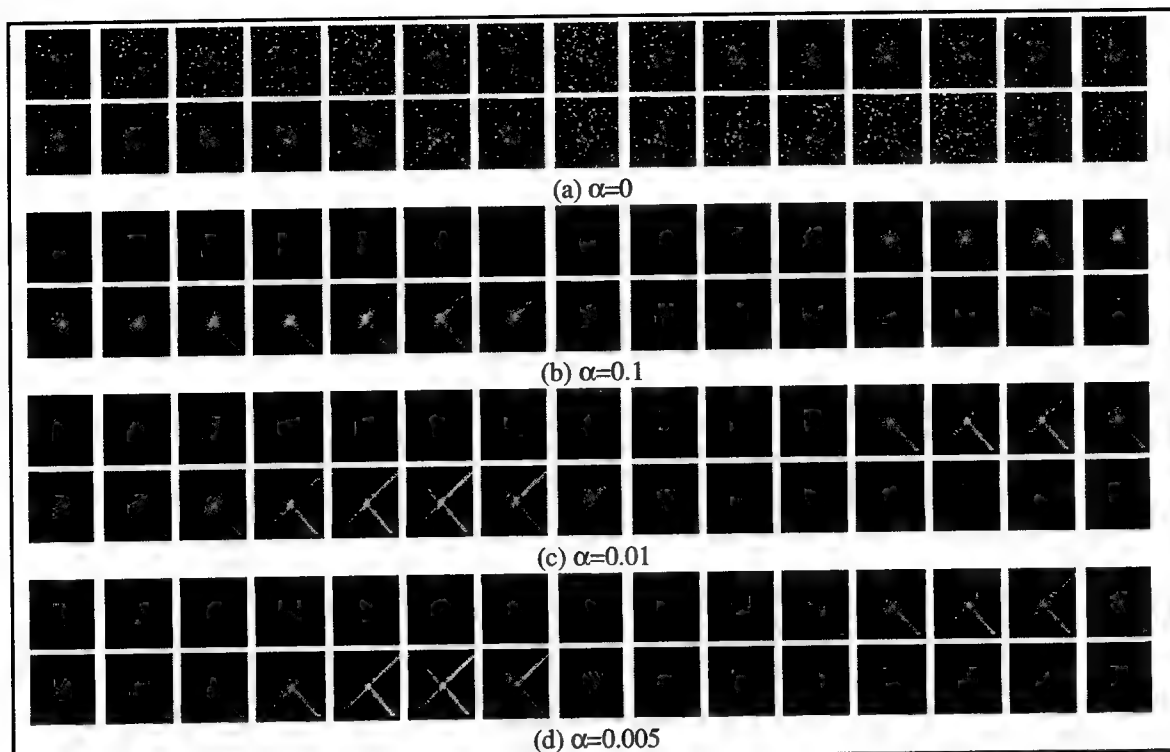


Figure 8.8: Resulting object sets after regularized inverse reconstruction with various α .

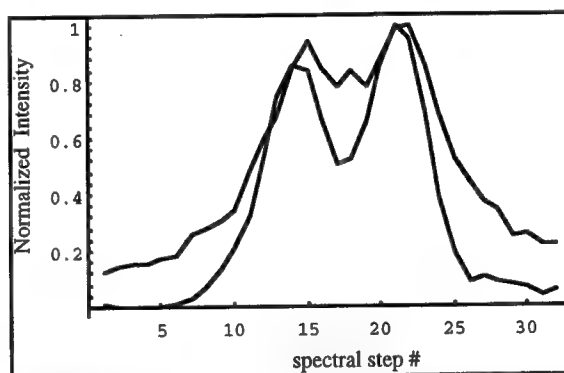


Figure 8.9: Spectral Radiance of pixel 16,16 before and after (bold) regularized inverse reconstruction with $\alpha = 0.005$.

Continuing the exploration of the spectral/spatial relationship this algorithm was applied to both the computer generated and experimentally measured increasing aperture doublet targets from Figure 6.7. The results are pictured in Figures 8.10, 8.11 and 8.12. As before, each 2D image is a $z(\lambda)$ vs. y cross-section of a 3D data cube with a corresponding spectral curve plotted below it.

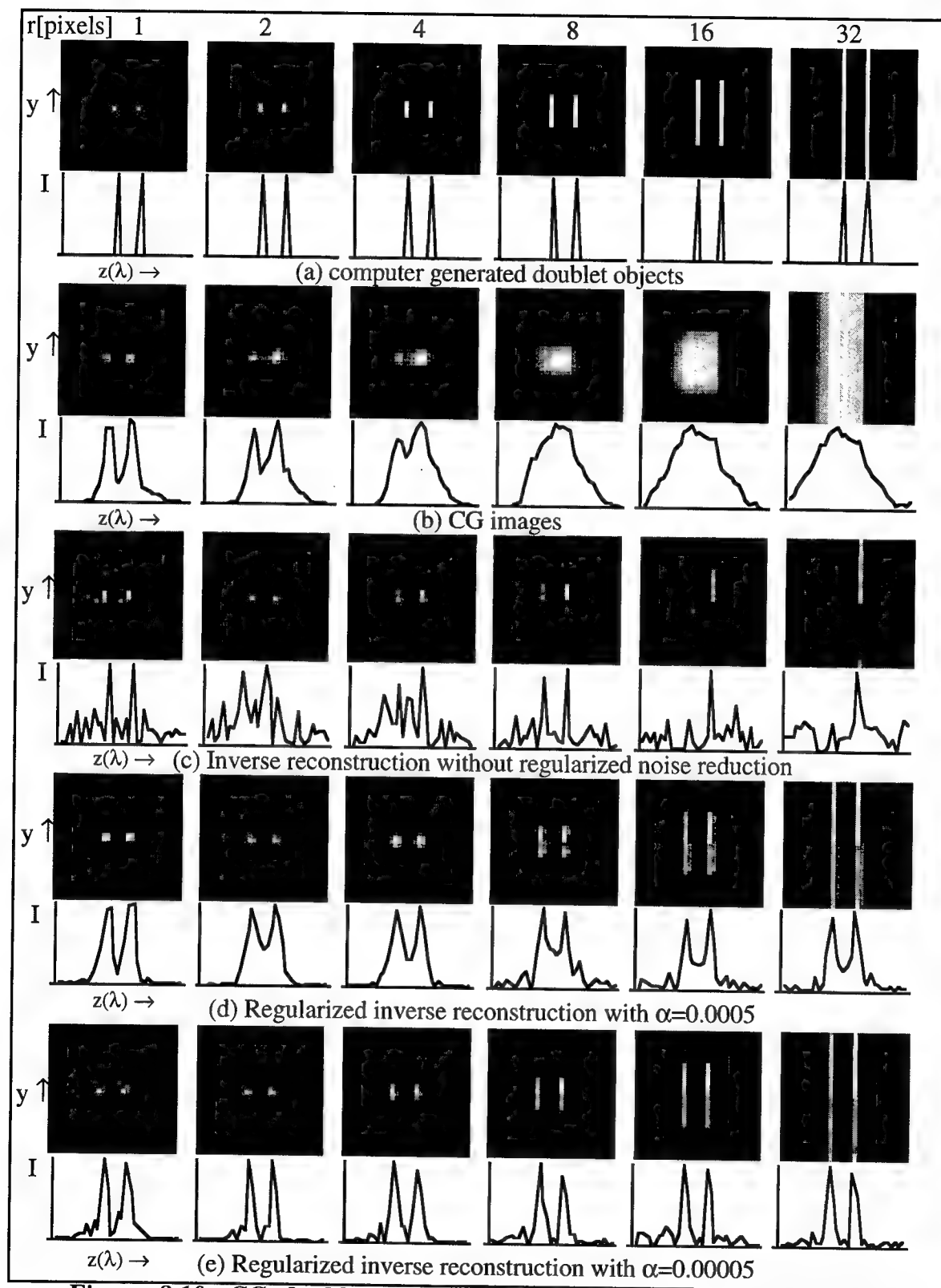


Figure 8.10: CG doublet objects, images and reconstructed objects

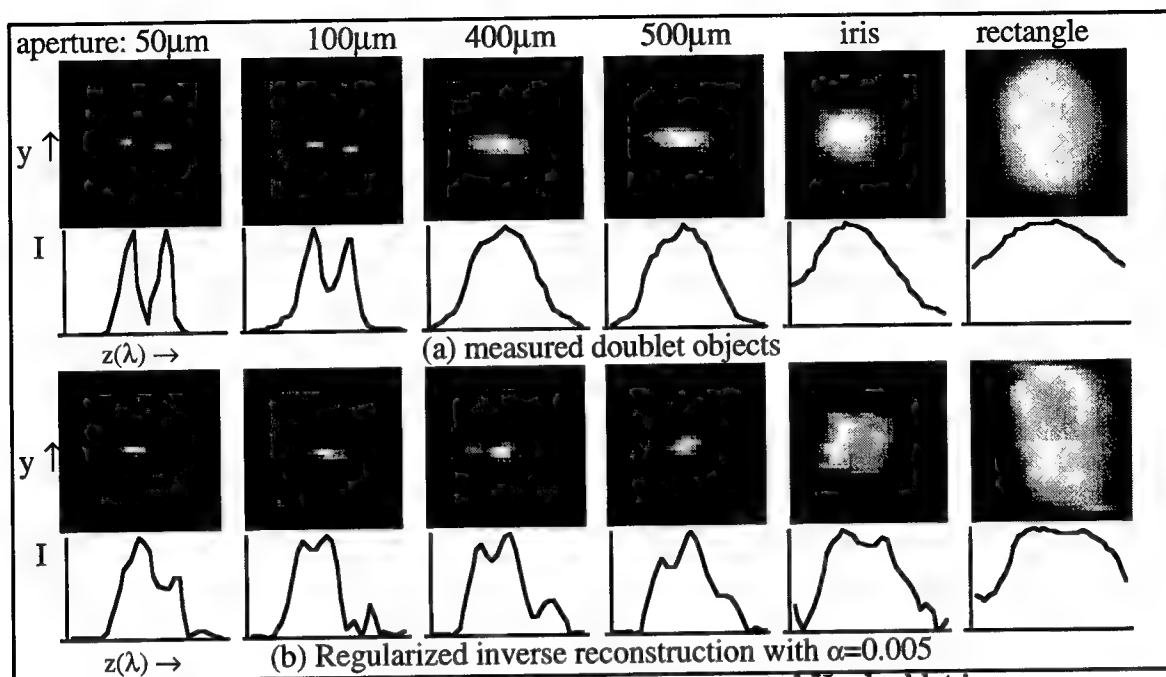


Figure 8.11: Measured and regularized inverse reconstructed Hg doublet images.

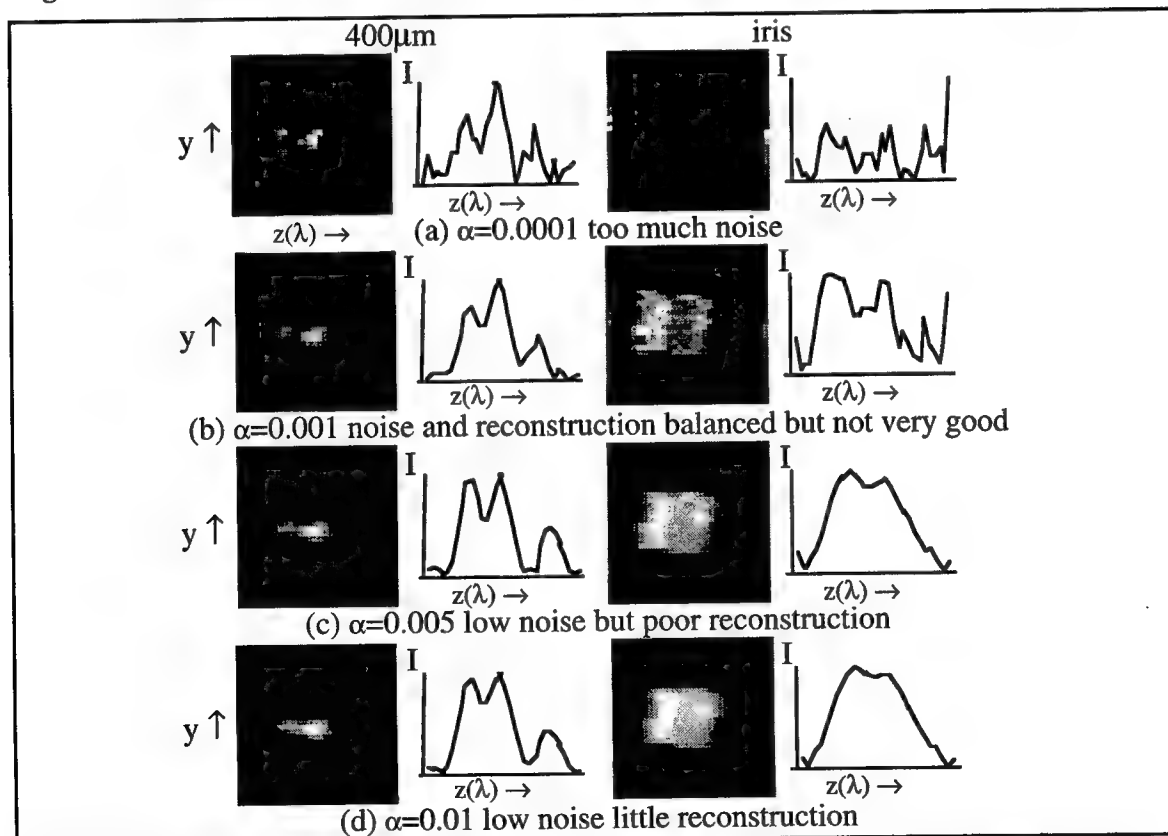


Figure 8.12: Results of regularized inverse filter on measured 400 μ m and iris images.

This lexicographic regularized inverse filter worked very well on the measured X images of Figure 8.8 and the CG data of Figure 8.7. Even the long 32 pixel aperture of the right hand column is reconstructed. However, it was ineffective on the experimentally measured image cubes of the increasing apertures shown in Figures 8.11 and 8.12. Notice the unpredicted peaks at the edges of the spectral curves caused by both the apodization in Figure 8.6, and regularized inverse filter applied to measured image cubes. These peaks are artifacts of an invalid assumption during lexicographical ordering that the psf is shift invariant and circular. The limited success that has been achieved is due to the fact that the targets have been spatially and spectrally located in the center of our 3D data cube, similar to being padded with zeros. However, as our target increased, i.e. the iris aperture, the circular approximation is seen as the psf wrapping around to the other side of our data cube. This problem is addressed by not making the circular assumption, by explicitly performing the z dimension matrix multiplication and implementing an SVD algorithm which also addresses probable difficulties such as a non-square data cube (MxNxN) and singular OTF matrices.

8.3.3 Singular Value Decomposition Inverse Filter

DOIS records a series of 2D spectral images, i_1, i_2, \dots, i_n . These are saved as a 3D image cube **image**[[x,y,z]]. The following expands equation (8.2) for a $j=4$, four color target. It describes each spectral image, $i_j(x,y)$ as the superposition of each spectral object, $o_k(x,y)$ convolved with a defocused point spread function, $h_{jk}(x,y)$ [Mooney 1995].

$$\begin{aligned}
 i_1(x,y) &= h_{11}(x,y) ** o_1(x,y) + h_{12}(x,y) ** o_2(x,y) + h_{13}(x,y) ** o_3(x,y) + h_{14}(x,y) ** o_4(x,y) \\
 i_2(x,y) &= h_{21}(x,y) ** o_1(x,y) + h_{22}(x,y) ** o_2(x,y) + h_{23}(x,y) ** o_3(x,y) + h_{24}(x,y) ** o_4(x,y) \\
 i_3(x,y) &= h_{31}(x,y) ** o_1(x,y) + h_{32}(x,y) ** o_2(x,y) + h_{33}(x,y) ** o_3(x,y) + h_{34}(x,y) ** o_4(x,y) \\
 i_4(x,y) &= h_{41}(x,y) ** o_1(x,y) + h_{42}(x,y) ** o_2(x,y) + h_{43}(x,y) ** o_3(x,y) + h_{44}(x,y) ** o_4(x,y)
 \end{aligned}
 \tag{8.14}$$

Following the theory of section 4.2 for simulation and reconstruction, 2D Fourier transforms are applied:

$$\begin{aligned}
I_1(\xi, \zeta) &= H_{11}(\xi, \zeta)O_1(\xi, \zeta) + H_{12}(\xi, \zeta)O_2(\xi, \zeta) + H_{13}(\xi, \zeta)O_3(\xi, \zeta) + H_{14}(\xi, \zeta)O_4(\xi, \zeta) \\
I_2(\xi, \zeta) &= H_{21}(\xi, \zeta)O_1(\xi, \zeta) + H_{22}(\xi, \zeta)O_2(\xi, \zeta) + H_{23}(\xi, \zeta)O_3(\xi, \zeta) + H_{24}(\xi, \zeta)O_4(\xi, \zeta) \\
I_3(\xi, \zeta) &= H_{31}(\xi, \zeta)O_1(\xi, \zeta) + H_{32}(\xi, \zeta)O_2(\xi, \zeta) + H_{33}(\xi, \zeta)O_3(\xi, \zeta) + H_{34}(\xi, \zeta)O_4(\xi, \zeta) \\
I_4(\xi, \zeta) &= H_{41}(\xi, \zeta)O_1(\xi, \zeta) + H_{42}(\xi, \zeta)O_2(\xi, \zeta) + H_{43}(\xi, \zeta)O_3(\xi, \zeta) + H_{44}(\xi, \zeta)O_4(\xi, \zeta)
\end{aligned} \tag{8.15}$$

Rewritten in matrix form:

$$\begin{bmatrix} I_1(\xi, \zeta) \\ I_2(\xi, \zeta) \\ I_3(\xi, \zeta) \\ I_4(\xi, \zeta) \end{bmatrix} = \begin{bmatrix} H_{11}(\xi, \zeta) & H_{12}(\xi, \zeta) & H_{13}(\xi, \zeta) & H_{14}(\xi, \zeta) \\ H_{21}(\xi, \zeta) & H_{22}(\xi, \zeta) & H_{23}(\xi, \zeta) & H_{24}(\xi, \zeta) \\ H_{31}(\xi, \zeta) & H_{32}(\xi, \zeta) & H_{33}(\xi, \zeta) & H_{34}(\xi, \zeta) \\ H_{41}(\xi, \zeta) & H_{42}(\xi, \zeta) & H_{43}(\xi, \zeta) & H_{44}(\xi, \zeta) \end{bmatrix} \begin{bmatrix} O_1(\xi, \zeta) \\ O_2(\xi, \zeta) \\ O_3(\xi, \zeta) \\ O_4(\xi, \zeta) \end{bmatrix} \tag{8.16}$$

This equation can be evaluated for each spatial frequency (ξ, ζ) . Lets take a closer look at the **H** matrix :

$$\mathbf{H} = \begin{bmatrix} H_{11}(\xi, \zeta) & H_{12}(\xi, \zeta) & H_{13}(\xi, \zeta) & H_{14}(\xi, \zeta) \\ H_{21}(\xi, \zeta) & H_{22}(\xi, \zeta) & H_{23}(\xi, \zeta) & H_{24}(\xi, \zeta) \\ H_{31}(\xi, \zeta) & H_{32}(\xi, \zeta) & H_{33}(\xi, \zeta) & H_{34}(\xi, \zeta) \\ H_{41}(\xi, \zeta) & H_{42}(\xi, \zeta) & H_{43}(\xi, \zeta) & H_{44}(\xi, \zeta) \end{bmatrix} \tag{8.17}$$

In Chapter 4 great lengths were taken to show that the point spread function is shift invariant (SIV). Applied here, it means that each H_{jk} can be expressed by the Fourier transform of a point spread function with an appropriate amount of defocus, $H_{\Delta z}$, where $\Delta z = i - j$, i.e. H_0 is infocus, H_1 is 1 step away from focus and H_{-1} is 1 step in the other direction.

$$\mathbf{H} = \begin{bmatrix} H_0(\xi, \zeta) & H_1(\xi, \zeta) & H_2(\xi, \zeta) & H_3(\xi, \zeta) \\ H_{-1}(\xi, \zeta) & H_0(\xi, \zeta) & H_1(\xi, \zeta) & H_2(\xi, \zeta) \\ H_{-2}(\xi, \zeta) & H_{-1}(\xi, \zeta) & H_0(\xi, \zeta) & H_1(\xi, \zeta) \\ H_{-3}(\xi, \zeta) & H_{-2}(\xi, \zeta) & H_{-1}(\xi, \zeta) & H_0(\xi, \zeta) \end{bmatrix} \tag{8.18}$$

This is a block Toeplitz matrix formed from Fourier transforming images of point source at various amounts of defocus. Typically when considering a large number of

spectral channels it will become a sparse band diagonal matrix since the $H_{\Delta z}$ approaches zero at significant amounts of defocus.

The task is to invert this \mathbf{H} matrix, however it can have various problems which cause it to be singular and difficult to invert [Mooney 1995]. There can fail to be a unique solution if one or more of the N equations is a linear combination of the others, a condition called row degeneracy. Or if all equations contain certain variables in the exact same linear combination, inversion can fail due to column degeneracy. A set of equations that is degenerate is called singular. Singular value decomposition is a technique to solve for a solution to the inverse matrix with singular matrixes and in fact diagnose the singularities. This is the method of choice for solving most linear least squares problems [Press 1988].

The SVD method is based on the linear algebra theorem that any $M \times N$ matrix \mathbf{H} whose number of rows M is greater than or equal to its number of columns N , can be written as the product of an $M \times N$ column-orthogonal matrix \mathbf{U} , an $N \times N$ diagonal matrix \mathbf{W} with positive or zero elements, and the transpose of an $N \times N$ orthogonal matrix \mathbf{V} .

$$\begin{bmatrix} H \end{bmatrix} = \begin{bmatrix} U \end{bmatrix} \begin{bmatrix} w_{11} & & \\ & \dots & \\ & & w_{nn} \end{bmatrix} \begin{bmatrix} V^T \end{bmatrix} \quad (8.19)$$

The matrices \mathbf{U} and \mathbf{V} are each orthogonal in the sense that their columns are orthonormal, where:

$$\begin{bmatrix} U^T \end{bmatrix} \begin{bmatrix} U \end{bmatrix} = \begin{bmatrix} V^T \end{bmatrix} \begin{bmatrix} V \end{bmatrix} = \begin{bmatrix} 1 \end{bmatrix} \quad (8.20)$$

Since \mathbf{V} is square, it is also row-orthonormal, $\mathbf{V} \cdot \mathbf{V}^T = \mathbf{I}$. The inverse of the diagonal matrix \mathbf{W} is easily determined by replacing the diagonal elements with $1/w$.

$$\begin{bmatrix} 1/w_{11} & & \\ & \dots & \\ & & 1/w_{nn} \end{bmatrix} \begin{bmatrix} w_{11} & & \\ & \dots & \\ & & w_{nn} \end{bmatrix} = \begin{bmatrix} 1 & & \\ & \dots & \\ & & 1 \end{bmatrix} \quad (8.21)$$

The decomposition and determination of \mathbf{U} , \mathbf{W} , and \mathbf{V}^T is accomplished by a standard routine found in Numerical Recipes. In *Mathematica* the function **SingularValues[H]** outputs three matrices \mathbf{U} , the elements of \mathbf{W} and \mathbf{V} . The inverse of \mathbf{H} is found from:

$$\mathbf{H}^{-1} = \mathbf{V} \cdot \left[\text{diag} \left(\frac{1}{w_j} \right) \right] \cdot \mathbf{U}^T \quad (8.22)$$

The elements of \mathbf{W} are called the singular values of the system. They help visualize the missing cone of our data, Figure 8.19. The noise can be suppressed by adding a regularization filter to the w_{ii} values:

$$\frac{1}{w} = \frac{w}{w^2 + \alpha^2} \quad (8.23)$$

Substituting this SVD into the inverse reconstruction equation:

$$\begin{aligned} \mathbf{O}(\xi, \zeta) &= \mathbf{H}(\xi, \zeta)^{-1} \mathbf{I}(\xi, \zeta) \\ \mathbf{O}(\xi, \zeta) &= \mathbf{V}(\xi, \zeta) \cdot \left[\text{diag} \left(\frac{w(\xi, \zeta)}{w^2(\xi, \zeta) + \alpha^2} \right) \right] \cdot \mathbf{U}^T(\xi, \zeta) \cdot \mathbf{I}(\xi, \zeta) \end{aligned} \quad (8.24)$$

This SVD Inverse filtering algorithm was implemented in *Mathematica*. The first step was to form the OTF matrix. The best results were obtained from using a combined point spread function which is an average of the experimentally measured and theoretical psfs found in Figure 8.13. The measured psf provides information about the influence of aberrations from our DOE, while the theoretical psf, calculated from the geometric cone,

provides the very small values which fall below the detectable range of the detector and would mistakenly be set to zero.

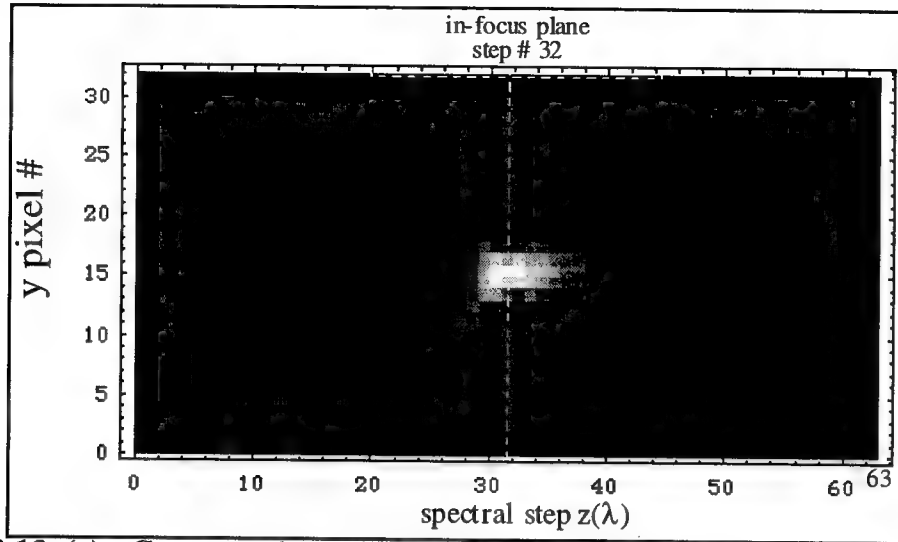


Figure 8.13 (c): Cross-section of the 3D combination psf used in SVD object reconstruction (contrast enhanced to show detail).

Looking again at equation (8.18) one might notice that it takes seven values of $H_{\Delta z}(\xi, \zeta)$ to form the four $z(\lambda)$ rows in the **H** matrix. To reconstruct **OTF** with 32 $z(\lambda)$ rows, values from 63 $z(\lambda)$ planes are required as shown in Figure 8.13. This provides images of a point source at focus (plane number 32) and 31 defocus steps on either side of focus. Since it has been established that the psf is shift invariant, a "basis" OTF matrix **P** is formed from taking the 2D Fourier transform of the image at each step of defocus with the procedure listed in Figure 8.14.

<pre>For[z=1, z<=63, z++, P[[z]]=cfft[combinedpsf[[z]]];]; P=P/Max[Abs[P]];</pre>	<p>This code takes the Fourier Transform of the (32x,32y) images at 63 steps of defocus, z, in the combined psf of Figure 8.13, then normalizes the results to form the normalized OTF, $P[[\Delta z, \xi, \zeta]]$</p>
---	--

Figure 8.14: Mathematica code to calculate the "basis" OTF, $P[[\Delta z, \xi, \zeta]]$.

The **OTF** matrix is formed by substituting the appropriate defocus data $P[[\Delta z, \xi, \zeta]]$. **OTF** is a four-dimensional matrix, $N \times N$ (32x32) for each spatial frequency

(ξ, ζ) , shown in Figure 8.15. The values are complex, $\text{Re} + i\text{Im}$, yet the standard SVD code is written for real elements. However, SVD can handle non square matrices, $M \times N$, so our $N \times N$ complex matrix is converted into a $2N \times N$ real matrix where the first N rows are the real values and the remainder are the imaginary. It is this matrix which will be inverted with the SVD routine and then rewritten as an $N \times N$ complex inverse matrix using the conversion matrix **inim**, formed in Figure 8.16.

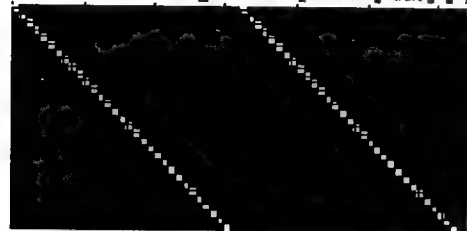
```
OTF=Table[0.,{i,32},{j,32},{ξ,32},{ζ,32}]; "forms a 4D OTF matrix"
SessionTime[]
For[ξ=1, ξ <=32, ξ ++, "puts the proper values into the 4D OTF
For[ζ=1, ζ <=32, ζ ++, matrix for each spatial frequency (ξ,ζ)"
OTF[[ξ,ζ]]=
{P[[32,ξ,ζ]], P[[31,ξ,ζ]], P[[30,ξ,ζ]], P[[29,ξ,ζ]], P[[... ,ξ,ζ]], P[[1,ξ,ζ]]}
{P[[33,ξ,ζ]], P[[32,ξ,ζ]], P[[31,ξ,ζ]], P[[30,ξ,ζ]], P[[... ,ξ,ζ]], P[[2,ξ,ζ]]}
{P[[34,ξ,ζ]], P[[33,ξ,ζ]], P[[32,ξ,ζ]], P[[31,ξ,ζ]], P[[... ,ξ,ζ]], P[[3,ξ,ζ]]}
{P[[35,ξ,ζ]], P[[34,ξ,ζ]], P[[33,ξ,ζ]], P[[32,ξ,ζ]], P[[... ,ξ,ζ]], P[[4,ξ,ζ]]}
{P[[36,ξ,ζ]], P[[35,ξ,ζ]], P[[34,ξ,ζ]], P[[33,ξ,ζ]], P[[... ,ξ,ζ]], P[[5,ξ,ζ]]}
{P[[37,ξ,ζ]], P[[36,ξ,ζ]], P[[35,ξ,ζ]], P[[34,ξ,ζ]], P[[... ,ξ,ζ]], P[[6,ξ,ζ]]}
{P[[38,ξ,ζ]], P[[37,ξ,ζ]], P[[36,ξ,ζ]], P[[35,ξ,ζ]], P[[... ,ξ,ζ]], P[[7,ξ,ζ]]}
{P[[39,ξ,ζ]], P[[38,ξ,ζ]], P[[37,ξ,ζ]], P[[36,ξ,ζ]], P[[... ,ξ,ζ]], P[[8,ξ,ζ]]}
{P[[40,ξ,ζ]], P[[39,ξ,ζ]], P[[38,ξ,ζ]], P[[37,ξ,ζ]], P[[... ,ξ,ζ]], P[[9,ξ,ζ]]}
{P[[41,ξ,ζ]], P[[40,ξ,ζ]], P[[39,ξ,ζ]], P[[38,ξ,ζ]], P[[... ,ξ,ζ]], P[[10,ξ,ζ]]}
{P[[42,ξ,ζ]], P[[41,ξ,ζ]], P[[40,ξ,ζ]], P[[39,ξ,ζ]], P[[... ,ξ,ζ]], P[[11,ξ,ζ]]}
{P[[43,ξ,ζ]], P[[42,ξ,ζ]], P[[41,ξ,ζ]], P[[40,ξ,ζ]], P[[... ,ξ,ζ]], P[[12,ξ,ζ]]}
{P[[44,ξ,ζ]], P[[43,ξ,ζ]], P[[42,ξ,ζ]], P[[41,ξ,ζ]], P[[... ,ξ,ζ]], P[[13,ξ,ζ]]}
{P[[45,ξ,ζ]], P[[44,ξ,ζ]], P[[43,ξ,ζ]], P[[42,ξ,ζ]], P[[... ,ξ,ζ]], P[[14,ξ,ζ]]}
{P[[46,ξ,ζ]], P[[45,ξ,ζ]], P[[44,ξ,ζ]], P[[43,ξ,ζ]], P[[... ,ξ,ζ]], P[[15,ξ,ζ]]}
{P[[47,ξ,ζ]], P[[46,ξ,ζ]], P[[45,ξ,ζ]], P[[44,ξ,ζ]], P[[... ,ξ,ζ]], P[[16,ξ,ζ]]}
{P[[48,ξ,ζ]], P[[47,ξ,ζ]], P[[46,ξ,ζ]], P[[45,ξ,ζ]], P[[... ,ξ,ζ]], P[[17,ξ,ζ]]}
{P[[49,ξ,ζ]], P[[48,ξ,ζ]], P[[47,ξ,ζ]], P[[46,ξ,ζ]], P[[... ,ξ,ζ]], P[[18,ξ,ζ]]}
.
.
{P[[61,ξ,ζ]], P[[60,ξ,ζ]], P[[59,ξ,ζ]], P[[58,ξ,ζ]], P[[... ,ξ,ζ]], P[[30,ξ,ζ]]}
{P[[62,ξ,ζ]], P[[61,ξ,ζ]], P[[60,ξ,ζ]], P[[59,ξ,ζ]], P[[... ,ξ,ζ]], P[[31,ξ,ζ]]}
{P[[63,ξ,ζ]], P[[62,ξ,ζ]], P[[61,ξ,ζ]], P[[60,ξ,ζ]], P[[... ,ξ,ζ]], P[[32,ξ,ζ]]}
];];
SessionTime[]
71630.88
73560.42
```

Figure 8.15: *Mathematica* code to form the OTF Matrix.

```

im=Table[0.,{x,32},{y,64}];
realim=IdentityMatrix[32];
For[x=1,x<=32,x++,
For[y=1,y<=32,y++,
im[[x,y]]=realim[[x,y]];
im[[x,y+32]]=I*realim[[x,y]];
];
ListDensityPlot[Abs[im]];

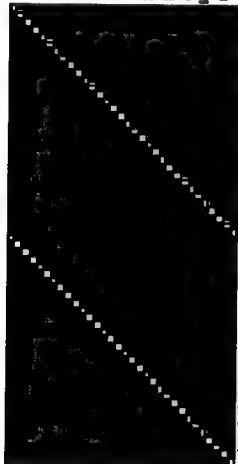
```



```

inim=PseudoInverse[im];
ListDensityPlot[Abs[inim]];

```



The SVD algorithm in *Numerical Recipes* and *Mathematica* only works on real matrices and the OTF matrix has complex numbers. However, it is possible to rewrite the square $N \times N$ complex matrix as a $2N \times N$ matrix, called **ri**, with the real values in the first N rows and the imaginary values in the lower N rows. The SVD is used to decompose and invert the $2N \times N$ **ri** matrix.

The code on the left forms a $2N \times N$ matrix **inim** where the 1st N rows form an Identity matrix and the bottom rows form a diagonal matrix with the complex value i along the diagonal. This matrix can be multiplied by the inverse of **ri** to reorder the inverse matrix into a $N \times N$ complex inverse matrix.

$$\begin{array}{c}
 \left| \begin{array}{c} H \\ \end{array} \right| \\
 \downarrow \\
 \left| \begin{array}{c} \text{Re}[H] \\ \text{Im}[H] \end{array} \right| \\
 \downarrow \text{SVD} \\
 \left| \begin{array}{c} H^{-1} \end{array} \right| = \left| \begin{array}{c} \text{Re}[H^{-1}] \\ \text{Im}[H^{-1}] \end{array} \right| \left| \begin{array}{cc} 1 & 1 \\ i & i \end{array} \right|
 \end{array}$$

Figure 8.16: *Mathematica* code to create **inim** which converts the $N \times N$ Complex matrix into an $2N \times N$ of all Real values.

The code in Figure 8.17 creates the matrix **IMAGE** by taking the Fourier transform of the 2D spectral images at each $z(\lambda)$. As shown, an additional dimension was added to the **IMAGE** matrix, m , where each value of m represents a different target. Since the OTF doesn't change, the algorithm can be applied to many image cubes while having to invert the matrix only once. In fact, once a proper OTF and α value are established, the inverse need only be performed once. It can be stored in memory for future use.

"forms a matrix with Fourier Transforms of 6 measured image cubes to reconstruct 6 object cubes simultaneously"

```
IMAGE=Table[0.,{m,6},{z,32},{x,32},{y,32}];
REIMAGE=Table[0.,{m,6},{z,32},{x,32},{y,32}];
For[m=1,m<=6,m++,
For[z=1,z<=32,z++,
IMAGE[[m,z]]=cfft[doubletimage[[m,z]]];
For[x=1,x<=32,x++,
For[y=1,y<=32,y++,
REIMAGE[[m,x,y,z]]=IMAGE[[m,z,x,y]]];];];
```

Figure 8.17: *Mathematica* code to create the Fourier space matrix IMAGE.

```
INOTF=Table[0.,{x,32},{y,32}];
ri=Table[0.,{x,64},{y,32}];
singularvalues=Table[0.,{x,32},{y,32},{i,32}];
OBJ=Table[0.,{m,6},{z,32},{x,32},{y,32}];
a=.09
SessionTime[]
For[x=1,x<=32,x++,
For[y=1,y<=32,y++,

For[k=1,k<=32,k++,          "form the 2NxN real valued matrix"
ri[[k]]=Re[OTF[[x,y,k]]];
ri[[k+32]]=Im[OTF[[x,y,k]]];];

{u,md,v}=SingularValues[ri];  "use the SVD command to find the
singularvalues[[x,y]]=md;      three matrices U,W & V^T"
w=md/(md^2+a^2);
inri=Transpose[v].DiagonalMatrix[w].u;  "find the inverse"
INOTF=inri.inim;                  "reorder into the complex inverse matrix"

For[m=1,m<=6,m++,          "Find the object from O=H^-1I"
OBJ[[m,x,y]]=INOTF.REIMAGE[[m,x,y]]];];

];
Print[x];
];
SessionTime[]
71630.88
73563.42
{Max[singularvalues],Min[singularvalues]}
{14.5595, 0.0000512428}
```

Figure 8.18: *Mathematica* code finds the SVD matrices, inverts the OTF and finds the reconstructed OBJ matrix.

The singular value decomposition, inverse and object reconstruction are performed with the code listed in Figure 8.18. The matrix **ri** is the 2NxN matrix of real values. The function `SingularValues[ri]` outputs the three matrices **u**, **md**, and **v**. The singular values

md are stored for future investigation and the α noise suppression is applied. The inverse is stored in **INOTF** then multiplied by the **IMAGE** resulting in **OBJ**. This is then inverse Fourier transformed to reconstruct the **object** cube in the program listed in Figure 8.19.

```

"Reorder the matrices"
REOBJ=Table[0., {n,6},{i,32},{j,32},{k,32}];
object=Table[0., {n,6},{i,32},{j,32},{k,32}];
For[z=1,z<=32,z++,
For[x=1,x<=32,x++,
For[y=1,y<=32,y++,
For[m=1,m<=6,m++,
REOBJ[[m,z,x,y]]=OBJ[[m,x,y,z]]];];];
"Take the inverse Fourier Transform of OBJ to find the object cubes"
For[m=1,m<=6,m++,
For[z=1,z<=32,z++,
object[[m,z]]=Abs[Cinfft[REOBJ[[m,z]]]];
];Print[m];

```

Figure 8.19: *Mathematica* code takes the inverse Fourier transform of the OBJ matrix.

The singular values, $w_{ii}(\xi, \zeta)$, of the **OTF** matrix are plotted in Figure 8.20. Each image is a density plot of the spatial frequencies contained at a given spectral frequency. Notice that there is a region of black pixels in the center of each image which grows with increasing spectral frequencies. This represents low frequency spatial/spectral information that isn't imaged by DOIS or recoverable with processing. Plotted in Figure 8.21 as a cross-section of each spectral frequency, the frequently discussed missing cone which plagues such imaging systems is seen [Barrett 1981, Mooney 1995, Descour 1995].

Singular value decomposition inverse reconstruction provides a unique and valuable opportunity to quantify the missing cone. The missing spatial and spectral frequencies can be determined from the design parameters to predict the cut off frequencies and used as a figure of merit when designing and comparing future imaging spectrometers.

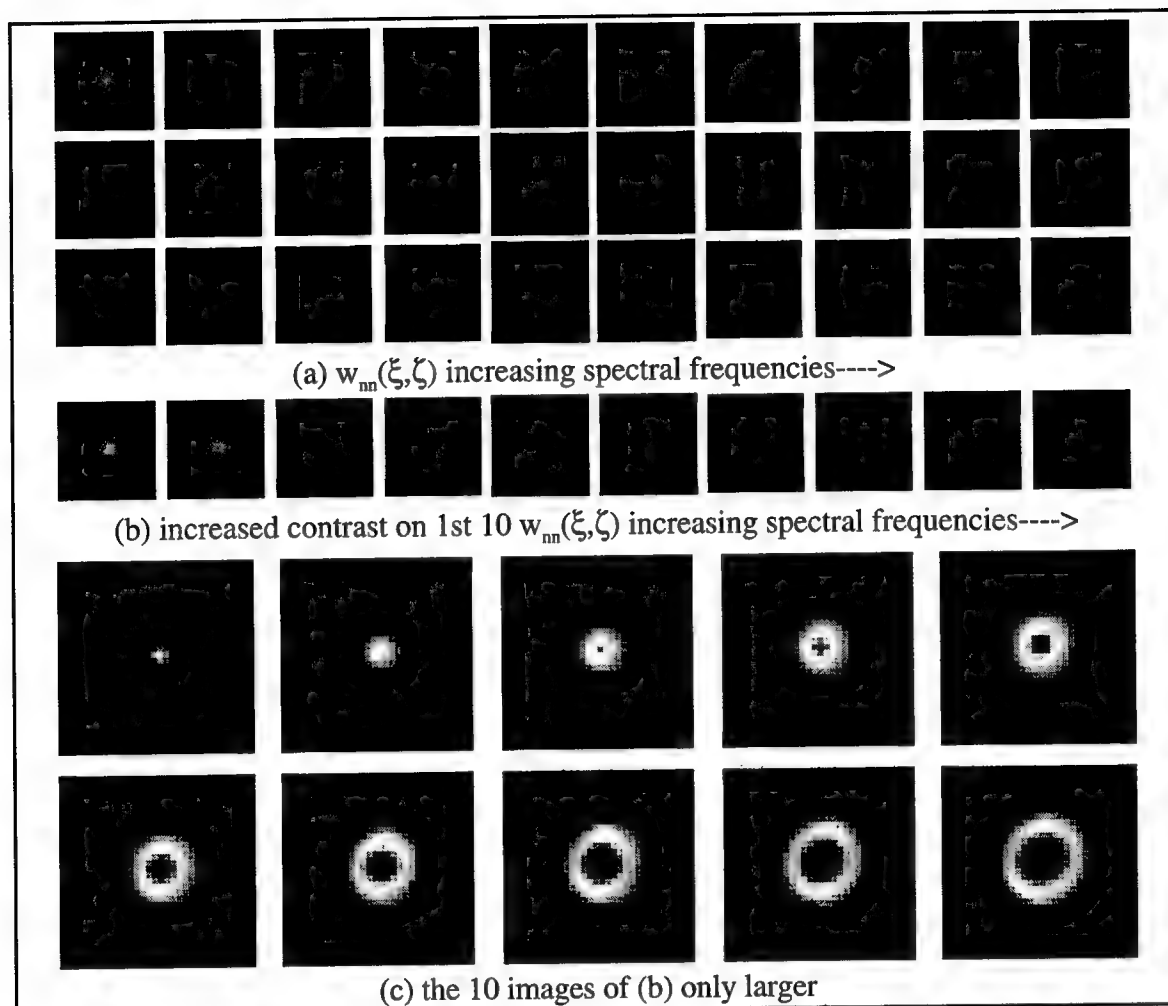


Figure 8.20: Singular Values $w_{nn}(\xi, \zeta)$ Matrix plots.

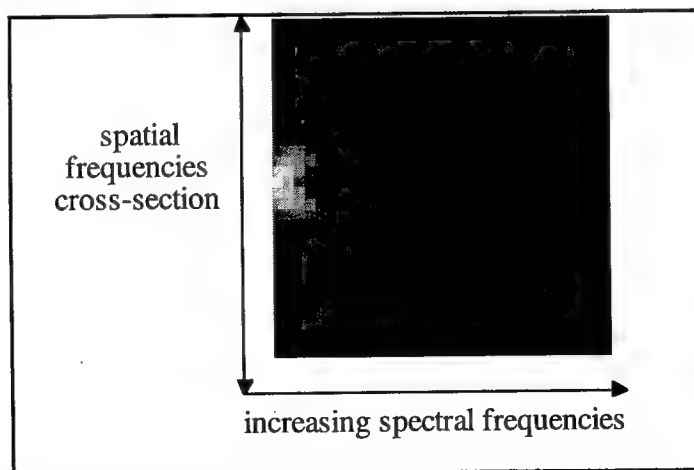


Figure 8.21: Cross-section shows missing cone.

8.3.3.1 SVD results

The following figures present results from applying the SVD object reconstruction algorithm from equation 8.24 to computer generated (CG) and experimentally measured images cubes, $(32x, 32y, 32z(\lambda))$ in size. Figure 8.23 depicts the results from reconstructing the CG object cubes of increasing square apertures in front of a Hg doublet that were generated in section 6.2.2. As expected, the doublet is indeed reconstructed using the SVD. Looking closer at the results, Figures 8.24 and 8.25 picture the same CG data sets but displayed as series of spectral images. The first is from the 8×8 square aperture, and the second from the 16×16 square. Objects were reconstructed with the regularization filter value α set to 0.5, 0.1 and 0.05 from equation 8.23. Notice that only 30 images are printed for each image series, for convenience the 1st and 32nd were omitted from the figure. Figure 8.22 lists the location values $z(\lambda)$ corresponding to the $(32x, 32y)$ images pictured in the series. Recall that each step represents $dz \approx 0.125\text{mm}$ and spectral step size $d\lambda \approx .25\text{nm}$ in both the CG and experimental cubes. The entire 32 step series records an 8nm band, a resolution that rivals any spectral filter.

2	3	4	5	6	7	8	9	10	11
12	13	14	15	16	17	18	19	20	21
22	23	24	25	26	27	28	29	30	31

Figure 8.22: Table of the z values for the following output series.

In (a) of Figure 8.24 and 8.25, the square aperture emits at locations 14 and 20. The effect of DOIS imaging is seen in (b): the edges of the squares are blurred, and it inaccurately measures the presence of the square in more than the two locations, the image is now blurred over most z locations. The SVD Inverse filter algorithm was applied with α equal to 0.5, 0.1 and 0.05 with the results displayed in (c), (d) and (e) respectively. The

reconstruction does reduce the occurrence of the square in the inaccurate locations, and the square is sharpened. As α is made lower, the reconstruction is better; however, noise and ghost images are introduced which aren't present in the (b) image cube.

Interestingly, the reconstructed object squares appear to be shifted by two z locations, $d\lambda \approx 0.5$ nm. The cause of this shift is indeterminate, an investigation into this is matter is recommended as a suggestion for further work.

The SVD algorithm was applied to four different experimentally measured image cubes. Each target was assembled to demonstrate a variety of spectral/spatial characteristics. For consistency Figure 8.26 shows that the SVD reconstruction works well on the experimentally measured 577/579 nm Mercury doublet with the X aperture. The noise regularization value α was set to 0.5, 0.1 and 0.05 for (b), (c) and (d) respectively in the figures of all four targets.

The second target combines a 542nm GreNe laser point source imaged along side the 546 nm Hg lamp with a trapezoidal aperture. The recorded image cube and reconstructed object cubes are shown in Figure 8.27. The SVD reconstruction improved both the spectral and spatial quality of the images without the artifacts demonstrated with the other algorithms.

To touch on larger targets, an almost full FOV rectangle aperture was placed in front of the Hg doublet in Figure 8.28. Although the 2nm doublet can't be resolved, DOIS measures it to be a line with about 4 nm FWHM using the SVD reconstruction, and the spatial information of the rectangle aperture is reconstructed. Finally, the mercury illuminated iris image cube was processed with the SVD. The results are shown in Figure 8.29, notice that a "hot spot" on the bulb has been reconstructed.

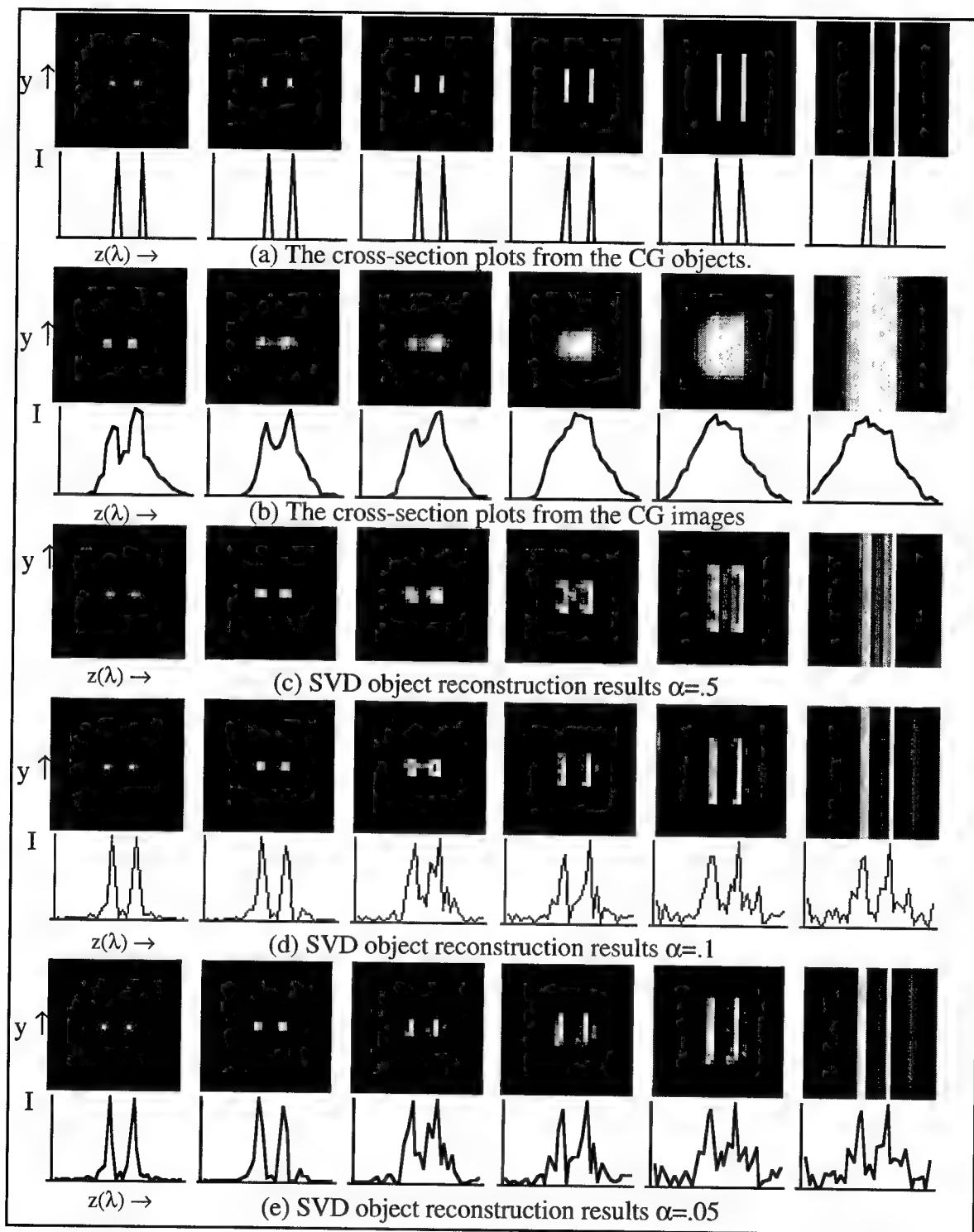


Figure 8.23: $z(\lambda)$ vs. y cross-section and spectral plots from SVD applied to CG Doublet.

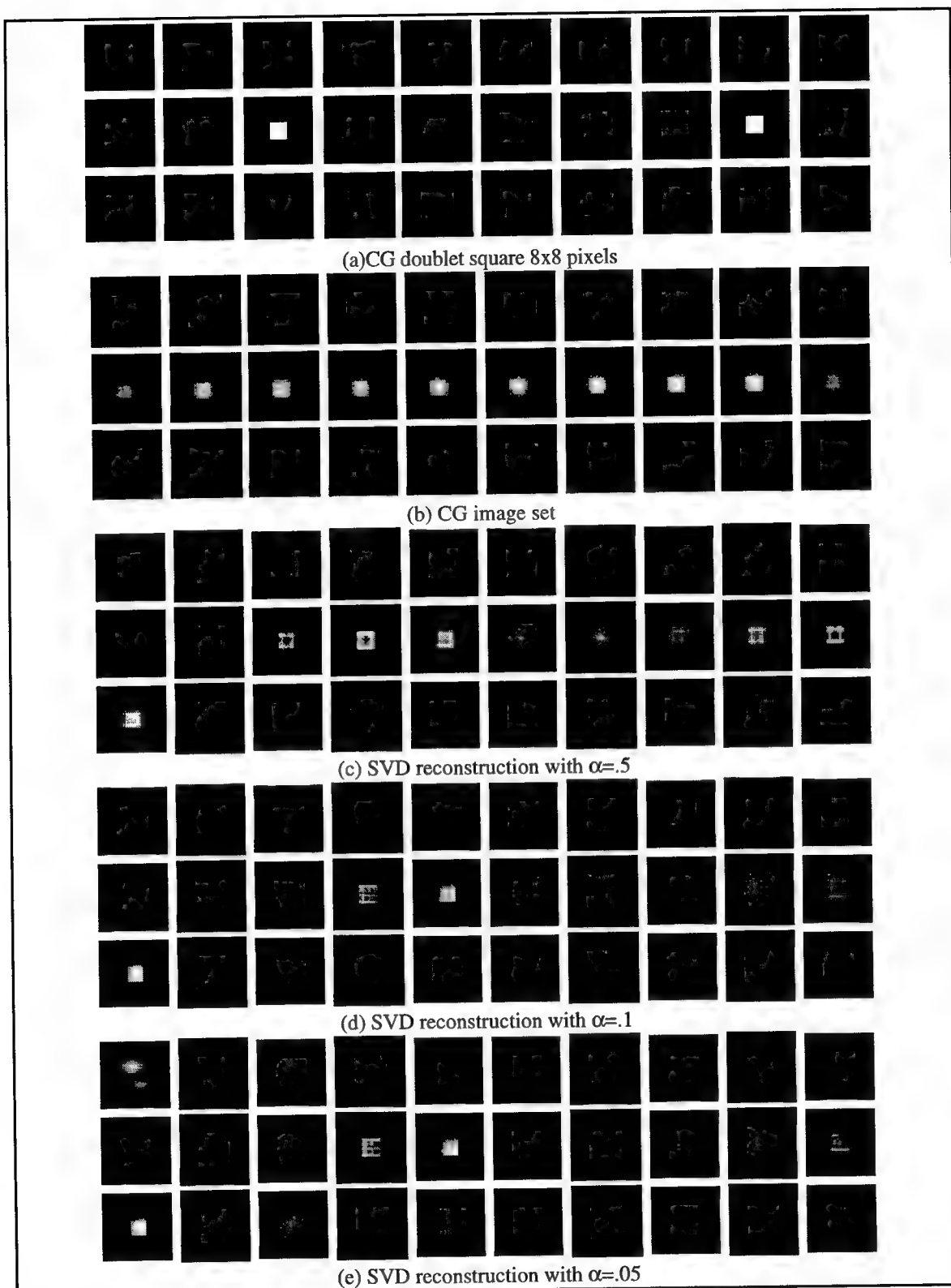


Figure 8.24: SVD reconstructed object series from the CG 8 x 8 pixel doublet aperture, previously depicted as cross-sections in 8.23.

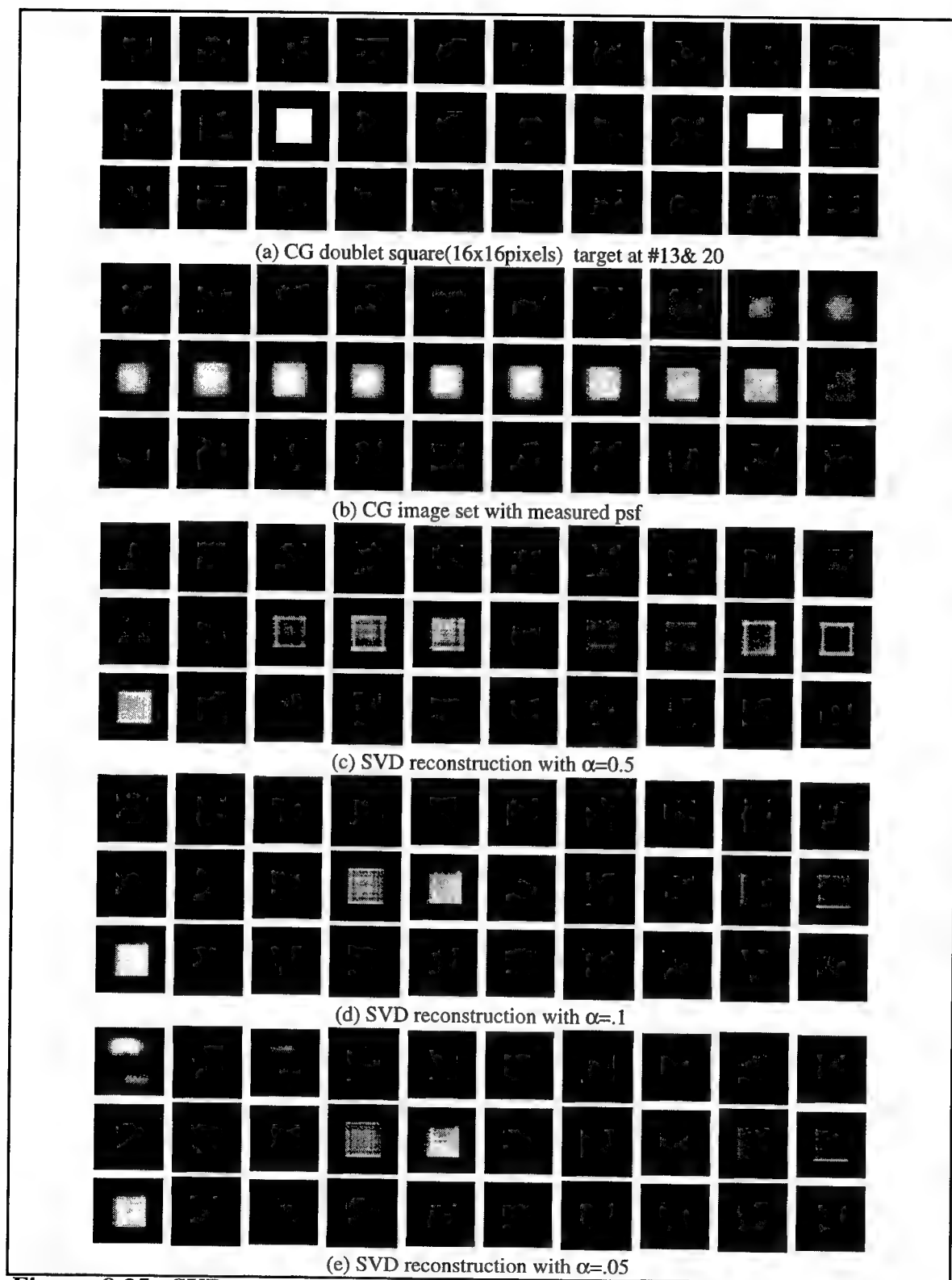


Figure 8.25: SVD reconstructed object series from the CG 16 x16 pixel doublet aperture, previously depicted as cross-sections in 8.23.

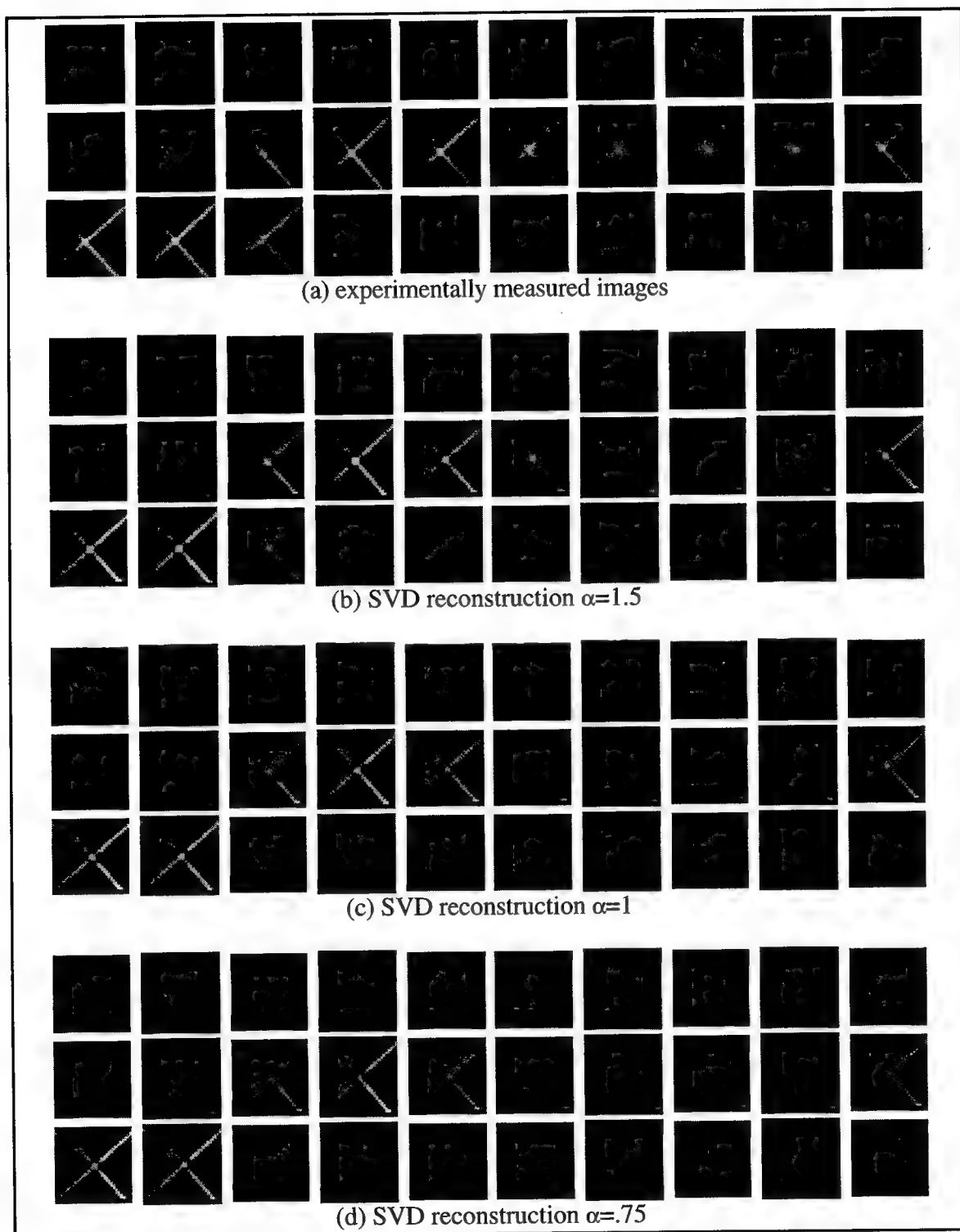


Figure 8.26: SVD reconstructed object series from the experimentally measured Hg 577/579 nm X.

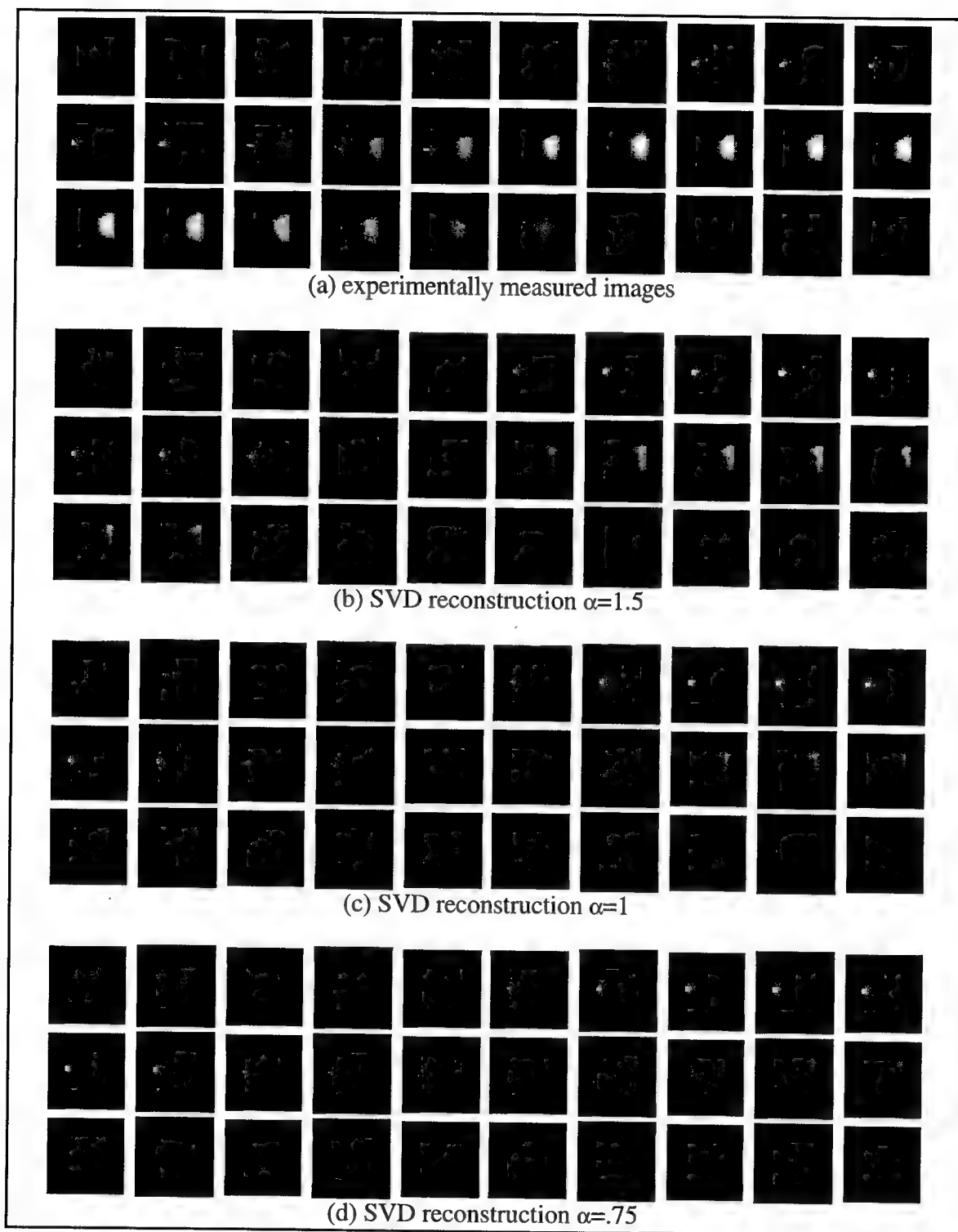


Figure 8.27: SVD reconstructed object series from the experimentally measured 542 nm GrNe point-source with a trapezoidal 546 nm Mercury target.

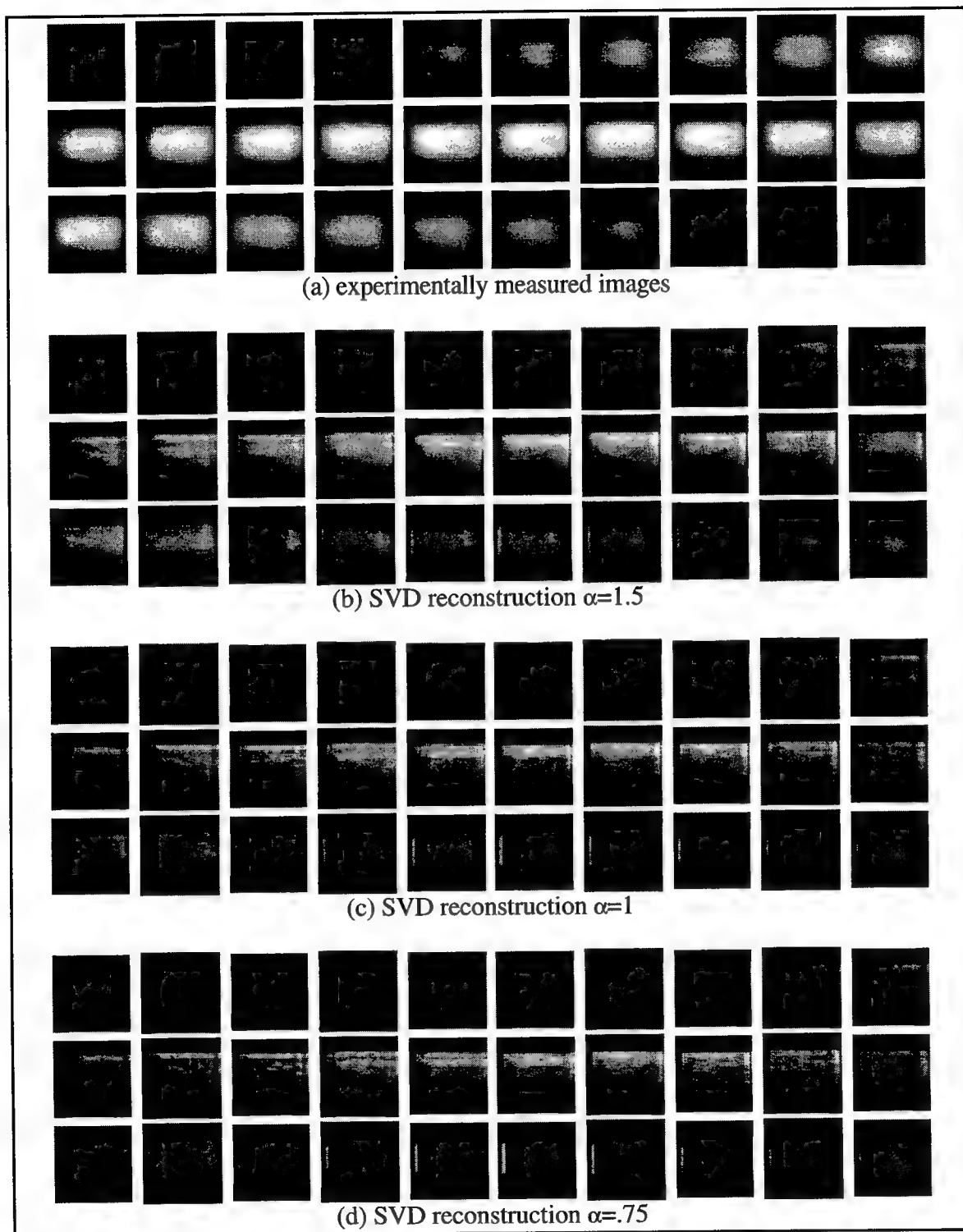


Figure 8.28: SVD reconstructed object series from the experimentally measured Mercury Rectangle.

(notice poor reconstruction when the target extends to the edges)

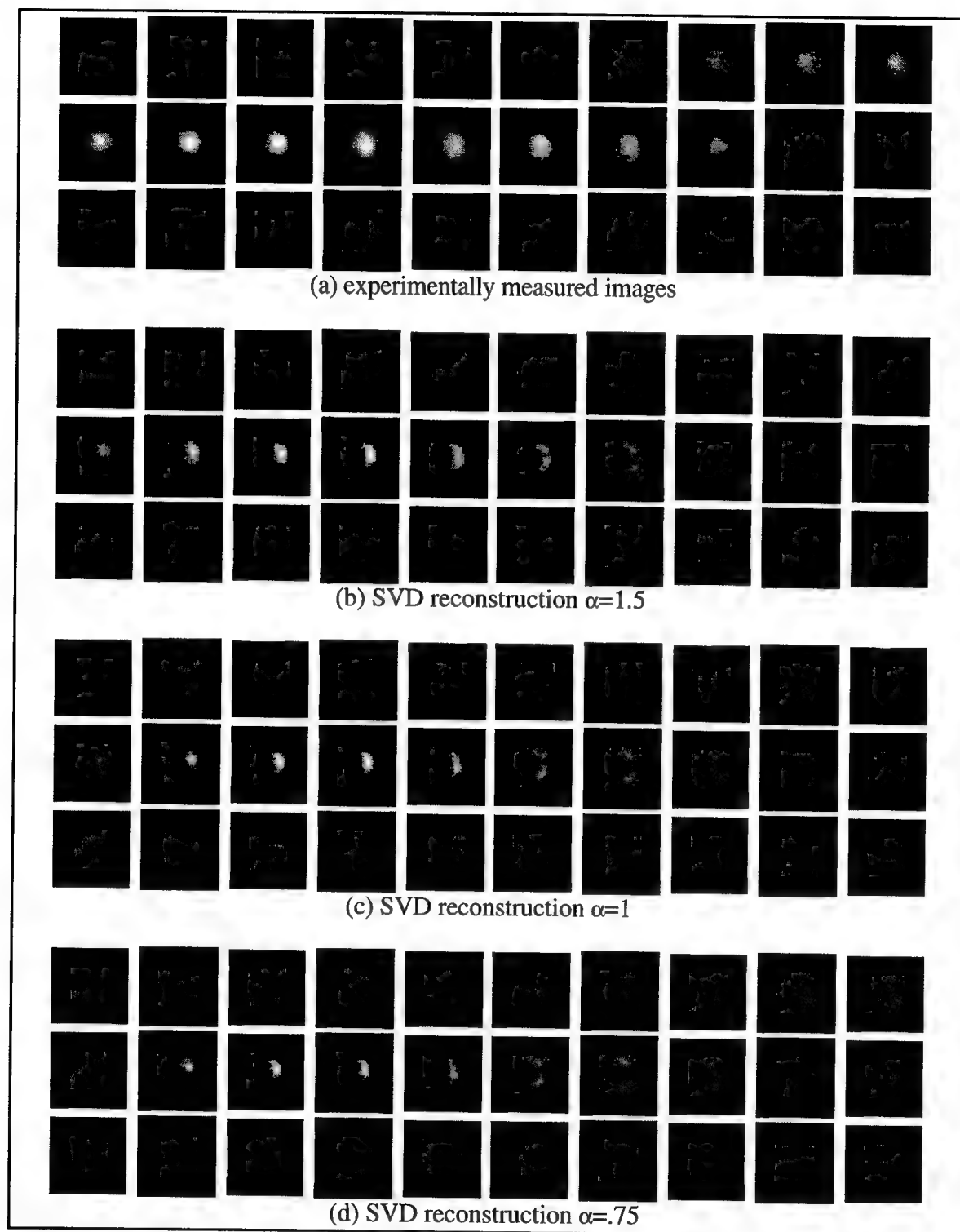


Figure 8.29: SVD reconstructed object series from the experimentally measured Iris illuminated by a Mercury bulb (notice the hot spot).

8.4 Constrained Iterative Deconvolution

The SVD Inverse Reconstruction algorithm with a regularized filter for noise suppression provides a linear restoration. One drawback of such linear methods is that negative ripples build up around strong features from the low values of the OTF and no reconstruction is possible beyond the OTF cutoff. Nonlinear restoration methods that constrain the result to be positive can eliminate this problem while using positivity and other a priori information to provide a better restoration. The drawback is that these methods are invariably iterative and hence quite computationally expensive in three dimensions. An additional challenge is to develop a relaxation parameter optimized for a particular application and image cube.

The strategy is to develop a positively constrained solution or guess object cube g_o , that when convolved with the known smearing function h will regenerate the observed image cube i . The pixel-by-pixel differences between the convolved guess and the observed data are used to update the guess.

$$\begin{aligned} gi^k &= go^k * h \\ go^{k+1} &= go^k + \gamma(i - gi^k) \\ \text{if } go^{k+1} \leq 0 &\text{ then } go^{k+1} = 0 \\ k &= k + 1 \end{aligned} \tag{8.25}$$

This is the Jansson-vanCittert constrained iterative deconvolution algorithm with the relaxation parameter [Jansson 1984]:

$$\gamma = r_o \left[1 - 2 \left| go^k - \frac{1}{2} \right| \right] \tag{8.26}$$

which applies the a priori information that the intensity is a positive value and that the spectra is a transmission function with a maximum value of 1. The best results were obtained with an initial guess equal to the regularized inverse filtered data set and a weighted relaxation parameter, γ .

The vanCittert iterative technique with a Jansson relaxation parameter of equation (8.25) was implemented in *Mathematica* and is listed in Figure 8.30. The algorithm was applied to the X Mercury doublet. The results after 10 and 20 iterations are pictured in Figure 8.31. The spectral radiance curve plotted in Figure 8.32 shows that the doublet is better resolved with every iteration.

```
gama=flatmimage/Max[flatmimage];
gobj=regularizedobj;
Print["=start time"SessionTime[]]; Print["=original maxobj"Max[gobj]];
Do[
  GOBJ=cflatfft[gobj];
  gi=Abs[cflatinfft[GOBJ*FLATOTF]];
  diff=flatmimage-gi;
  gobj=gobj+gama*diff;
  gobj=(gobj+Abs[gobj])/2;
  objnum[[c]]=gobj;
  Print["iteration"];Print[c]; Print["=maxobj"Max[gobj]]; Print["=maxdiff"Max[diff]];
  Print["=mindiff"Min[diff]]; Print["time"SessionTime[]];
  ,{c,20}]
```

Figure 8.30: *Mathematica* code for the Jansson-vanCittert algorithm.

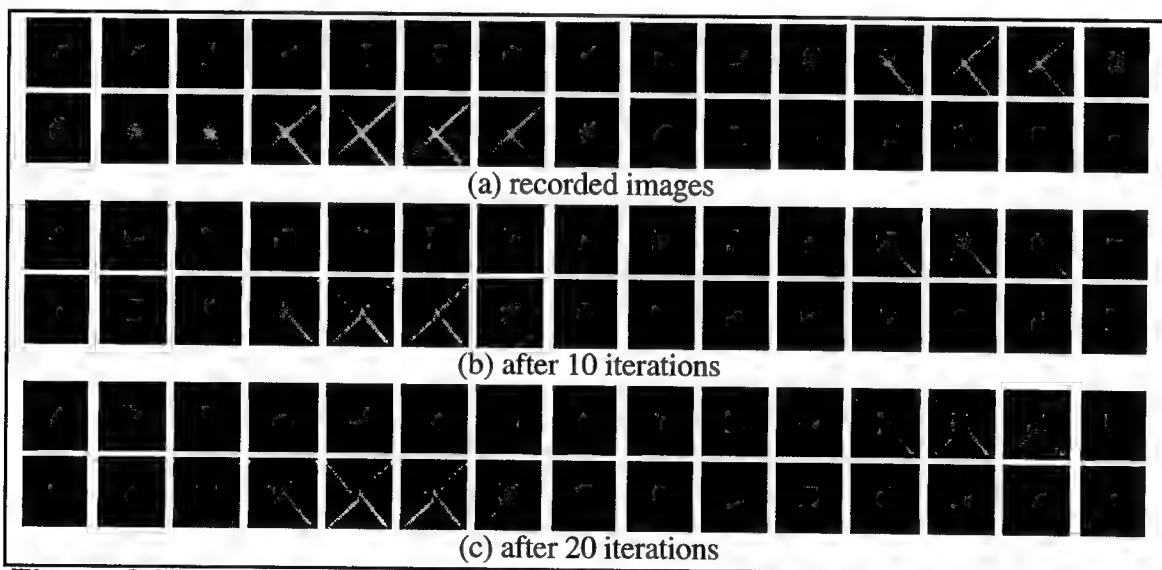


Figure 8.31: Resulting images after Jansson-vanCittert reconstruction with various iterations. (a) original recorded data. (b) $n=10$. (c) $n=20$.

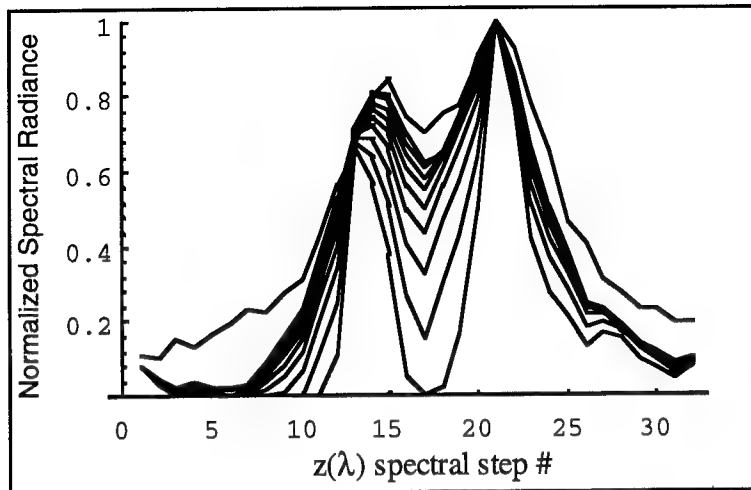


Figure 8.32: Spectral Radiance of pixel 16,16 Jansson-vanCittert reconstruction at various iterations.

The Jansson-vanCittert algorithm didn't work for large targets or data with excessive noise. Various relaxation functions were implemented and several hundred iterations ran without ever reaching convergence. This inspired the addition of another step to the algorithm. The difference term is inverse filtered with a regularized inverse filter as described in equation (8.27). This achieved much better results that converge within a few iterations.

$$\begin{aligned}
 gi^k &= go^k * h \\
 diff &= i - gi^k \\
 DIFF &= Fourier[diff] \\
 regulardiff &= Abs \left[InverseFourier \left[DIFF \left(\frac{H^*}{H^*H + \alpha} \right) \right] \right] \quad (8.27) \\
 go^{k+1} &= go^k + regulardiff \\
 \text{if } go^{k+1} \leq 0 &\text{ then } go^{k+1} = 0 \\
 k &= k + 1
 \end{aligned}$$

The *regularized inverse filtered vanCittert* algorithm of equation (8.27) was implemented in *Mathematica* with the code listed in Figure 8.33. It was applied to CG doublet and experimentally measured iris images. The rms difference between the recorded

images and the guess images is plotted against the number of iteration in Figure 8.34; they show convergence in less than 5 iterations.

```

start with measured image
image=flatmimage/Max[flatmimage];
gobj=image;
a=.01
Print["start time"SessionTime[]];
Do[ gimage=Abs[cflatinfft[cflatfft[gobj]*FLATOTF]];
gimage=gimage/Max[gimage];
diff=image-gimage;
diff=diff-Min[diff];
n=Ceiling[(c)];
REGULARDIFF=cflatfft[diff]*Conjugate[FLATOTF]/((FLATOTF*Conjugate[FLATOTF])+a);
regulardiff[[n]]=Abs[cflatinfft[REGULARDIFF]];
gobj=gobj+regulardiff[[n]];
rms[[c]]=Mean[Abs[regulardiff[[n]]]];
objnum[[n]]=gobj;
Print["iteration" c]; Print["rms"rms[[c]]];
,{c,20}
Print["time"SessionTime[]];
For[i=1., i<=1, i++,
par[[i]]=Partition[reblurredobject,1024];
For[j=1., j<=32, j++,
obj[[i,j]]=Partition[par[[i,j]],32];
obj[[i,j]]=Transpose[RotateRight[Transpose[RotateRight[obj[[i,j]],16],16],];];
For[m=1, m<=1, m++,
For[z=1, z<=32, z++,
trans[[z]]=Transpose[obj[[m,z]]];
h[[m,z]]=trans[[z,16]];
w[[m,z]]=obj[[m,z,16]];];
h[[m]]=Transpose[h[[m]]];
w[[m]]=Transpose[w[[m]]];];

```

Figure 8.33: Mathematica code for regularized inverse filtered vanCittert iterative reconstruction.

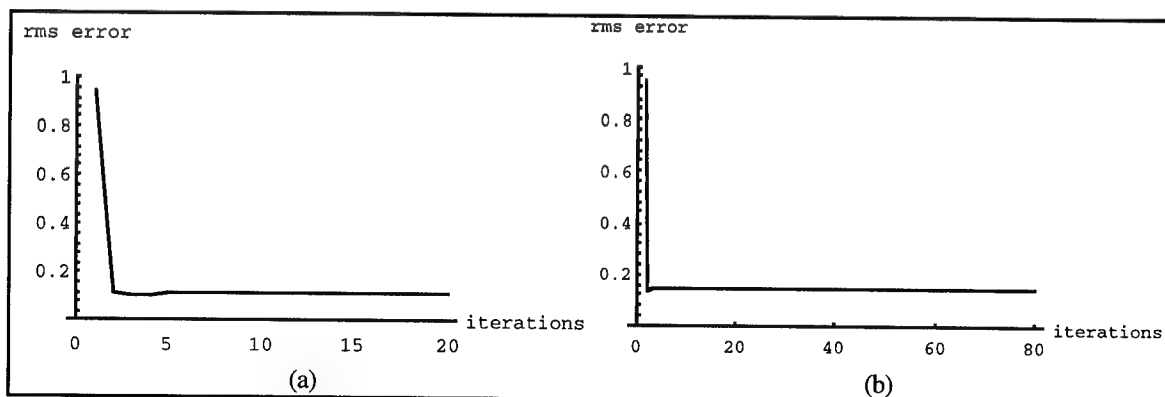


Figure 8.34: CG doublet; rms error after each iteration for (a) the CG doublet and (b) the iris.

The results are depicted in Figures 8.35, 8.36 and 8.37. The objects' spectral and spatial information is reconstructed, including the lamp hot spot and spectral doublet in the iris data. Although this algorithm does look promising, it requires the regularized inverse filter which was shown to make approximations that aren't always appropriate. See the wrap around problems in the iris plots which result in improper peaks in the tails of the spectral plots. It was also found that the algorithm had to be manipulated to fit the target. This aside, the constrained iterative technique could still be a solution to the deconvolution problem for certain applications, particularly if DOIS were required to image the same or similar targets repeatedly.

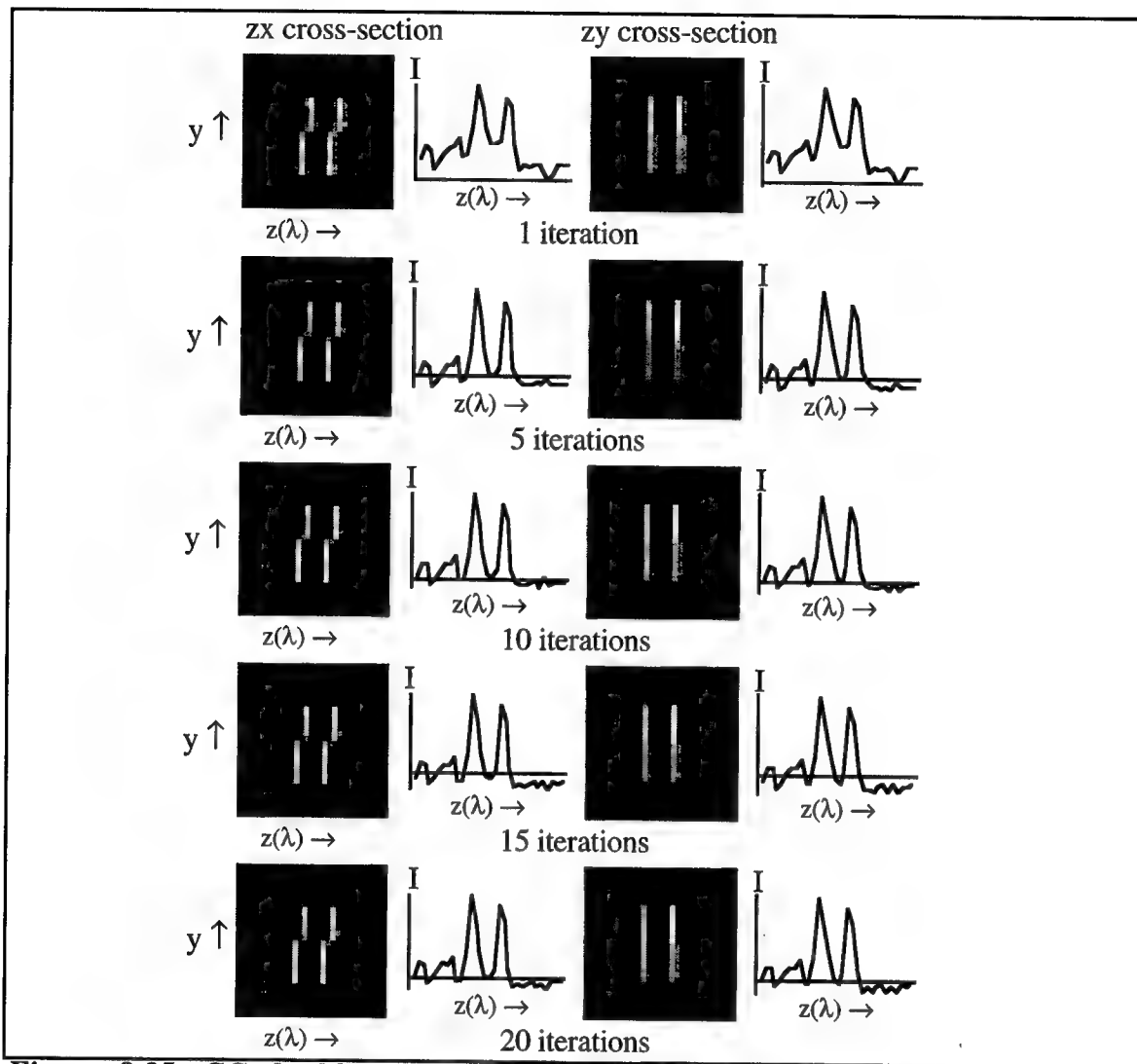


Figure 8.35: CG doublet; results of regularized inverse filtered vanCittert iterative reconstruction with $\alpha = 0.001$.

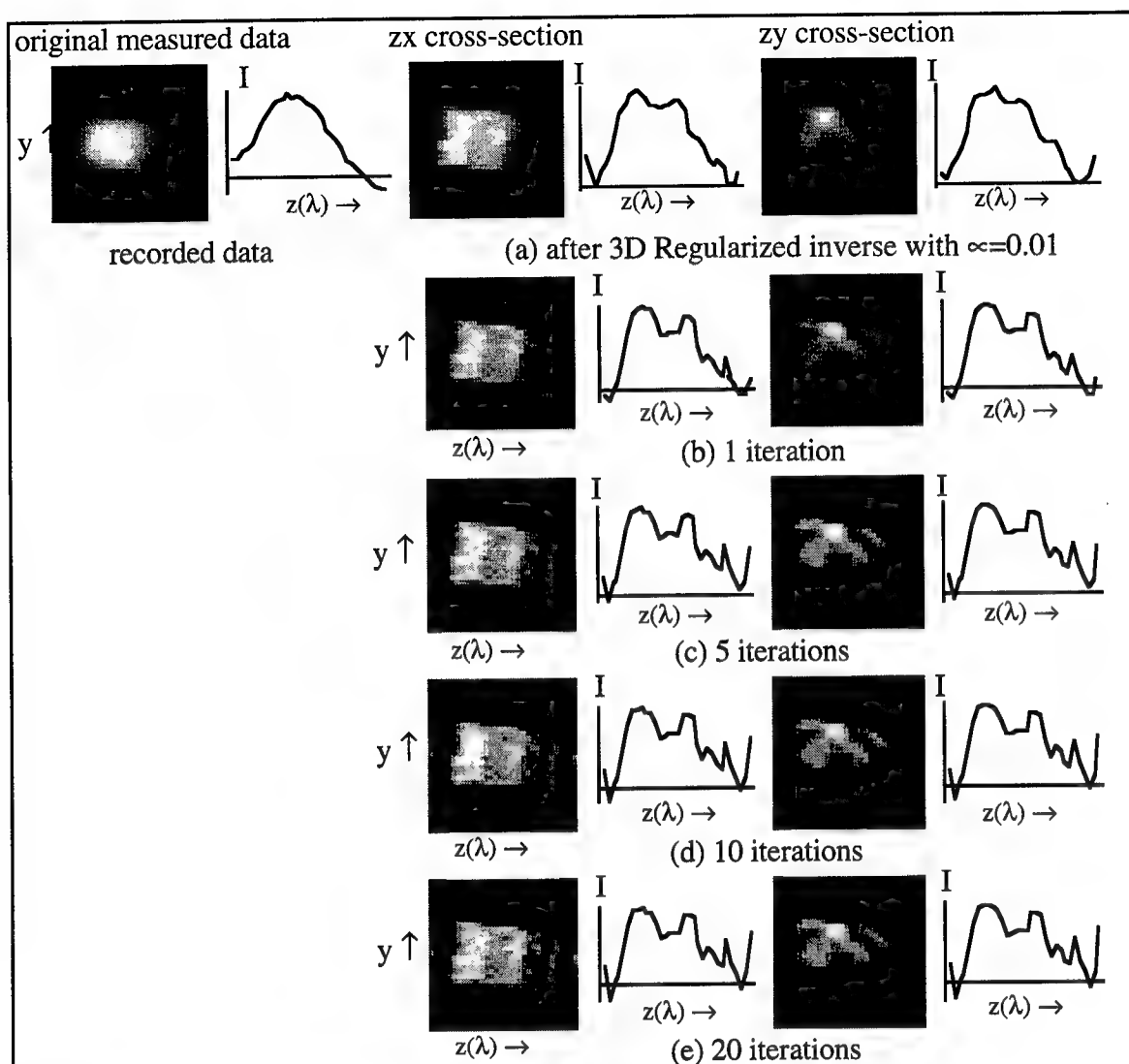


Figure 8.36: Results of iris reconstruction after (a) 3D Regularized inverse filter and (b-e) with regularized inverse filtered vanCittert iterative reconstruction $\alpha=.01$.

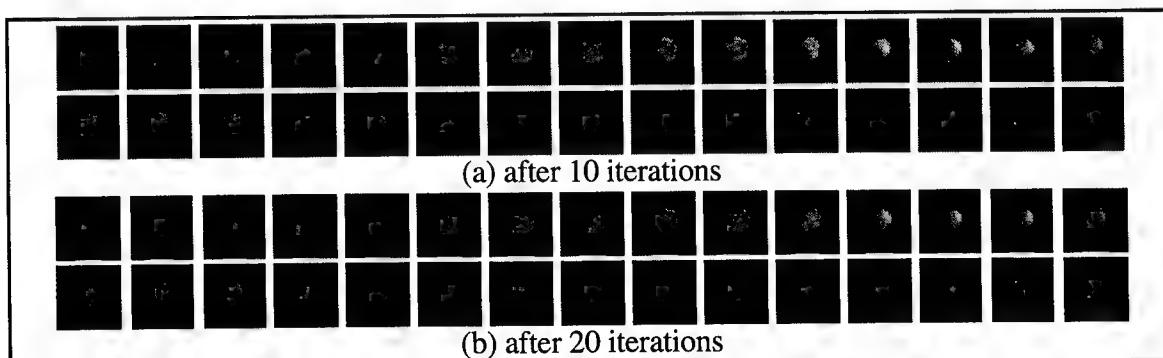


Figure 8.37: Reconstructed iris objects after 10 & 20 iterations.

9. CONCLUSION

The Diffractive Optic Image Spectrometer (DOIS) is a viable multi-spectral imager.

This dissertation demonstrated and proved the concept of spectral imaging with a diffractive optic. More importantly, the theory of spectral imaging with a diffractive optic, referred to as diffractive spectral sectioning, was developed and an appropriate digital image restoration algorithm was derived to deconvolve the DOE transfer function from the recorded image cube, providing a high resolution spectral/spatial object cube.

The spectral resolving power of 288 ($\lambda_c/\Delta\lambda = 577_{\text{nm}}/2_{\text{nm}}$) demonstrated by the DOIS prototype can be utilized to predict capability of future diffractive optic image spectrometer designs applied in any spectral range; UV, visible or IR.

I conclude that the best image spectrometer designed with a diffractive optic would include a kinoform; a high efficiency, multi-level DOE with a refractive surface to balance the spherical and off axis aberrations. An intermediate zoom lens should be used to perform the spectral scanning while maintaining a constant magnification. The most accurate and powerful reconstruction algorithm is the Singular Value Decomposition Inverse Filter with a regularization term for noise suppression.

9.1 DOIS Advantages

DOIS has several advantages over current image spectrometers. It incorporates a simple one axis translation on a rugged platform making it insensitive to vibrations which limit Fourier Transform spectrometers. DOIS is programmable, providing single spectra, narrowband or full spectrum image cubes. It can provide coarse or fine spectral resolution by choosing the stepping increment and an object reconstruction algorithm at various levels of computational expense.

DOIS uses mainly off the shelf components. The DOE fabrication does have a large first time expense to generate a master; however, multiple copies can be replicated at minimal expense. The design is not limited by the availability of materials like conventional thin film spectral filters. Once built for one application, additional wavelengths within a wide spectral range can be viewed for other applications without changing components.

DOIS solves a common problem associated with spectral filters; the central wavelength of a filter's bandpass can shift due to environmental factors such as temperature. This can be corrected for in a DOIS system with a simple change in position, making on-board calibration and realignment possible.

DOIS provides enough spectral and spatial image quality without post-detection processing that there are applications where the recorded image cube can be utilized to represent the target. Contrary to computer-tomography approaches, even when object reconstruction processing is required the pre-processed images are at least recognizable so that the operator can have confidence while recording the data.

The DOIS spectrometry feature can be added to existing camera systems with a simple lens/mount replacement, providing additional information for the difficult task of target identification. DOIS can also be a cost effective solution to spectroscopy applications where imaging isn't required but would serve as a bonus. The imaging will help in minimizing misalignment and improve tracking of moving targets. The additional pixels within the field of view could act as simultaneous data measurements that can be averaged to improve accuracy and reduce noise.

As with most imaging spectrometers the scanning mechanism will limit use in applications with short lifetimes, however as presented below in section 9.2.3, a DOIS system can be designed with no moving parts, recording the entire image cube in a single "snapshot".

9.2 Suggestions for future work

During this dissertation several ideas were conceived for continued research with diffractive optic imaging spectrometers and are presented below. Additionally, it was discussed in section 6.2.2 that a field stop should be added to the optical train to aid in reconstructing targets on the edge of the field of view and that an investigation should be performed into the cause of a spectral shift in the reconstructed data in Figure 6.7.

9.2.1 Dual Waveband design using multiple orders

While working with the 2 level zone plate, 5 separate diffractive orders were observed by scanning the detector closer to the DOE. Each order is located at $\frac{f}{m}$, where f is the focal length of the first diffractive order and m is the diffractive order number. While viewing wideband emitting targets, the orders started to superimpose one another. Why not use this effect to design a multi-band spectral imager, where the DOE images far IR radiation in the first order and the mid IR in the second order?

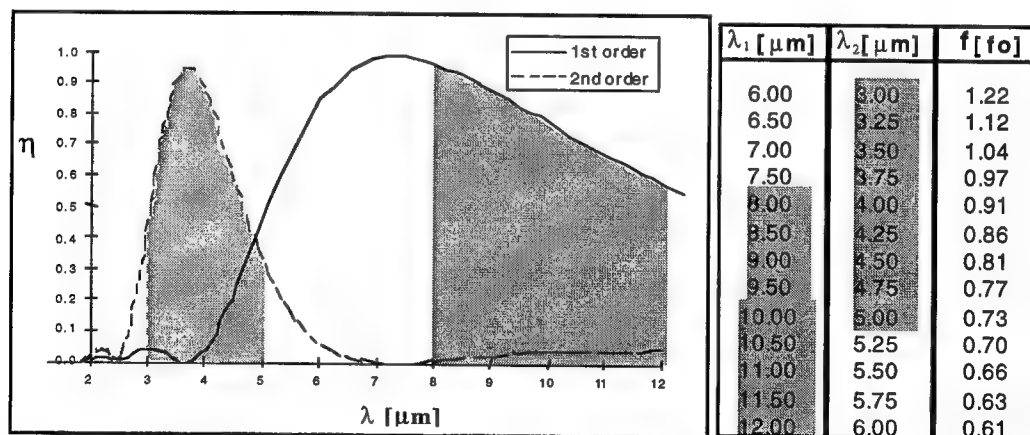


Figure 9.1: Two waveband design, mid IR and far IR, with $\lambda_0=7.3\mu\text{m}$ spectral η for each order, and the two wavelengths at each focal position.

A 16 level DOE designed at $\lambda_d=7.3\mu\text{m}$ images 8 to $12\mu\text{m}$ far IR radiation in its first order and 3 to $5\mu\text{m}$ mid IR in its second diffractive order. Figure 9.1 shows the 1st and 2nd order spectral diffraction efficiency for a $\lambda_d=7.3\mu\text{m}$ DOE. The two wavelengths that are

imaged at each focal position are listed in Figure 9.1(b). One can think of various detector configurations, as well as an array of both mid and far IR detectors.

This multi-order concept was demonstrated with the DOIS visible prototype. The second order image of a 633 nm HeNe laser came to focus at the same plane as the third order image of a 422 nm monochromator slit.

9.2.2 Programmable DOE with an SLM, variable focus device

Depicted in Figure 9.2, an electronically controlled variable focus diffractive lens or spatial light modulator (SLM), can replace the DOE in the diffractive optic image spectrometer to create a DOIS with no moving parts. The components are mounted with a fixed separation. The SLM will select the image spectra by electronically changing the DOE ring spacing, which will change the focal length [Domash 1996].

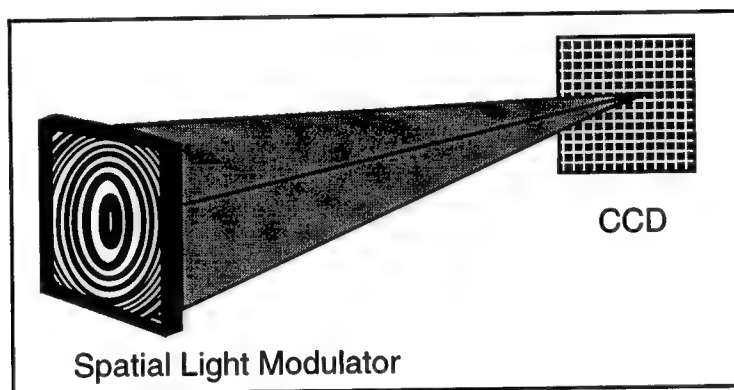


Figure 9.2: Design for a static DOIS with a controllable, variable focus lens.

9.2.3 Array of DOEs

Finally, an image spectrometer can be designed with diffractive optics and no moving parts to record the entire 3D image cube simultaneously. Figure 9.3 is the schematic of a DOIS "snapshot" technique which records a set of images at predetermined spectral lines. Each lens of the array is fabricated to have the same design focal length but at different wavelengths. The detector array is segmented into a region for each wavelength or

an array of detector arrays could be assembled. This configuration eliminates scanning and magnification differences. However unlike a segmented detector with an array of filters, if the temperature shifts or requirements change the array can easily be repositioned at a different distance to detect another set of spectra. Additionally, by fabricating one lens to be refractive, such as a Fresnel Lens, a conventional full-band image of the entire scene can be recorded as well.

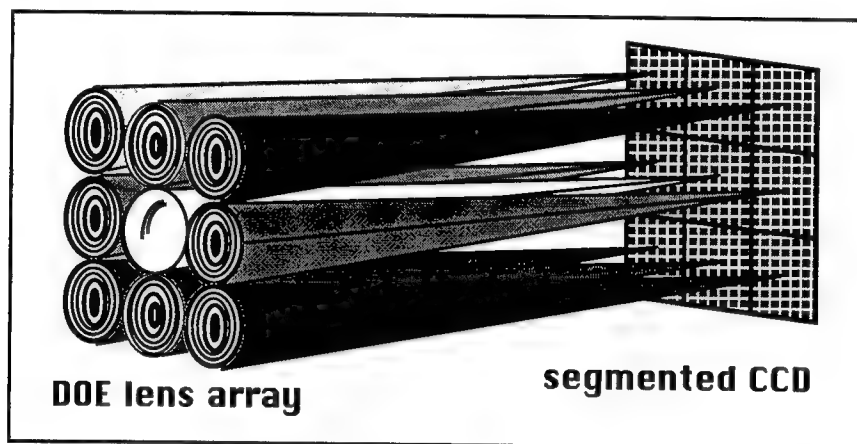


Figure 9.3: Design for a static DOIS with a DOE lens array.

In conclusion, DOIS, the diffractive optic imaging spectrometer presented in this dissertation is a practical, high resolution, compact, economical, rugged, programmable, multi-spectral imager. With proper selection of the DOE substrate and detector material, it can be built to operate at ultraviolet, visible or infrared wavelengths for applications in surveillance, remote sensing, law enforcement, environmental monitoring, laser communications, medical imaging and laser counter intelligence.

REFERENCES

Agard D.A., Hiraoka Y., Sedat J.W., "Three-dimensional Microscopy: image processing for high resolution subcellular imaging," *SPIE Vol.1161 New methods in Microscopy and Low Light Imaging*, pp.24-30, (1989).

Agard D.A., Hiraoka Y., Shaw P., Sedat J.W., Fluorescence Microscopy in Three-dimensions," *Methods in Cell Biology* Vol.30 Ch.13, pp.353-377, Academic Press (1989).

Aikens R.S., Agard D.A., Sedat J.W., "Solid-State Imagers for Microscopy," *Methods in Cell Biology* Vol. 29 Ch.16, pp.291-313, Academic Press (1989).

Andrews H.C., Hunt B.R., *Digital Image Restoration*, aaaaaaprentice-Hall (1977).

Barrett H.H., Swindell W., *Radiological Imaging*, Academic Press (1981).

Bernhardt P.A., "Direct reconstruction methods for hyperspectral imaging with rotational spectrotomography," *J. Opt. Soc. Am.* 12,9 (September 1995).

Blass W. E. and Halsey G. W., *Deconvolution of Absorption Spectra*, Academic Press (1981).

Born M., Wolf E., *Principles of Optics*, Pergamon Press, pp. 439-441, (1989)

Bronson R., *Matrix Methods: An Introduction*, Academic Press (1970).

Byrne C.L., "Block Methods for Image Reconstruction from Projections," *IEEE Transactions on Image Processing* Vol.5 No. 5, pp. 792-794 (May 1996).

Byrne C.L., "Iterative Image Reconstruction Algorithms Based on Cross-Entropy Minimization," *IEEE Transactions on Image Processing* Vol.2 No.1, pp. 96-103 (January 1993).

Castleman K.R., *Digital Image Processing*, Prentice-Hall (1979).

Chiu M.Y., Barrett H.H., Simpson R.G., "Three-dimensional reconstruction from planar projections," *J. Opt. Soc. Am.* 70,7 (July 1980).

Chiu M.Y., Barrett H.H., Simpson R.G., Chou C., Arendt J.W., Gindi G.R., "Three-dimensional radiographic imaging with a restricted view angle," *J. Opt. Soc. Am.* 69,10 (October 1979).

Chmelik R., "Focusing and the optical transfer function in a rotationally symmetric optical system," *Applied Optics* Vol. 33(17), pp. 3702-3704 (June 1994).

Cochran W.T., Cooley J.W., Favini D.L., Helms H.D., Kaenel R.A., Lang W.W., Maling, G.C.Jr., Nelson D.E., Rader C.M., Welch P.D., "What Is the Fast Fourier Transform?," *Proceedings of the IEEE* Vol. 55 No.10, 1664-1677 (October 1967).

REFERENCES-Continued

- Conchello J.A., Hansen E.W., "Enhanced 3-D reconstruction from confocal scanning microscope images. I: Deterministic and maximum likelihood reconstructions," *Applied Optics* Vol. 29(26), pp.3795-3804 (10 September 1990).
- Conchello J.A., Kim J.J., Hansen E.W., "Enhanced three-dimensional reconstruction from confocal scanning microscope images. II. Depth discrimination versus signal-to-noise ratio in partially confocal images," *Applied Optics* Vol. 33(17), pp. 3740-3750 (10 June 1994).
- Conchello J.A., "Deconvolution of fluorescence microscopy images," *Pro. SPIE* 2655, (1996).
- Descour M.R., Dereniak E.L., "Nonscanning no-moving-parts image spectrometer," *Pro. SPIE* 2480, pp. 48-64, (1995).
- Descour M.R., Mooney J.M., Perry D.L., Illing L., *Imaging Spectrometry, Pro. SPIE*, 2480 (1995).
- Demoment G., "Image Reconstruction and Restoration: Overview of Common Estimation Structures and Problems," *IEEE Transactions on Acoustics, Speech, and Signal Processing* Vol. ASSP-37(12), pp. 2024-2036 (December 1989).
- Domash L.H., Chen T., Gomatam B.N., Gozewski C.M., "Computer-generated swichable diffractive elements in a polymer-dispersed liquid crystal composite," *Pro. SPIE*, 2689-26, (1996).
- Driscoll W.G., Vaughan W., *Handbook of Optics*, McGraw-Hill (1978).
- Erhardt A., Zinser G., Komitowski D., Bille J., "Reconstructing 3-D light-microscope images by digital image processing," *Applied Optics* Vol. 24(2), pp. 194-200 (15 January 1985).
- Faklis, Blough, "Diffractive optics test facility", RPC Technical Report 1316-088-G-AR (1993).
- Fay F.S., Carrington W., Lifshitz L.M., Fogarty K., "Three-dimensional analysis of molecular distribution in single cells using the digital imaging microscope", *SPIE Vol.1161 New Methods in Microscopy and Low Light Imaging* (1989).
- Fink D.G., Christiansen D., *Electronics Engineers' Handbook*, pp.11-44, 11-45, McGraw-Hill (1989).
- Frieden B.R., "Optical transfer of the Three-Dimensional Object," *J. Opt. Soc. Am.* 57,1 (January 1967).
- Frieden B. R., *Picture Processing and Digital Filtering*, Springer-Verlag (1975).
- Frieden B.R., *Probability, Statistical Optics, and Data Testing*, Springer-Verlag (1983).

REFERENCES-Continued

- Gaskill J.D., *Linear Systems, Fourier Transforms, and Optics*, John Wiley & Sons (1978).
- Goetz A.F.H., "Imaging spectrometry for remote sensing: Vision to reality in 15 years," *Pro. SPIE* 2480, pp. 2-13, (1995).
- Gonzalez R.C., Wintz P., *Digital Image Processing*, Addison-Wesley (1987).
- Goodman J.W., *Introduction to Fourier Optics*, McGraw-Hill (1968).
- Goodman and Silvestri, "Some effects of Fourier-domain phase quantization," *IBM J. Res. Dev.* 14, 478 (1970).
- Hect, *Optics*, Addison-Wesley (1989).
- Herman G.T., Meyer L.B., "Algebraic Reconstruction Techniques Can Be Made Computationally Efficient," *IEEE Transactions on Medical Imaging*, Vol.12 No. 3 (September 1993).
- Hinnrichs M, Morris G.M., "Image multispectral sensing", United States Patent #5,479,258 (December 26, 1995).
- Hinnrichs M., Massie M.A., "Image multispectral sensing: a new and innovative instrument for hyperspectral imaging using dispersive techniques" *Pro. SPIE* 2480, pp. 93-104, (1995).
- Jansson P.A., *DECONVOLUTION With Applications in Spectroscopy*, Academic Press (1984).
- Javidi B., Caulfield H.J., Horner J.L., "Image deconvolution by nonlinear signal processing," *Applied Optics* Vol.28(15), pp.3106-3111 (August 1989).
- Jones P.F., Aitken G.J.M., "Comparison of three-dimensional imaging systems," *J. Opt. Soc. Am.* 11,10 (October 1994).
- Kawata S., Ichioka Y., "Iterative image restoration for linearly degraded images. II. Reblurring procedure," *J. Opt. Soc. Am.* Vol. 70(7), pp.768-772 (July 1980).
- Lesem, Hirsute, and Jordan, "The kinoform: a new wavefront reconstruction device," *IBM J. Res. Dev.* 13, 150 (1969).
- Levi L., *Applied Optics: A guide to Optical System Design/Volume 1*, John Wiley & Sons (1968)
- Lyons D., Mikolas D., "Fabrication of large aperture optical elements on Germanium and BK-7 Glass substrates." *Research Accomplishments* National Nanofabricaton Facility at Cornell (1994).

REFERENCES-Continued

- Lyons D., "Image Spectrometry with a Diffractive Optic," *Imaging Spectrometry*, Pro. SPIE 2480, pp. 123-131, (April 1995).
- Lyons D., Whitcomb K., "The DOE in DOIS, a diffractive optic image spectrometer", *Diffractive & Holographic Optics Technology III*, Proc SPIE Vol 2689 (February 1996).
- Lyons D., Whitcomb K., "Image reconstruction algorithms for DOIS", *Algorithms for Multispectral Imagery*, Proc SPIE Vol 2758 (April 1996).
- Lyons D., Whitcomb K., "Characterization of the DOIS prototype", *Imaging Spectrometry II: New Sensors*, Proc SPIE Vol 2819 (August 1996).
- Lyons D., Whitcomb K., "Diffractive optic image spectrometer with constant magnification", United States Patent pending (March 1997).
- Madjidi-Zolbanine H., Froehly C., "Holographic correction of both chromatic and spherical aberrations of single glass lenses," *Applied Optics* Vol. 18(14), pp.2385-2393 (July 15, 1979).
- Miyamoto, "The phase Fresnel lens," *J. Opt. Soc. Am.* 51, 17 (1961).
- Mooney J.M., "Angularly multiplexed spectral imager," *Pro. SPIE* 2480, pp. 65-77, (1995).
- Morris M.G., Rochester Photonics Corporation, Rochester NY, (716) 272-3010, private communications (1994)
- O'Shea D.C., "Grayscale masks for diffractive optics," in *Diffractive Optics*, Vol. 11, 1994 OSA Technical Digest Series, pp. 119-124 (1995).
- Press W. H., Flannery B. P., Teukolsky S. A. and Vetterling W. T., *Numerical Recipes in C*, Cambridge University Press (1988).
- Reynolds G.O., DeVelis J.B., Parrent G.B., Thompson B.J., *The New Physical Optics Notebook: Tutorials in Fourier Optics*, SPIE Optical Engineering Press (1989).
- Robbins G.M., Huang T.S., "Inverse Filtering for Linear Shift-Variant Imaging Systems," *Proceedings of the IEEE* Vol.60 No. 7, pp. 862-872 (July 1972).
- Russ J.C., *The Image Processing Handbook*, CRC Press (1995).
- Sawchuk A.A., "Space-Variant Image Motion Degradation and Restoration," *Proceedings of the IEEE* Vol. 60 No.7, pp. 854-861 (July 1972).
- Sawchuk A.A., "Space-variant image restoration by coordinate transformations," *J. Opt. Soc. Am.* 64,2 (February 1974).

REFERENCES-Continued

- Schowengerdt R.A., *Techniques for Image Processing and Classification in Remote Sensing*, Academic Press (1983).
- Sezan M.I., *Selected Papers on Digital Image Restoration*, SPIE Milestone Series, Vol. MS 47 (1992).
- Sezan M.I., Tekalp A.M., "Survey of recent developments in digital image restoration," *Optical Engineering* Vol. 29 No. 5, 393-404 (May 1990).
- Shaw P.J., "3-dimensional microscopy using tilted views," *SPIE Vol. 1161 New Methods in Microscopy and Low Light Imaging* (1989).
- Sitter D.N. Jr., Rhodes W.T., "Three-dimensional imaging: a space invariant model for space variant systems," *Applied Optics* Vol. 29(26), pp.3789-3794 (10 September 1990).
- Smith W.J., *Modern Lens Design*, McGraw-Hill (1992).
- Stone T.W., Thompson B.J., *Holographic and Diffractive Lenses and Mirrors*, SPIE Milestone Series, Vol. MS 34, (1991).
- Stone T., George N., "Hybrid diffractive-refractive lenses and achromats," *Applied Optics*, Vol. 27(14), pp. 2960-2971 (1990)
- Swanson G.J., "Binary Optics Technology: The Theory and Design of Multi-level Diffractive Optical Elements", Lincoln Laboratory Technical Report # 854, (1989).
- Sweatt W.C., "Mathematical equivalence between a holographic optical element and an ultra-high index lens," *J. Opt. Soc. Am.* Vol. 69(3), pp. 486-487 (March 1979).
- Veldkamp, Swanson G.J., "Diffractive optical elements for use in infrared systems," *Optical Engineering* Vol. 28 No. 6, 605(1989).
- Waggoner A., DeBiasio R., Conrad P., Bright G.R., Ernst L. Ryan K., Nederlof M., Taylor D., "Multiple Spectral Parameter Imaging", *Methods in Cell Biology* Vol. 30 Ch.17, pp. 449-478, Academic Press (1989).
- Ward J.E., Auth D.C., Carlson F.P., "Lens Aberration corrected by holography," *Applied Optics*, Vol. 10(4), pp. 896-900 (April 1971)
- Wilson R.G., McCreary S.M., Thompson J.L., "Optical transformations in three-space: Simulations with a PC," *Am. J. Phys.* 60 (1), (January 1992).
- Wolfe W.L., Zissis G.J., *The Infrared Handbook*, Infrared Information Analysis Center at ERIM, (1989).
- Wolfe W.L., "Multispectral Imaging Devices," SPIE short course notes SC54, 27 July 1994.
- Wolfram S., *Mathematica*, Addison-Wesley (1991).

MISSION OF ROME LABORATORY

Mission. The mission of Rome Laboratory is to advance the science and technologies of command, control, communications and intelligence and to transition them into systems to meet customer needs. To achieve this, Rome Lab:

- a. Conducts vigorous research, development and test programs in all applicable technologies;
- b. Transitions technology to current and future systems to improve operational capability, readiness, and supportability;
- c. Provides a full range of technical support to Air Force Material Command product centers and other Air Force organizations;
- d. Promotes transfer of technology to the private sector;
- e. Maintains leading edge technological expertise in the areas of surveillance, communications, command and control, intelligence, reliability science, electro-magnetic technology, photonics, signal processing, and computational science.

The thrust areas of technical competence include: Surveillance, Communications, Command and Control, Intelligence, Signal Processing, Computer Science and Technology, Electromagnetic Technology, Photonics and Reliability Sciences.